Draft Manuscript for Review

The lamphrophyric dykes of the Dolomitic Area (Southern Alps, Italy): markers of the Late Triassic shift from orogenic-like to anorogenic magmatism

Journal:	*Journal of Petrology*
Manuscript ID	Draft
Manuscript Type:	Original Manuscript
Date Submitted by the Author:	n/a
Complete List of Authors:	Casetta, Federico; University of Ferrara, Physics and Earth Sciences; Ickert, Ryan; Scottish Universities Environmental Research Centre Mark, Darren; Argon Isotope Facility, Scottish Universities Environmental Research Centre (SUERC) Bonadiman, Costanza; Università Di Ferrara, Giacomoni, Pier Paolo; University of Ferrara, Department of Earth Sciences Ntaflos, Theodoros; University of Vienna, Dept. of Lithospheric Research; Coltorti, Massimo; Università Di Ferrara,
Keyword:	Alkaline-carbonatitic lamprophyre, Amphibole texture, Camptonite, Dolomitic Area, Predazzo, Southern Alps, Triassic magmatism

The lamphrophyric dykes of the Dolomitic Area (Southern Alps, Italy): markers of the Late Triassic shift from orogenic-like to anorogenic magmatism

Running title: A Late Triassic alkaline-carbonatitic pulse in the Dolomitic Area

Federico Casetta*

Department of Physics and Earth Sciences, University of Ferrara

Via Saragat 1, 44121 Ferrara, Italy

Ryan B. Ickert

Scottish Universities Environmental Research Centre, Scottish Enterprise Technology Park, Rankine Avenue, East Kilbride, G75 0QF, UK

Darren F. Mark

Scottish Universities Environmental Research Centre, Scottish Enterprise Technology Park, Rankine Avenue, East Kilbride, G75 0QF, UK

Department of Earth & Environmental Science, University of St Andrews, St Andrews, KY16 9AJ, UK

Costanza Bonadiman**

Department of Physics and Earth Sciences, University of Ferrara

Via Saragat 1, 44121 Ferrara, Italy

Pier Paolo Giacomoni

Department of Physics and Earth Sciences, University of Ferrara

Via Saragat 1, 44121 Ferrara, Italy

Theodoros Ntaflos

Department of Lithospheric Research, Universität Wien

Althanstraße 14 (UZA II), 1090 Wien, Austria

Massimo Coltorti

Department of Physics and Earth Sciences, University of Ferrara

Via Saragat 1, 44121 Ferrara, Italy

* Corresponding author. Phone +39 0532 974721. E-mail: cstfrc@unife.it

** Corresponding author. Phone +39 0532 974720. E-mail: bdc@unife.it

The lamphrophyric dykes of the Dolomitic Area (Southern Alps, Italy): markers of the Late Triassic shift from orogenic-like to anorogenic magmatism

ABSTRACT

The camptonitic/bostonitic dykes cropping out at Predazzo (Dolomitic Area, Southern Alps) are among the oldest examples of lamprophyric rocks in Italy. Interpreted as a late-stage pulse related to the Middle Triassic high K calc-alkaline/shoshonitic magmatism of the Predazzo Intrusive Complex, these alkaline lamprophyres are poorly studied. In this paper, we present the first complete petrological, geochemical and geochronological characterization of the Predazzo lamprophyres, with the aim of deciphering their relationship with the Triassic magmatic events of the Dolomitic Area and the whole Southern Alps. We find that the Predazzo lamprophyric magmatic system was dominated by fractional crystallization processes, even if the amphibole textures suggest small scale mixing dynamics during differentiation. Moreover, the occurrence of primary carbonate ocelli in the camptontic rocks suggest that the alkaline lamprophyric magmas were associated with carbonatitic melts. On the basis of elemental, geochronological and isotopic data, we show that: i) Predazzo lamprophyres were emplaced at 219.22 ± 0.46/0.73 Ma ($^{40}Ar/^{39}Ar$; 2σ; analytical/full systematic uncertainties), and are therefore younger than the short-lived Ladinian (237-238 Ma) magmatic event of the Dolomitic Area; ii) their trace element and Sr-Nd isotopic signature ($^{87}Sr/^{86}Sr_i$ = 0.7033-0.7040; $^{143}Nd/^{144}Nd_i$ = 0.51260-0.51265) suggest a garnet-amphibole-bearing mantle source that interacted with asthenospheric components, diverging from the Ladinian high K calc-alkaline/shoshonitic rocks, which require a source with subduction signature. All these features, fostered by a comparison to the main Middle-Late Triassic magmatic occurrences of the Alps and Carpathians regions, suggest that the Predazzo alkaline lamprophyres belong to the same alkaline-carbonatitic magmatic event that intruded the mantle beneath the Southern Alps (i.e. Finero peridotite) at about 215-225 Ma. In this scenario, the Predazzo camptonites/bostonite

dykes cannot be considered as a late-stage pulse of the orogenic-like Ladinian magmatism of the Dolomitic Area but represent the geochemical/geochronological junction between it and the rifting phase related to the opening of the Alpine Tethys.

KEYWORDS

Alkaline-carbonatitic lamprophyre; Amphibole texture; Camptonite; Dolomitic Area; Predazzo; Southern Alps; Triassic magmatism.

INTRODUCTION

The late-stage emplacement of lamprophyric dykes typifies a large number of plutonic complexes, providing important information of the local geodynamic evolution. According to Le Maitre *et al.* (1989), Rock (1991), Woolley *et al.* (1996) and Le Maitre *et al.* (2002), lamprophyres can be defined as H_2O, CO_2 and alkali-rich rocks with a porphyritic texture, characterized by amphibole and/or phlogopite phenocrysts and feldspars and/or feldspathoids in the groundmass. Their genesis is commonly attributed to partial melting of a metasomatised mantle (Rock, 1991; Stoppa *et al.*, 2014; Pandey *et al.*, 2017*a*; 2017*b*; Soder & Romer 2018), whereas their emplacement is usually associated to the onset of lithospheric extensional-transtensional tectonic regimes. Lamprophyres, in fact, are typically associated with strike-slip movements, and potentially act as markers of a change in the geodynamic regime and tectonomagmatic conditions (Scarrow *et al.*, 2011). Following Le Maitre *et al.* (2002), lamprophyric rocks are grouped, on the basis of their mineralogy, into three associations: i) minette-kersantite; ii) vogesite-spessartite; iii) sannaite-camptonite-monchiquite. This discrimination partially reflects what was originally proposed by Le Maitre *et al.* (1989) and Rock (1991), according to whom the first two associations belong to the "calc-alkaline (shoshonitic) lamprophyres", whereas the third to the "alkaline lamprophyres". While the calc-alkaline variety is commonly (but not exclusively) associated to convergent settings, alkaline

lamprophyres are typical of divergent margins and continental intra-plate settings (Rock, 1991; Batki *et al.*, 2014; Stoppa *et al.*, 2014; Ubide *et al.*, 2014; Lu *et al.*, 2015; Pandey *et al.*, 2017*a*; 2017*b*), their composition resembling that of volatile-enriched alkali basalts, basanites and nephelinites.

Several authors have investigated the main geochemical features of the Cretaceous (110 Ma) to Oligocenic (29 Ma) alkaline lamprophyres across Italy, speculating about their genesis by partial melting of the deep mantle portions metasomatized by alkaline carbonatitic components (Galassi *et al.*, 1994; Vichi *et al.*, 2005; Stoppa, 2008; Stoppa *et al.*, 2014). Lesser known are the alkaline lamprophyres of the Dolomitic Area (Southalpine domain, NE Italy), associated with the Middle Triassic Predazzo Intrusive Complex, to which they seem geochemically and temporally related (Lucchini *et al.*, 1969). However, the connection between these alkaline lamprophyres and the host volcano-plutonic complex, of trachybasaltic/shoshonitic affinity, has never been investigated, remaining an intriguing topic and a key factor for deciphering the evolution of the magmatism of the Dolomitic Area.

Whole-rock major, trace element and Sr-Nd isotopic determinations, together with mineral phases major and trace element chemistry, were used to characterize the Predazzo alkaline lamphrophyres and model their mantle source, on one side, and the main differentiation dynamics to which lamprophyric melts underwent at shallow depth, on the other side. Finally, $^{40}Ar/^{39}Ar$ dating on crystal separates enabled to frame for the first time their emplacement within the temporal evolution of the Dolomitic Area and the whole Southern Alps magmatism.

GEOLOGICAL AND GEODYNAMIC OVERVIEW

The geodynamic framework of the Autroalpine-Southalpine domains during Middle-Late Triassic is a challenging topic, mainly because of the variety of magmas erupted over a short time span in a relatively limited area, whose tectonic features have been also subsequently obscured by the Alpine orogenesis. Magmas with calc-alkaline/shoshonitic affinity intruded in

several localities of the Southern Alps, Dynarides and Hellenides between ~242 and 227±6 Ma (Bebien *et al.*, 1978; Barbieri et al., 1982; Pe-Piper, 1982; 1983; 1998; Pamić, 1984; Gianolla, 1992; Mundil *et al.*, 1996; Armienti *et al.*, 2003; Beccaluva *et al.*, 2005; Cassinis *et al.*, 2008; Bellieni *et al.*, 2010; Beltràn-Trivino *et al.*, 2016; Bianchini *et al.*, 2018; Storck *et al.*, 2018; Wotzlaw *et al.*, 2018). Simultaneously, scattered intrusions of alkaline magmas emplaced between 231±1 and 227±7 Ma along the Periadriatic lineament (Karawanken) and in the Carpathians (Ditrau) area (Lippolt & Pidgeon, 1974; Dallmeyer *et al.*, 1997; Morogan *et al.*, 2000; Visonà & Zanferrari, 2000; Batki *et al.*, 2014; Pál-Molnár *et al.*, 2015).

The concomitance between the orogenic signature of the Southern Alps magmatism and the onset of extensional-transtensional tectonic regimes (Doglioni, 1984, 1987, 2007; Stampfli & Borel, 2002; 2004) led some to hypothesize various possible geodynamic scenarios for the Southern Alps. They include: i) aborted rifting in a passive margin (Bernoulli & Lemoine, 1980); ii) active mantle upwelling (Stähle *et al.*, 2001); iii) arc system at the Paleo-Tethys NW limb (Castellarin *et al.*, 1988); iv) back-arc development connected to the subduction of the Paleo-Tethys (Ziegler & Stampfli, 2001; Stampfli & Borel, 2002; 2004; Stampfli *et al.*, 2002; Armienti *et al.*, 2003; Stampfli, 2005; Cassinis *et al.*, 2008; Schmid *et al.*, 2008; Zanetti *et al.*, 2013); v) anorogenic rifting with subduction signature inherited from the Hercynian orogeny (Sloman, 1989; Bonadiman *et al.*, 1994; Pe-Piper, 1998; Beltràn-Trivino *et al.*, 2016). To interpret the distribution of the Triassic orogenic and anorogenic magmatism, Visonà & Zanferrari (2000) hypothesized that the mantle portions beneath the Southalpine-Austroalpine and the Carnian-Dinaric plates experienced different Palaeozoic evolutions, being affected by subduction-related and plume-related processes, respectively. Alternatively, Bianchini *et al.* (2018) proposed the existence of a Palaeozoic oceanic basin between the Southalpine and Austroalpine domains closed by a subducted plate dipping beneath the former. In such a scenario, the mantle beneath the Southalpine domain was fluxed by subduction-related components, whereas its Austroalpine counterpart was affected by mantle upwelling dynamics.

The Predazzo Intrusive Complex and the lamprophyric dykes

Among the Middle Triassic magmatic occurrences in the Southern Alps, the Dolomitic Area is the most intriguing, since it is composed of huge amounts of basaltic/latitic volcanics (~2000 km^2 of areal extension), their plutonic counterparts (Predazzo Intrusive Complex, Mt. Monzoni and Cima Pape), and a well-developed dyke swarm (Gasparotto & Simboli, 1991; Bonadiman *et al.*, 1994; Casetta *et al.*, 2018*a*; 2018*b*). According to Abbas *et al.* (2018), the duration of the magmatic event responsible for the generation of the Dolomitic Area volcano-plutonic bodies was ~0.7 Ma, in agreement with the solidification time of the Predazzo Intrusive Complex (PIC) proposed by Casetta *et al.* (2018*a*). On the other hand, age data reported by Storck *et al.* (2018) from an ash layer in the Bagolino section (Brescian Alps) enabled to extend the duration of this magmatic event to ~5 Ma, thus from 242.653 ± 0.036 to 237.579 ± 0.042 Ma.

Of the three plutonic bodies cropping out in the Dolomitic Area, PIC is the only multi-pulse intrusion, created by the emplacement of three SiO_2-saturated to -undersaturated magma batches. It can be subdivided in three units, named Shoshonitic Silica Saturated (SS), Shoshonitic Silica Undersaturated (SU) and Granitic Unit (GU). The SS and SU units, characterized by shoshonitic affinity, are composed, respectively, of quartz- and nepheline-bearing pyroxenites/gabbros to syenites, whereas GU is composed of granites and syenogranites with high-K calc-alkaline affinity. The cross-cutting relationships between dykes and the various portions of the intrusion suggest the following emplacement sequence for the complex: SS→GU→SU (Casetta *et al.*, 2018*b*). Petrologic and isotopic (Sr-Nd) studies on PIC, complemented by field observations, reveal (i) the shallow depth of the intrusion (1.4-5.6 km); (ii) its textural gradual transition towards the overlying hypabyssal and volcanic deposits; (iii) the low degree of crustal assimilation experienced by PIC magmas during ascent; (iv) the Sr-Nd isotopic enrichment of PIC rocks, well fitting the EM I mantle field; (e) the slight progressive isotopic depletion in the mantle source, moving towards higher $^{143}Nd/^{144}Nd$ ratios

from the SS to the SU batches (Casetta *et al.*, 2018*a*; 2018*b*). A Zircon U-Pb age shows that the emplacement of the GU syenogranites occurred at 237.3 ± 1.0 Ma (Mundil *et al.*, 1996). Analogously, a recent study by Storck *et al.* (2018) proposed a crystallization age of 238.075 ± 0.087 Ma (U-Pb on zircon) for PIC monzodiorites: unfortunately, the lack of precise information about sampling localities prevents to relate such monzodiorites to the SS or SU suites.

Within the Predazzo area, an articulated swarm of dykes, ranging in thickness from decimeters to meters, intrudes both the PIC, the overlying volcanics, and the sedimentary host rocks (Fig. 1). These dykes are mainly porphyritic basalts to trachytes with the same geochemical features of the intrusive batches. A minor portion of the dyke swarm is composed of grey to greenish lamprophyric dykes, 0.2-2.0 m in thickness (Fig. 2). As the majority of the dykes of this area, lamprophyres are intruded inside PIC (SS and GU bodies) and the surrounding volcanites; only one sample has been found within the Permian Val Gardena sandstone formation (Lucchini *et al.*, 1969).

MATERIALS AND METHODS

Whole-rock major and trace element analyses were carried out at the Department of Physics and Earth Sciences of the University of Ferrara using an ARL Advant-XP automated X-ray fluorescence spectrometer. Full matrix correction procedure and intensities were completed following Traill & Lachance (1966). Accuracy and precision are better than 2-5% for major elements and 5-10% for trace elements. Detection limits are 0.01 wt% and 1-3 ppm for most of the major and trace element concentrations, respectively.

Rb, Sr, Y, Zr, Nb, Hf, Ta, Th, U, and rare-earth elements (REE) were analyzed at the Department of Physics and Earth Sciences of the University of Ferrara by inductively coupled plasma-mass spectrometry (ICP-MS) using a Thermo Series X spectrometer with precision and accuracy better than 10% for all elements, well above the detection limit.

Mineral phase major element compositions were analyzed at the Department of Lithospheric Research of the University of Wien, using a CAMECA SX100 electron microprobe equipped with four WD and one ED spectrometers. The operating conditions were as follows: 15 kV accelerating voltage, 20 nA beam current, and 20 s counting time on peak position. Natural and synthetic standards were used for calibration, and PAP corrections were applied to the intensity data (Pouchou & Pichoir 1991).

Trace element concentration of pyroxene and amphibole crystals was carried out at the CNR - Istituto di Georisorse of Pavia by laser ablation microprobe-inductively coupled plasma-mass spectrometry (LAM-ICP-MS). The basic set and protocol were described by Tiepolo *et al.* (2003). NIST 610 and NIST 612 standard glasses were used to calibrate relative element sensitivity. Precision and accuracy for trace element analyses were assessed by standard sample BCR-2 (reference values from USGS Geochemical Reference Materials Database). Each analysis was corrected with internal standards using CaO for both clinopyroxene and amphibole. The detection limit was function of the ablation volume and counting time and was therefore calculated for each analysis; indeed, ablation volume greatly dependes on instrument configuration. As a consequence, the detection limit reduces if spot size, beam power and cell gas flow are decreased. A 40-100 μm beam diameter and 20 μm s1 scanning rate were used. The theoretical detection limit ranges from 10 to 20 ppb for REE, Ba, Th, U, Zr and are about 2 ppm for Ti.

Whole-rock $^{87}Sr/^{86}Sr$ and $^{143}Nd/^{144}Nd$ isotopic analyses were performed at the Radiogenic Laboratory of the Scottish Universities Environmental Research Centre (SUERC) of Glasgow by means of a Sector-54 TIMS instrument. Strontium and Nd mass fractionation was corrected with exponential laws to $^{86}Sr/^{88}Sr = 0.1194$ and $^{146}Nd/^{144}Nd = 0.7219$, respectively. Eight measurements of SRM987 standard during the course of this analytical programme yielded a mean value of 0.710244±0.000016 (2 SD), consistent with the consensus value of ~0.71025. Twelve measurements of JNdi standard during the course of this analytical programme yielded

a mean value of 0.512079±0.000018 (2 SD), consistent with consensus value of 0.51210. For signal intensities, loading conditions and sample preparation procedures for Sr-Nd isotopic analyses see Casetta *et al.* (2018*a*).

Samples (amphibole and feldspar separates) for $^{40}Ar/^{39}Ar$ dating were prepared using the methods described in Mark *et al.* (2011*a*). All samples were subsequently cleaned in de-ionised water. They were parcelled in high purity Al discs for irradiation. International standards Fish Canyon sanidine (FCs) (28.294 ± 0.036 Ma, Renne *et al.*, 2011; Morgan *et al.*, 2014) and GA1550 biotite (99.738 ± 0.104 Ma, Renne *et al.*, 2011) were loaded adjacent to the samples to permit accurate characterisation of the neutron flux (J parameter). Samples were irradiated for 50 hours in the Cd-lined facility of the CLICIT Facility at the OSU TRIGA reactor. Standards were analyzed on a MAP 215-50 system (described below briefly and in more detail by Ellis *et al.*, 2012) - FCs was analyzed by CO_2 laser total fusion as single crystals (n = 20). GA1550 (n = 20) was also analyzed by CO_2 laser total fusion and step-heated using a CO_2 scanning laser (n = 5) (Barfod *et al.*, 2014). Using GA1550 the J-parameter was determined to a precision approaching 0.1% uncertainty.

Wafers were loaded into an Ultra-High-Vacuum (UHV) laser cell with a SiO_2 window. In situ UVLAMP Ar extraction was conducted using a New Wave UP-213 nm UV laser system (described in Moore *et al.*, 2011). 50 x 50 x 5 μm^3 (amounts of ablated material approximately 1250 μm^3) raster pits were made in mineral surfaces to extract the Ar isotopes. All gas fractions were subjected to 180 seconds of purification by exposure to two SAES GP50 getters (one maintained at room temperature, the other held at ca. 450˚C). A cold finger was maintained at -95.5˚C using a mixture of dry ice ($CO_{2[S]}$) and acetone. Ion beam intensities (i.e., Ar isotope intensities and hence ratios) were measured using a MAP 215-50 mass spectrometer in peak jumping mode. Measurements were made using a Balzers SEV-217 electron multiplier. The system had a measured sensitivity of 1.12 x 10^{-13} moles/Volt. The extraction and cleanup, as well as mass spectrometer inlet and measurement protocols and data acquisition were

automated. Blanks (full extraction line and mass spectrometer) were made following every two analyses of unknowns. The average blank ± standard deviation (n = 28) from the entire blank run sequence was used to correct raw isotope measurements from unknowns. Mass discrimination was monitored by analysis of air pipette aliquots after every five analyses of unknowns (n = 13, 7.21 x 10^{-14} moles ^{40}Ar, $^{40}Ar/^{36}Ar$ = 289.67 ± 0.63).

The samples were step-heated using a CO_2 laser (approximately 500-1500˚C, optical pyrometer measurements). Extracted gases were subjected to 300 seconds of purification by exposure to two SAES GP50 getters (one maintained at room temperature, the other held at ca. 450˚C). A cold finger was maintained at -95.5˚C using a mixture of dry ice ($CO_{2[S]}$) and acetone. Ion beam intensities were measured using a MAP 215-50 mass spectrometer in peak jumping mode. Measurements were made using a Balzers SEV-217 electron multiplier. The system had a measured sensitivity of 1.12 x 10^{-13} moles/Volt. The extraction and cleanup, as well as mass spectrometer inlet and measurement protocols and data acquisition were automated. Blanks (full extraction line and mass spectrometer) were made following every analysis of an unknown. The average blank ± standard deviation for each experiment (n = 14) from the entire blank run sequence was used to correct raw isotope measurements from unknowns. Mass discrimination was monitored by analysis of air pipette aliquots after every three analyses.

All Ar isotope data were corrected for backgrounds, mass discrimination, and reactor-produced nuclides and processed using standard data reduction protocols and reported according to the criteria of Renne *et al.* (2009). The atmospheric argon isotope ratios of Lee *et al.* (2006), which have been independently verified by Mark *et al.* (2011*b*), were employed. The $^{40}Ar/^{39}Ar$ ages for were determined relative to the statistical optimization model of Renne *et al.* (2010; 2011) and are reported including analytical and full systematic uncertainties at the 2 sigma level. All raw Ar/Ar data with associated parameters are presented in Electronic Appendix 1.

PETROGRAPHY AND WHOLE ROCK GEOCHEMISTRY

Petrography

The lamprophyric dykes cropping out at Predazzo (Fig. 2), generally NNW-SSE and N-S oriented, are easily recognizable on field for their grey-greenish colour and for abundant, cm-size xenoliths and megacrysts (Vardabasso, 1929; Lucchini *et al.*, 1969; 1982). The majority of the xenoliths are cumulitic clinopyroxenites (Morten, 1980) and/or feldspar+quartz aggregates from the Triassic intrusive rocks and the Permian basement, but also a few mantle-derived spinel lherzolites can be found.

The mineral paragenesis of Predazzo lamprophyres, together with their chemical composition, led Lucchini *et al.* (1969) to classify them as camptonites, an alkaline variety of lamprophyres characterized by abundant plagioclase (modally more abundant than K-feldspar), and the absence of leucite and Na-foids (Rock, 1991).

The texture of the analyzed samples is generally panidiomorphic, with, in order of decreasing abundance, amphibole, plagioclase, clinopyroxene and olivine phenocrysts, embedded in a microcrystalline assemblage made of amphibole, plagioclase, clinopyroxene, K-feldspar and Fe-Ti oxides (Fig. 2). Accessory phases include carbonate, ilmenite, titanite, apatite and analcime. The modal abundance of the main constituents can be summarized as: amphibole 40%, plagioclase 35%, clinopyroxene 10%, olivine 7%, K-feldspar 3%, Fe-Ti oxides 5%. Carbonate is present as filling of olivine sites, in secondary veins/fractures or as major constituent of small (200-250 μm in diameter) spherical ocelli, variably distributed and surrounded by the tangential growth of plagioclase, amphibole and/or clinopyroxene. Large-sized (up to 5 cm) feldspar and amphibole megacrysts often occur. Only one sample (MA1) is characterized by the lack of clinopyroxene and olivine, being composed of, in order of decreasing abundance, amphibole (50%), plagioclase (40%), K-feldspar (6%) and Fe-Ti oxides (4%). These features confirm the definition of camptonites proposed by the previous authors for almost all Predazzo lamprophyres. An exception is constituted by the evolved sample MA1, whose differentiated nature led to the definition of bostonite (*sensu latu*, "mildly alkaline,

porphyritic, leucocratic dyke rocks intimately associated with some camptonite-monchiquite dyke-suites; corresponds in IUGS terminology to porphyritic (biotite-hornblende) alkali feldspar trachyte or micro-alkali feldspar syenite"; Rock, 1991; Fig. 2).

Amphibole, pale brown to reddish in colour, dominates the paragenesis of Predazzo camptonites, always occurring with euhedral habitus and elongated shape in both the phenocrysts and the groundmass types. In the bostonite sample, amphibole shape is often nearly acicular, and its colour is pale brown to yellowish. It ranges in size from 20-30 μm (groundmass) to 2.5 mm (phenocryst), excluding the exceptional centimetric dimensions reached by the megacrysts, whose colour ranges from dark brown to black.

Plagioclase crystals are euhedral and vary in size between 10-20 and 400-450 μm, being the second major constituent of the lamprophyre paragenesis. In the bostonitic dyke, its volumetric abundance sensitively increases. Larger plagioclase xenocrysts, shreds and aggregates (0.5-1 mm) of crustal origin can be easily distinguished from the phenocrysts by their rounded shape and by the presence of well developed reaction rims.

Clinopyroxene, pale brown in colour, is modally subordinant and smaller than amphibole, rarely exceeding 150-200 μm in size among the phenocrysts. Relicts of bigger euhedral clinopyroxene crystals (1-2 mm) are almost totally dismembered and replaced by plagioclase, amphibole and Fe-Ti oxides, resulting in an "atoll-like" shape, where only the outermost rim is preserved.

Olivine (100-350 μm) is rare and present only as a phenocryst phase, appearing usually altered and pseudomorphosed by calcite and serpentine.

K-feldspar and Fe-Ti oxides are present in the groundmass, rarely exceeding 40-50 μm in size. Clinopyroxene ad olivine are totally absent in the bostonite sample, where the presence of K-feldspar and Fe-Ti oxides strongly increases. Many samples are strongly altered, and the formation of secondary calcite, serpentine, epidote and chlorite often occurs at the expense of olivine and clinopyroxene.

Whole rock major and trace element chemistry

Predazzo camptonites are characterized by SiO_2 in the range of 44.1 to 47.9 wt% and high alkali contents (1.6-3.2 Na_2O wt%; 1.0-3.7 K_2O wt%), plotting between the basanite, basalt and trachybasalt fields of the TAS diagram (Fig. 3; Table 1). Sample MA1 is characterized by higher silica (52.8 wt%) and alkali (2.9 Na_2O wt%; 5.0 K_2O wt%) contents, plotting in the basaltic trachyandesite field. Mg# values (calculated as MgO/[MgO+FeO] mol%, assuming Fe_2O_3/FeO ratio of 0.15 in agreement with a fO_2 around FMQ buffer; Kress & Carmichael, 1991) are extremely variable, ranging from 70 to 37. These values strongly depend on the large MgO variations (from 3.0 to 11.3 wt%) at a narrower FeO interval (8.5-10.8 wt%). The lowest FeO content (6.5 wt%) is reported from the bostonite, whose Mg# is about 47. TiO_2 (1.4-2.4 wt%) and Al_2O_3 (15.3-18.8 wt%) contents are respectively slightly lower and higher than the values proposed by Rock (1991) as averaged composition for an alkaline lamprophyre. CaO contents span the range of 8.8-14.2 wt%, and are sensitive to secondary alteration/hydrothermal processes and to the variable presence of carbonates. K_2O/Na_2O are between 0.6 and 2.0, marking the K-affinity of all Predazzo lamprophyres. CIPW norm calculations highlight the moderate to strong Si-undersaturation, with 1-13% normative nepheline and the presence of 3-5% normative leucite for two samples with high K/Si. MgO is negatively correlated with compatible elements, such as Ni (from 237 to 27 ppm), Co (from 48 to 26 ppm) and Cr (from 585 to 14 ppm), suggestings that Predazzo lamprophyres underwent an initial fractionation of olivine and clinopyroxene, consistent with the observed mineral paragenesis (Fig. 4). Rubidium (31-331 ppm) and Ba (334-991 ppm) do not show any correlation with MgO, whereas Sr and Zr concentration progressively increase from 581 to 1546 ppm and from 150 to 356 ppm respectively with decreasing MgO (Fig. 4).

Chondrite-normalized (Sun & McDonough, 1989) incompatible element patterns of Predazzo lamprophyres (Fig. 5) are characterized by Nb, Ta and LILE (especially Sr) enrichments, as

well as by negative anomalies in Th and U and positive peaks in Zr and Ti with respect the adjacent elements. These features are similar to those documented by Scarrow *et al.* (2011) in the Central Iberia camptonites/bostonites. The Predazzo lamprophyre pattern resembles that of alkaline rocks, but, when compared to the average composition of oceanic island basalts (OIB, Sun & McDonough, 1989), they appear depleted in all elements except Rb, Ba and Sr. This feature is even more evident if we compare them to the average pattern of camptonites (Fig. 5; Rock, 1991). Chondrite-normalized (Sun & McDonough, 1989) REE patterns are characterized by LREE enrichment (up to 200 times chondrite; La_N/Yb_N up to 11.0) and flat M-HREE profiles, with absence of Eu negative anomaly, consistent with the lack of significant plagioclase fractionation, even in the bostonitic sample (Fig. 5). The less differentiated camptonite (Mg# 70) is slightly LREE-depleted with respect to the other camptonites, as evidenced by its lower La_N/Yb_N ratio of about 6.0. The Gd_N/Yb_N ratios of Predazzo camptonites range between 1.7 and 2.7, contrasting with the typical steep-sloping shape of OIB rocks in general, and of camptonites in particular (Fig. 5; Sun & McDonough, 1989; Rock, 1991). Compared to the Cretaceous (110 Ma) to Oligocenic (29 Ma) alkaline and ultramafic Italian lamprophyres (Galassi *et al.*, 1994; Vichi *et al.*, 2005; Stoppa, 2008; Stoppa *et al.*, 2014), Predazzo camptonites/bostonites are generally depleted in all incompatible elements, except for Rb and K. A common feature is the absence of a Ta-Nb-Ti negative anomaly (Fig. 5).

MINERAL CHEMISTRY AND TEXTURES

Major element composition of amphibole, clinopyroxene, feldspars, oxides and trace element analyses of amphibole and clinopyroxene have been determined on representative crystals in the primitive and differentiated lamprophyres. The intense state of alteration of the olivine crystals, which are filled by calcite/serpentine, prevented their chemical analysis, therefore we briefly summarize the olivine compositional features inside Predazzo camptonites reported by Carraro & Visonà (2003). According to these authors, olivine phenocrysts of the less evolved

camptonites range in compostion from $Fo_{72.5}$ to $Fo_{87.5}$, suggesting a primitive, mantle-derived nature of these rocks.

Amphibole

Due to amphibole chemical complexity, a significant amount of classification schemes have been proposed in literature (e.g. Tindle & Webb 1994; Leake *et al.*, 1997; Hawthorne *et al.*, 2012; Locock, 2014; Ridolfi *et al.*, 2018). Among the most recent classifications, we adopted the Locock (2014) a.p.f.u. computation, calculating the formula on the basis of 24 oxygens (OH, F, Cl, O), and assuming (OH, F, Cl) = (2 - 2Ti) and ^{W}O = 2Ti, according to the recommendations of the IMA-CNMNC subcommittee on amphiboles (Table 2; Hawthorne *et al.*, 2012; Oberti *et al.*, 2012). This cation site distribution assignes the proper nomenclature while minimizing the OH and Fe^{3+} effects.

The analyzed crystals belong to both the ^{W}(OH, F, Cl)- and the ^{W}(O)-dominant (oxo-amphibole) groups, and to the Ca subgroup. Their composition is extremely variable between camptonitic and bostonitic rocks. The former includes pargasite, ferri-kaersutite, magnesio-hastingsite and Ti-rich magnesio-hastingsite, whereas the latter are mainly magnesio-hastingsite, Ti-rich magnesio-hastingsite, Ti-rich ferri-sadanagaite and Ti-rich ferro-ferri-sadanagaite. The sadanagaitic compositions are quite rare and represent the most Si-poor variety of amphibole reported from the alkaline lamprophyres (Rock, 1991). Overall, amphiboles (Mg# = 28-75, calculated as Mg/[Mg+Fe] mol% assuming all Fe as Fe^{2+}) have K_2O and Na_2O contents increasing from 1.0 to 1.5 wt% and from 2.3 to 3.1 wt%, respectively, with decreasing Mg# (Fig. 6). Their TiO_2 (2.0-6.0 wt%) and CaO (10.2-12.4 wt%) contents are positively correlated with Mg#. Aluminium content varies between 12.4 and 16.3 wt% (Table 2). On the basis of cation site distribution, the calculated maximum OH contents is 1.4 a.p.f.u.

Amphibole textural features and major element compositions

Optical and electron microscope observations, coupled with major element chemical data, enabled us to identify the occurrence of five distinct textural types of amphibole, following a scheme analogous to that proposed for plagioclase and clinopyroxene crystals at Mt. Etna by Giacomoni *et al.* (2014; 2016).

Type 1 amphiboles (Fig. 7a) are the most common group among both phenocrysts and groundmass assemblages. They are characterized by euhedral habitus with homogeneous pale brown to orange rounded dissolved cores; the more differentiated their host rock is, the more elongated the crystal shapes are, becoming acicular in the bostonite (MA1) sample. *Type 1* crystals are generally Ti-rich magnesio-hastingsitic (Mg# = 59-71) in MA1 bostonite, and range from pargasitic to magnesio-hastingsitic and Ti-rich magnesio-hastingsitic (Mg# = 71-74) in the camptonites. A reddish ferri-kaersutitic rim (Mg# =59-66) with euhedral shape, in optical continuity with the cores, usually surrounds the larger magnesio-hastingsitic/Ti-rich magnesio-hastingsitic phenocrysts in the camptonites only. Often, in *Type 1* amphiboles an intermediate overgrowth, magnesio-hastingsitic in composition (Mg# = 72-74), is visible only by means of electron microscope. Amphiboles in the groundmass, homogeneous and euhedral, reflect the composition of the outermost rims of the phenocrysts, being therefore ferri-kaersutitic in the camptonites and Ti-rich magnesio-hastingsitic in the bostonites.

Type 2 amphiboles (Fig. 7b) have brown rounded cores, are Ti-rich magnesio-hastingsitic in composition, and are characterized by the presence of dispersed re-crystallizaed glass pockets made of Fe-Ti oxides. The cores (Mg# = 62-64) are often surrounded by magnesio-hastingsitic intermediate overgrowths (Mg# = 73-74) analogous to those documented in *Type 1* amphiboles. Ferri-kaersutitic rims (Mg# = 60-68) border this type of crystals. Both the intermediate overgrowth and the external rim are in optical continuity with the core. This amphibole type has been recognized only in the camptonitic dykes.

Type 3 amphiboles (Fig. 7c), typical of both camptonites and bostonites, are characterized by blackish dusty cores with euhedral edges, surrounded by Ti-rich magnesio-hastingsitic to ferri-

kaersutitic rims (Mg# 53-70). As for *Type 1* crystals, Ti-rich magnesio-hastingsite rims are present in the bostonitic sample whereas ferri-kaersutite ones in the camptonitic ones.

Type 4 amphiboles (Fig. 7d) are those previously defined as xenocrysts. They are usually centimeter-scale in size, black in colour and markedly altered, sometimes being resorbed in entire portions. Their core, Ti-rich magnesio-hastingsitic in composition (Mg# 51-62), is often pervaded by the incipient formation of fibrous minerals and micrometric veins, these latters in turn dominated by the presence of Fe-Ti oxides. The outer portions of the core present strongly dusty resorbed zones comparable to those recognized in *Type 3* crystals. As the other amphiboles, *Type 4* xenocrysts are surrounded by a pale brown to reddish magnesio-hastingsitic to ferri-kaersutitic rim (Mg# ~68).

Type 5 amphiboles (Fig. 7e) occur both as phenocrysts and centimeter-scale megacrysts, dark brown in colour. With respect to *Type 4* xenocrysts, megacrysts can be identified by their habitus, usually euhedral, as well as by the absence of resorption and alteration features. Dark brown euhedral cores with Ti-rich ferri-sadanagaitic to Ti-rich ferro-ferri-sadanagaitic composition (Mg# 29-39) constitute *Type 5* crystals. They are always surrounded by pale brown Ti-rich magnesio-hastingsitic rims (Mg# 68-72), in optical continuity with the cores. This amphibole type has been recognized only in the MA1 bostonite.

It should be noticed that, although important as indicators for the physico-chemical conditions of the lamprophyres magmatic system, *Type 2, Type 3, Type 4* and *Type 5* are much rarer than *Type 1* amphiboles, rarely exceeding 1-5% by volume of the specimens.

Amphibole trace element composition

Due to the small size and general alteration of most of the amphiboles, in situ trace element analyses (Table 3) were obtained only for *Type 1* (both core/rim of the larger phenocrysts and smaller groundmass specimens), *Type 2* (rim) crystals and *Type 4* (core/rim) xenocrysts.

Chondrite-normalized (Sun & McDonough, 1989) incompatible element patterns of amphiboles are characterized by positive Ba and Sr, and negative Th, U and Zr anomalies (Fig. 8). Amphiboles REE content is markedly enriched with respect to the chondritic composition, as displayed by their convex-upward REE pattern (Fig. 8). The most enriched patterns, especially in Nb, Zr, Hf and REE, are shown by the *Type 4* amphibole core and by the *Type 1* groundmass crystals. REE content of these crystals are enriched 30 to 70 times with respect to the chondritic values. On the other side, the less enriched patterns are displayed by *Type 1* larger phenocrysts, characterized by the Zr-Hf-Nb relative depletion at the core and REE depletion at the rim. Generally, rim compositions (*Type 1* crystals and *Type 4* xenocrysts) are REE-depleted with respect to their related cores (Fig. 8). No significant variations between *Type 2* amphibole rims and the *Type 1* larger phenocrysts was recognized.

Clinopyroxene

According to the IMA nomenclature (Morimoto, 1988), clinopyroxene crystals in Predazzo camptonites are generally aluminian- to ferrian-titanian-diopsides (Fig. 6; Table 4). The most magnesian compositions, characterized by Mg# of ~82, are reported from the cores of the larger clinopyroxene phenocrysts. The less magnesian ones, down to Mg# 64, belong to the smaller crystals. Core-rim Mg# decrease from 82 to 68-72 in the larger phenocrysts, whereas smaller pheocrysts are more homogeneous, at Mg# 64-78. As with the amphiboles, the outermost rim of the larger "atoll-like" dismembered clinopyroxenes (Mg# ~74) have a similar composition to the smaller euhedral crystals. Titanium content reaches high values (5.2 wt%) in the ferrian-titanian-diopside terms, as also highlighted by Carraro & Visonà (2003). Al_2O_3 content ranges from 4.8 to 10.9 wt% and is positively correlated with Na_2O (0.25 to 0.75 wt%; Table 4).

Clinopyroxene trace element chemistry

Clinopyroxene trace element analyses (Table 3) were performed on euhedral phenocrysts as well as on the outermost rims of the larger crystal with evident compositional zoning. Chondrite-normalized (Sun & McDonough, 1989) incompatible element patterns of clinopyroxenes resemble those of amphibole, except for those structurally prevented (Rb, Ba) or preferentially partitioned into amphibole (Sr and Ti; Fig. 8). REE patterns also mimic those of amphibole, but with a gentler M-HREE-fractionated profiles (Fig. 8). No significant trace element compositional variations are present between the smaller clinopyroxene phenocrysts and the outermost rims of the larger reacting crystals.

Feldspar

Plagioclase and K-Feldspar crystallization occur later than olivine, clinopyroxene and amphibole, as evidenced by their dimension and texture. Plagioclase compositions vary from bytownite to oligoclase, with anorthite content ranging from An_{74} to An_{41} in the camptonites, and from An_{42} to An_{23} in the MA1 bostonite (Table 5). Even if present in the groundmass of the camptonites, K-Feldspar becames modally and dimensionally significant in the bostonitic sample, where it ranges in composition from Or_{54} to Or_{57} (Fig. 6; Table 5).

Fe-Ti oxides

Fe-Ti oxides are widespread in the groundmass assemblage of all Predazzo lamprophyres, and are generally Ti-magnetitic in composition, with TiO_2 and Al_2O_3 contents ranging from 12.1 to 19.0 wt% and from 2.3 to 7.8 wt%, respectively (Fig. 6; Table 6). As mentioned above, micrometric Ti-magnetite crystals can be also found included in *Type 2* amphibole cores or within the reaction assemblages pervading some clinopyroxene crystals and *Type 4* amphibole xenocrysts.

CARBONATE OCELLI

Rounded ocellar structures with carbonatic composition were identified in most of the Predazzo camptonites, where they occur together with secondary-filled veins/vescicles and late-stage replacement of olivine. The bostonitic sample, however, is ocelli-free, as often happens for differentiated alkaline lamprophyres (Rock, 1991). Chemically, the carbonate crystals analyzed in the ocelli can be subdivided in two groups (Fig. 9; Table 7): i) dolomite-ankerite type (FeO = 5.0-14.4 wt%; MgO = 12.7-18.7 wt%); ii) magnesite-siderite type, close to the breunneritic term (FeO = 27.5-39.0 wt%; MgO = 14.3-24.0 wt%). These compositions well fit those identified by Rock (1991) for the worldwide carbonate-bearing lamprophyres. SrO content is low in all carbonate types, reaching the maximum values of 0.16-0.30 wt% in some dolomite-ankerite grains; BaO was often below the EMPA detection limit. MnO content varies from 0.24 to 0.62 wt%. Some of the ocelli are texturally composite, including both smaller dolomite-ankerite crystals and larger well-developed magnesite-siderite ones, the latters mainly occuring in the inner portions; some others are instead constituted of sole dolomite-ankerite crystals (Fig. 9).

An intriguing topic in the study of carbonates in the magmatic rocks is the determination of their primary (carbonatitic) origin, since late-stage hydrothermal precipitations and alteration processes can lead to misleading interpretations. If the carbonate ocelli represent/belong to a primary melt, the intimate association between lamprophyric and carbonatitic melts would have been confirmed also in the Predazzo camptonites, and liquid immiscibility processes probably drove the generation of the carbonate ocelli globular structures (Rock, 1991; Le Roex & Lanyon, 1998; Leat *et al.*, 2000; Vichi *et al.*, 2005). If not, their nature would be linked to the occurrence of late-stage hydrothermal processes.

From a textural point of view, carbonate ocelli of Predazzo camptonites are characterized by: (i) spherical shape, easily distinguishable from secondary-filled amygdalae, elongated in shape; (ii) flow-aligned tangential growth of high-temperature-forming silicates (plagioclase, amphibole and/or clinopyroxene); (iii) lack of more typically hydrothermal minerals, such as

zeolites (Fig. 9). According to Vichi *et al.* (2005) and Gozzi *et al.* (2014), all these features speak in favour of the primary magmatic nature of carbonate ocelli, and, therefore, of the existence of carbonatitic-like droplets within the silicate melt.

To solve the primary *vs.* secondary nature of carbonates, some authors proposed that a low SrO contents (<0.6 wt%) suggest a late-stage origin (Hay & O'Neil, 1983; Hogarth, 1989; Leat *et al.*, 2000), whereas some others hypothesized that carbonates with SrO >0.3 wt.% and MnO >0.2 wt.% could be considered as primary (Vichi *et al.*, 2005). On the other side, it should be noticed that magnesite-siderite series in carbonatitic complexes often display low SrO contents (Buckley & Woolley, 1990; Zaitsev *et al.*, 2004). Plotting our data in a CaO/MgO vs. SrO+MnO space, which discriminates between high temperature and late-stage secondary carbonates (Vichi *et al.*, 2005), a positive correlation is displayed by most of the magnesite-siderite crystals, whereas an almost constant CaO/MgO accompanies a large scattered (SrO+MnO) sum for all the dolomite-ankerite grains (Fig. 9). Such a feature would be consistent with a late-stage crystallization of the magnesite-siderite crystals, and a magmatic origin for the dolomite-ankerite grains (Vichi *et al.*, 2005). This hypothesis is also supported by the occurrence of magnesite-siderite-free ocelli in the Predazzo camptonites. A similar combination has been also recognized by Leat *et al.* (2000) in carbonate ocelli inside the Middle Jurassic lamprophyres of the Ferrar region (Antarctica): according to these authors, an earlier formation of magmatic calcite-dolomite series was followed by the late-stage deposition of Fe-rich and Sr-poor carbonates towards the core of the ocelli. Such an interpretation, well fitting both the chemical and textural features of the carbonate ocelli of Predazzo lamprophyres, lead us to hypothesize that: i) dolomite-ankerite crystallization was primary (magmatic), likely derived from a carbonatitic-like melt that coexisted with the lamprophyric one; ii) the magnesite-siderite precipitation probably occurred during late-stage hydrothermal fluid circulation.

AGE AND ISOTOPIC SIGNATURE OF PREDAZZO CAMPTONITES

$^{40}Ar/^{39}Ar$ geochronology

The $^{40}Ar/^{39}Ar$ incremental heating method was applied to amphibole and feldspar separates from two different camptonite samples (FF2 and FF37). Results, and age spectra are shown in Fig. 10. Sample FF2 (plagioclase): The data defined a plateau (>90% ^{39}Ar, n = 16, MSWD 0.9) with an age of 218.90 ± 0.59 Ma. The younger discordant steps in the age spectrum likely related to alteration of the plagioclase. Sample FF37 (amphibole): The data defined a plateau (>50% ^{39}Ar, n = 6, MSWD 1.98) with an age of 219.70 ± 0.73 Ma. Younger apparent ages in the early steps of amphibole age spectrum, concomitant with high K/Ca ratios, were probably due to secondary alteration. The plagioclase and amphibole age are in good agreement and define a crystallisation age for the Predazzo camptonites of 219.22 ± 0.46/0.73 Ma (2σ; analytical/full systematic uncertainties). These results show that the emplacement of the lamprophyric dykes took place ~19 Ma later than that of the Predazzo Intrusive Complex (U-Pb zircon age of 238.075 ± 0.087, Storck *et al.*, 2018).

$^{87}Sr/^{86}Sr$ and $^{143}Nd/^{144}Nd$ isotopes

Whole-rock $^{87}Sr/^{86}Sr$ and $^{143}Nd/^{144}Nd$ isotopic ratios were measured on representative samples among the Predazzo lamprophyres (Table 1). Strontium isotopic ratios range between 0.7044 and 0.7064, whereas Nd isotopic compositions vary between 0.51277 and 0.51280. Initial isotopic ratios, respectively named $^{87}Sr/^{86}Sr_i$ and $^{143}Nd/^{144}Nd_i$, were corrected to an age of 220 Ma, in accordance with the $^{40}Ar/^{39}Ar$ dating results. The Predazzo samples are characterized by $^{87}Sr/^{86}Sr_i$ values ranging between 0.7033 and 0.7040, for a $^{143}Nd/^{144}Nd_i$ range of 0.51260-0.51265 (Fig. 11). No systematic isotopic variations between the camptonites and the bostonites were recognized. The isotopic data, in accordance to what hypothesized by Marrocchino *et al.* (2002), highlight a discrepancy between the isotopic signature of the lamprophyres and their "hosting" Predazzo Intrusive Complex (Casetta *et al.*, 2018*a*). The lamprophyres isotopic

signature lies in fact between the DMM and the EM I mantle end-members, in contrast to that of the PIC, purely EM I-like (Fig. 11).

LAMPROPHYRES DIFFERENTIATION

The differentiation processes of worldwide alkaline lamprophyres are often testified by the occurrence, both at local (ocelli, veins, globules) and regional scale (coeval dykes/plutons), of co-magmatic intermediate/felsic rocks, mainly foid-syenitic in composition. In other cases, the efficiency of differentiation is evidenced by the intimate association between camptonites and bostonites (Rock, 1987; 1991). The occurrence of both camptonites and bostonites in the Predazzo dykes swarm, together with the mineral phase compositional variations, suggests that differentiation processes played a predominant role in this magmatic system. The above mentioned Ni, Co, Cr decrease and the contemporary Zr, Sr increase at decreasing MgO (Fig. 4) speak in favour of the occurrence of fractional crystallization (FC) processes in the Predazzo lamprophyres magmatic system. The absence of a significant crustal contribution is supported by the high whole rock MgO, Cr and Ni contents, the presence of forsteritic olivine and the initial $^{87}Sr/^{86}Sr$ and $^{143}Nd/^{144}Nd$ values that approach the DMM isotopic component. These features point towards a mantle-derived origin for our samples, in accordance with most of the worldwide alkaline lamprophyres (Rock, 1991). Additionally, the absence of a Sr isotopic increase between camptonites and bostonites rules out significant interaction with the crust (i.e. assimilation/contamination) during differentiation.

Using the simple Shaw (1970) equation, $C_L = C_0 * F^{(D-1)}$, an approximate evaluation of the fractional crystallization (FC)-related residual melt percentage (F) from a starting primitive camptonitic composition (C_0) towards an evolved bostonitic one (C_L) can be obtained by considering, to the first approximation, the partition coefficients weighted for the mineral fractionation percentage (D) equal to zero. The application of such equation to the most incompatible element (i.e. Zr), modeled that bostonites were generated by ~40% fractional

crystallization from a starting camptonitic melt. Accordingly, major element FC vectors (Fig. 12) show that a 35% fractional crystallization of an assemblage made of olivine (19.1%), clinopyroxene (53.4%), amphibole (19.1%) and Ti-magnetite (8.4%) accounts for the bostonite composition from a starting primitive camptonitic magma.

T-P-fO_2 CONDITIONS OF CRYSTALLIZATION AND WATER CONTENT OF LAMPROPHYRIC MELTS

The determination of T-P-fO_2 parameters of lamprophyric systems is challenging. To retrieve the physico-chemical crystallization conditions of the melts, we applied several thermo-, oxy-barometric and hygrometric equations to the main coexisting mineral phases of camptonites and bostonites, such as clinopyroxene, Ti-magnetite and amphibole.

Clinopyroxene and Ti-magnetite crystallization conditions

Since the composition of lamprophyric melts is, by definition, higher in volatiles with respect to alkali basalts and basanites, temperature and pressure of clinopyroxene crystallization were determined by the clinopyroxene-only H_2O-independent equations of Putirka (2008). Equilibrium between clinopyroxene phenocrysts and camptonitic melt was evaluated by means of their Fe-Mg partitioning, assuming a $^{Cpx\text{-}Liq}Kd_{Fe\text{-}Mg}$ of 0.26±0.05 (Akinin *et al.*, 2005), which ideally reflect clinopyroxene equilibrium conditions in an alkali-dominated basic melt (i.e. camptonites; Ubide *et al.* (2014). Results indicated that most of the clinopyroxene phenocrysts were not in equilibrium with their host camptonitic melt (Mg# 59-65), requiring instead a more evolved melt. The disequilibrium is also supported by the compositional zoning between cores (Mg# 82) and rims (Mg# 68) of many crystals, as well as by the dusty reaction zones of the larger phenocrysts. The few crystals in equilibrium with their whole rock composition were used for the thermobarometric calculations. Pressure and temperature were calculated from the equations 32a and 32d of Putirka (2008) respectively, in turn derived by the *T*-dependent

barometer and the *P*-independent thermometer of Putirka *et al.* (1996). The obtained values indicated that clinopyroxene crystallized between 6.4 and 2.3 kbar, in a *T* interval of 1124 to 1060°C (Table 8).

The oxygen fugacity of the lamprophyres was then calculated by means of the oxy-barometer of Ishibashi (2013), based on the Fe^{2+}/Fe^{3+} partitioning between spinel and melt. According to the values obtained by the clinopyroxene-melt thermobarometers, a *T-P* range of 1100-1050°C and 5.0 kbar was considered representative to apply the Ishibashi (2013) equation to the Ti-magnetite crystals in the camptonitic melt. Results yielded an oxygen fugacity interval of -8.3/-10.0 log fO_2 at 1100°C, and a -9.4/-11.0 log fO_2 range at 1050°C, thus varying between -1 and +1 FMQ (Table 8).

Amphibole crystallization conditions

The *T-P* conditions of amphibole crystallization and the H_2O content of the coexisting melt were calculated by means of the amphibole-melt thermobarometric equations of Putirka (2016) and the single-mineral hygrometer of Ridolfi *et al.* (2010), respectively. The equilibrium between amphibole crystals and camptonitic/bostonitic melts was evaluated by means of the *T*- and *P*-independent $^{Amph\text{-}Liq}Kd_{Fe\text{-}Mg}$ exchange coefficient, which should be 0.28±0.11 in conditions of equilibrium (Putirka, 2016).

The analysed amphiboles resulted not in equilibrium with the camptonitic melt, having an Mg/Fe ratio slightly lower with respect to their host rock ($^{Amph\text{-}Liq}Kd_{Fe\text{-}Mg}$ = 0.42-0.89); on the other side, equilibrium conditions were attained by some crystals in the bostonitic melt ($^{Amph\text{-}Liq}Kd_{Fe\text{-}Mg}$ = 0.29-1.0). As expected, *Type 4* xenocrysts and *Type 5* amphiboles cores yielded extreme disequilibrium conditions with respect to camptonitic and bostonitic melts, with $^{Amph\text{-}Liq}Kd_{Fe\text{-}Mg}$ values as high as 1.22 and 1.94, respectively.

The single-mineral hygrometer of Ridolfi *et al.* (2010) indicates that amphibole crystallization generally occurred at a water contents of 6.7-8.1 wt% in the camptonitic melt, and 5.8-8.4 wt%

in the bostonitic one (Table 8). Higher values were obtained from the *Type 4* xenocrysts and *Type 5* amphibole cores, which yielded H_2O contents up to 8.9 and 9.8 wt%, respectively. By considering the amphiboles in equilibrium with their host rock (bostonitic) composition, a water content range of 5.8-6.8 wt% is obtained.

Temperature and pressure conditions of amphibole crystallization were calculated by applying the Putirka (2016) *P*-independent thermometer (Equation 5) and the *T*-independent, H_2O-dependent barometer (Equation 7b). The H_2O values obtained by the Ridolfi *et al.* (2010) hygrometer were used as input for the barometer. Results indicated that amphibole crystallization in the camptonitic/bostonitic melt occurred in a *T* range of 1074 to 927°C, at *P* decreasing from 12.3 to 4.7 kbar (Table 8). The highest *P* are instead yielded by *Type 4* xenocrysts (11.2-12.3 kbar) and *Type 5* amphiboles cores (9.6-11.3 kbar), at corresponding crystallization *T* of 1008-1060°C and 927-983°C, respectively (Table 8). It is worth noting that, due to the significant disequilibrium between these crystals and the melt composition, these values should be considered with caution. If we only consider the amphibole in equilibrium with the (bostonitic) melt, a *T-P* interval of 1048-1001°C and 6.9-4.7 kbar is obtained: this can be likely considered representative of the shallower conditions of crystallization of amphibole in the magmatic system. The deeper crystallization conditions of amphibole can be roughly approached by some *Type 1*, *Type 2* and *Type 3* crystals which are close to the equilibrium conditions to the host camptonite ($^{Amph\text{-}Liq}Kd_{Fe\text{-}Mg}$ = 0.42-0.46), and yield higher *P* (9.2-11.6 kbar) and T (up to 1067°C).

Nevertheless, the calculated *T-P* range of amphibole crystallization (927-1074°C) is in good agreement with the experimental simulations proposed by Pilet *et al.* (2010), who demonstrated that kaersutite crystallization can start at 1130°C and 15 kbar in a volatile-enriched (5-6 H_2O wt%) basanitic melt, thus in conditions similar to those of Predazzo camptonites.

If combined to the clinopyroxene-melt thermobarometric results, these *T-P* values (Table 8) suggest that the crystallization of amphibole and clinopyroxene occurred continuously at least

between 6.9 and 2.3 kbar, a *T* decreasing from 1124 to ~1000°C, in a melt with H_2O content ≥ 5.8-6.8 wt%.

Interpretation of amphibole textures

A correlation between the obtained *T-P* and H_2O results and the previously identified textures enable us to infer amphibole crystallization processes.

The homogeneous composition of *Type 1* amphibole cores, close to the equilibrium with the camptonitic melt ($^{Amph\text{-}Liq}Kd_{Fe\text{-}Mg}$ = 0.42-0.58) records a growth at high *T-P* (1023-1069°C; 9.2-11.6 kbar), at H_2O content of the melt ranging between 7.2 and 8.5 wt%. The crystallization of *Type 1* amphiboles continued during differentiation of the melt towards a bostonitic composition, where crystals grew in equilibrium ($^{Amph\text{-}Liq}Kd_{Fe\text{-}Mg}$ = 0.32-0.36) at *T-P* down to 948-1042°C and 6.2-9.8 kbar, and water content of 6.5-7.7 wt%.

Type 2 crystal cores, in marked disequilibrium with the camptonitic melt ($^{Amph\text{-}Liq}Kd_{Fe\text{-}Mg}$ = 0.73-0.80), record a *T-P* crystallization interval of 997-1009°C and 8.9-9.2 kbar, at 6.8-7.1 H_2O wt% in the melt. The rounded shape of both *Type 1* and *Type 2* amphibole cores, especially in the camptonitic rocks, reflects an event of simply dissolution after reaction with a melt phase undersaturated in amphibole. Subsequently, the melt differentiated and re-saturated in amphibole, allowing the precipitation of the ferri-kaersutitic rims at slightly lower *T-P* and H_2O contents (1038-1067°C; 7.4-9.0 kbar; 6.8-7.5 H_2O wt%; Fig. 7b).

The magnesio-hastingsitic (Mg# = 73-74) overgrowth in both *Type 1* and *Type 2* crystals is similar to the diopsidic bands identified by Petrone *et al.* (2018) in the clinopyroxenes from Stromboli volcano (Aeolian Islands). Accordingly, this level probably formed in response of new pulse of primitive-type melts that introduced additional high *T* components (Mg and Ca) in the magmatic system. An abrupt *T* increase (1051-1071°C) is recorded in this intermediate overgrowth (Figg. 7a and 7b), which can provide the evidence of small-scale mixing dynamics between differentiated and primitive batches inside the magmatic system.

Dusty zones of *Type 3* amphibole cores were instead the result of pseudomorphic replacement by interface-coupled dissolution-precipitation processes, resulting in Ti-magnetite, plagioclase and clinopyroxene formation at the interface (Ruiz-Agudo *et al.*, 2014). The overgrowth of a newely formed rim in *Type 3* crystals is likely concomitant with the formation of *Type 1* and *Type 2* amphibole rims, and in fact approaches the equilibrium conditions with the bostonitic melt ($^{Amph\text{-}Liq}Kd_{Fe\text{-}Mg}$ = 0.34-0.69). The crystallization conditions of *Type 3* amphibole rims are the following: *T* = 1057-1063°C (camptonite) to 961-1030°C (bostonite); P = 8.7-9.8 kbar (camptonite) to 6.3-7.5 kbar (bostonite); melt H_2O content = 6.4-7.8 wt% (both camptonite and bostonite).

Type 4 xenocrysts probably represent relicts of larger crystals of deep crustal origin, brought to the surface by the ascent of lamprophyres. The incipient alteration and resorption features of their cores suggest disequilibrium with the hosting melt, as also confirmed by the high $^{Amph\text{-}Liq}Kd_{Fe\text{-}Mg}$ (1.22). High *P* (up to 12.3 kbar) and water content (8.9 H_2O wt%) were in fact obtained by the thermobarometric calculations, at relatively low *T* (1008°C). Their dusty portions probably formed as consequence of interface-coupled dissolution-precipitation. The outermost rim, compositionally analogous most phenocryst rims and groundmass crystals (*Type 1, Type 2* and *Type 3*) represent a late overgrowth approaching the equilibrium with the magmatic system ($^{Amph\text{-}Liq}Kd_{Fe\text{-}Mg}$ down to 0.61), as evidenced by the similar crystallization *T* (1042-1060°C), *P* (11.2 kbar) and H_2O (8.3 wt%).

The texture of *Type 5* amphiboles is composed of a Ti-rich ferri-sadanagaitic to Ti-rich ferro-ferri-sadanagaitic (Mg# = 29-39, Fig. 7e) core and by a Ti-rich magnesio-hastingsitic rim. The sharp edges and optical continuity between cores and rims, as well as the absence of resorption zones, suggest that this texture is a consequence of a Ti-rich magnesio-hastingsite overgrowth around preexisting crystals. The peculiar composition of *Type 5* crystal cores is rare, even in lamprophyric rocks (Rock, 1991), and for this reason it is difficult to attribute them a specific origin, making it necessary the development of further studies to constrain their nature. The

high $^{Amph\text{-}Liq}Kd_{Fe\text{-}Mg}$ (1.18 to 1.94) of the cores indicate a significant disequilibrium with respect to the bostonitic rock, implying that they would attain equilibrium only in an extremely differentiated melt. The thermobarometric results, which should be considered with caution, suggest a high *P* (9.6-11.3 kbar) and low *T* (927-983°C) crystallization, at high water content (up to 9.8 wt%). The Ti-rich magnesio-hastingsitic rims are similar in composition to the other phenocrysts and groundmass crystals and represent a subsequent growth in equilibrium with the bostonitic melt ($^{Amph\text{-}Liq}Kd_{Fe\text{-}Mg}$ = 0.29-0.55), at *T* of 977-1048°C, *P* of 4.9-6.9 kbar and water content down to 5.8 wt%.

The observed simple dissolution and pseudomorphic replacement textures indicate a very dynamic regime of the lamprophyres magmatic system. Chemical zoning associated with dissolution-reprecipitation textures suggest that amphibole stability was affected by *T* changes due to small scale mixing between variably differentiated and/or volatile rich melts. The repeated occurrence of such small scale mixing processes resulted in fact in multiple and abrupt changes of amphibole liquidus conditions during lamprophyre differentiation.

LAMPROPHYRE MANTLE SOURCE AND MELTING MODEL

The HFSE distribution of the less fractionated Predazzo camptonites well fit the OIB field in the Th_N vs. Nb_N tectonic discrimination diagram (Saccani, 2015), highlighting a clear genetic link to a within-plate setting. Additionally, the camptonite-bostonite trend with decreasing Mg# on the same diagram is consistent with a significant involvement of subsequent fractional crystallization processes, in accordance to what modelled above (Fig. 13). The alkaline within-plate signature of Predazzo lamprophyres is clearly evidenced by the Ti/Y vs. Nb/Y and Zr/Y vs. Zr diagrams (Fig. 13; Pearce & Norry, 1979; Pearce, 1982), as well as by the Th-Hf-Ta and Zr-Nb-Y ternary diagrams (Fig. 13; Wood, 1980; Meschede, 1986).

An intriguing topic is the nature of the mantle source from which Predazzo lamprophyres were derived, especially in light of their HFSE/REE distribution and Sr-Nd isotopic signature.

Indirect evidence of the minimum depth of segregation is provided by the lherzolite xenoliths, which record a re-equilibration process at about 45 km of depth, in the spinel stability field (Carraro & Visonà, 2003). The Zr/Y (6-11), Lu/Hf (0.07-0.12) and Dy_N/Yb_N (1.1-1.7) ratios of Predazzo lamprophyres suggest that garnet played a significant role during melting in their mantle source, as also suggested by Pinzuti *et al.* (2013) for Asal Rift magmas. On the other side, the La_N/Yb_N and Gd_N/Yb_N ratios of the less fractionated camptonites are not very high, suggesting that their source differs from those of the "typical" alkaline lamprophyres and OIB magmas (Sun & McDonough, 1989; Rock, 1991). According to the Sr-Nd isotopic data (Fig. 11), lamprophyres were generated by a depleted mantle, as also confirmed by the Nb/La vs. La/Yb diagram of Smith *et al.* (1999), which indicates that a marked contribution of asthenosphere was required for their generation (Fig. 14).

On the basis of these contraints, we tentatively modelled the nature of the mantle domain from which Predazzo lamprophyres were segregated by applying non-modal batch melting equations (Shaw, 1970). To account for the HFSE and REE budget of our samples, several mantle melting domains were used as starting point of our simulations. The modal composition and melting proportion of each of the considered mantle sources are reported in Table 9. A first discrimination between the role of spinel and garnet in the hypothetical source was put forward by using as starting mantle domains a spinel- and a garnet-bearing fertile lherzolites (Primordial Mantle, PM composition; Sun & McDonough, 1989). Consistent with the Sr-Nd isotopic data, a melting path was also proposed by using as starting source a depleted mantle composition (DMM, Workman & Hart, 2005). According to the obtained melting curves, none of the chosen starting component was able to obtain the Sm/Yb ratio of Predazzo lamprophyres (Fig. 14). Their Gd/Yb ratio was better approximated by the melting curve of the garnet-bearing source, even if the match was not perfect (Fig. 14). Consequentely, amphibole and/or phlogopite were introduced as additional components of the starting mantle domains in our simulations. The calculated curves showed that both a garnet-amphibole-, a garnet-phlogopite- and a garnet-

spinel-amphibole-bearing sources were able to account for the Sm/Yb and Gd/Yb ratios of our samples (Fig. 14). However, the REE patterns obtained by melting the garnet-phlogopite-lherzolite were anomalously HREE-enriched with respect to Predazzo lamprophyres, being therefore considered not suitable for our model. Among the melting trends of garnet-amphibole- and the garnet-spinel-amphibole-bearing sources, the former better reproduced the features of the less fractionated Predazzo lamprophyres, both in the Sm/Yb, La/Yb and Gd/Yb ratios and in the REE pattern (Fig. 14). Accordingly, Predazzo lamprophyres could have been generated by low melting percentages (1.0 to 2.5%) of a garnet-amphibole-bearing lherzolite, with a fertile PM starting composition (Sun & McDonough, 1989).

Such mantle source modal composition and melting degrees are like those proposed by Batki *et al.* (2014) to explain the generation of Ditrau lamprophyres. However, the starting composition of the Predazzo lamprophyres mantle source resulted more depleted than the Ditrau one, as testified by the REE-enriched astenospheric composition (EAM, Seghedi *et al.*, 2004) invoked by Batki *et al.* (2014) to explain the genesis of the latters. The presence of a garnet-bearing mantle source enriched in LILE and volatiles and with an astenospheric signature was also proposed by Stoppa *et al.* (2014) to model the genesis of the Cretaceous to Oligocenic alkaline/ultramafic lamprophyres of Central-Southern Italy, whose REE patterns are strongly LREE-enriched and HREE-depleted with respect to the Predazzo ones.

The involvement of amphibole and garnet during melting was required to simulate the relatively low LREE/HREE ratios of Predazzo lamprophyres, as well as to get rid of their H_2O-CO_2-alkali-rich nature. Considering that the spinel-garnet transition in a continental lithospheric setting occurs at 60-90 km (20-30 kbar; Takahashi & Kushiro, 1983; Falloon & Green, 1988; Kinzler & Grove, 1992; Robinson & Wood, 1998; Pinzuti *et al.*, 2013), we can hypothesize that the melting region of Predazzo lamprophyres was located at depth >60-70 km. On the other side, the amphibole stability limit in the mantle is limited to ~30 kbar (Frost, 2006; Fumagalli *et al.*, 2009; Tumiati *et al.*, 2013; Mandler & Grove, 2016), suggesting that a depth of 70-80

km can be considered appropriate. Similar depths are also consistent with those proposed by Hammouda & Keshav (2015), according to whom carbonatite and silicate melts can coexist between 20 and 26 kbar (ca. 60-80 km) along the convecting mantle adiabat (asthenosphere).

GEODYNAMIC IMPLICATIONS

The magmatism of the Dolomitic Area

The late-stage occurrence of alkaline lamprophyric dykes in intrusive complexes often acquires a double significance, since they do not only act as younger chronological boundary of the magmatic episode, but are also the most primitive magma types, less contaminated by the crust (Rock, 1991). In the case of the Predazzo area, several authors have suggested that the alkaline lamprophyric dykes are strictly related to that of the main Predazzo Intrusive Complex (Lucchini *et al.*, 1969; 1982; Carraro & Visonà, 2003). However, the new geochronological and geochemical data presented in our study lead us to interpret that alkaline lamprophyres belongs to an independent magmatic pulse. The obtained $^{40}Ar/^{39}Ar$ age results (from 218.90 ± 0.59/0.66 to 219.70 ± 0.73/0.85 Ma; Fig. 10) show in fact that the alkaline lamprophyres emplaced about 17-20 Ma later than the Predazzo Intrusive Complex (238.075 ± 0.087 Ma, Storck *et al.*, 2018). Since the entire Ladinian volcano-plutonic event in the Dolomitic Area lasted from 239.04±0.04 to 237.77±0.05 Ma (Brack *et al.*, 1996; Mundil *et al.*, 1996; Mietto et al., 2012; Abbas *et al.*, 2018; Storck *et al.*, 2018; Wotzlaw *et al.*, 2018), it is evident that the camptonitic/bostonitic dykes at Predazzo represent an independent, subsequent magmatic event. The chronological gap is also reinforced by the geochemical discrepancies: despite showing a K-affinity comparable to that of the high-K calc-alkaline to shoshonitic volcano-plutonic rocks of the entire Dolomitic Area (Fig. 3; Bonadiman *et al.*, 1994; Casetta *et al.*, 2018*a*; 2018*b*), lamprophyres are characterized by peculiar trace element profiles and Sr-Nd isotopic signature (Figg. 5 and 11). In fact, whereas the Ladinian high-K calc-alkaline to shoshonitic rocks display the typical subduction-related incompatible element patterns, alkaline lamprophyres are

typified by the lack of any Ta-Nb-Ti and U-Th negative anomalies, suggesting the involvement of an OIB-like component in their mantle source. Moreover, the $^{87}Sr/^{86}Sr_i$ and $^{143}Nd/^{144}Nd_i$ signature of camptonites/bostonites points towards a genesis from a mantle source more depleted than the EM I-like source that produced the Ladinian high-K calc-alkaline to shoshonitic rocks. As shown in Fig. 11, in fact, they plot close to the DMM end-member (Workman & Hart, 2005), suggesting that a significant contribution of the asthenospheric mantle was involved in their genesis. This feature confirms a time-related progressive depletion of the mantle source beneath the Dolomitic Area during Middle-Late Triassic, as already hypothesized for the source of Predazzo Intrusive Complex (PIC; Casetta *et al.*, 2018*a*). Our study indicates that the magmatic activity in the Dolomitic Area was not confined to the Ladinian, but re-activated at about 218.5-220.5 Ma, with the emplacement of a volumetrically reduced alkaline pulse generated from a $^{143}Nd/^{144}Nd$-enriched mantle domain. At shallow depth, the ascent of such volumetrically reduced melts was probably favoured by extensional-trastensional dynamics, to which lamprophyres are often associated (e.g. Scarrow *et al.*, 2011, and reference therein). The (if any) relationships between Predazzo lamprophyres and the Triassic NE-SW transtensive-transpressive regimes of the Dolomitic Area (Doglioni, 2007; Doglioni & Carminati, 2008; Abbas *et al.*, 2018), however, were never modelled, and would require further studies, especially in the light of the new age data.

Late-stage magmas or alkaline precursors?

When considered at a geodynamic scale, the significance of the lamprophyric magmatism at Predazzo is intriguing, since several magmatic episodes with variable geochemical affinity shaped the Southalpine-Austroalpine and Carnic-Dinaric domains from Permian to Middle-Late Triassic. The most similar and chronologically closer magmatic occurrence was documented in the Ditrau Alkaline Massif (Carpathians), where late-stage alkaline lamprophyres (camptonites) intruded a Middle-Triassic (231-227 Ma) alkaline multi-pulse

intrusion (Dallmeyer *et al.*, 1997; Morogan *et al.*, 2000; Pana *et al.*, 2000; Batki *et al.*, 2014; Pál-Molnár *et al.*, 2015). The major and trace elements and isotopic similarities between the Ditrau lamprophyres and the intrusive complex led to interpret them as the parental magmas of the intruded plutonic suite (Batki *et al.*, 2014). Such a model cannot be applied to the Predazzo case, where the geochronological and geochemical discrepancies between the alkaline lamprophyres and the PIC rule out any possible connection between the camptonites/bostonites and the trachybasaltic/shoshonitic rocks. Notwithstanding a slight relative depletion in Th, U, Nb, Zr, and LREE, with respect to Ditrau Alkaline Massif, Predazzo lamprophyres have comparable Sr-Nd isotopic signature (Figg. 5 and 11), suggesting that similar mantle sources were involved in their genesis. According to Batki *et al.* (2014), the latters were generated by 1-4% partial melting of a garnet+amphibole enriched lherzolite, with the contribution of asthenospheric HIMU-OIB-like components. This melting process took place in an early extensional phase of the Middle Triassic to Jurassic rifting that separated the Getic microplate from the Bucovinian margin (Batki *et al.*, 2014), thus representing the Alpine Tethys rift portion located northward of the Meliata basin (Stampfli *et al.*, 2002; Stampfli, 2005). Precursors of the Tethyan opening were also documented in the Brescian Alps, not far from the Dolomitic Area, where intra-plate tholeiitic lavas and dykes with depleted Sr-Nd isotopic signature emplaced almost simultaneously with the Predazzo lamprophyres, at about 217±3 Ma (Cassinis *et al.*, 2008).

Coeval (220-225 Ma) magmatic occurrences were also recognized in the Western Alps, where alkaline dykes, generated by an upwelling mantle with significant astenospheric contribution, emplaced in the Finero area (Stähle *et al.*, 1990; 2001). Moreover, ages of 215±35 Ma and 220±4 Ma were determined by Morishita *et al.* (2008) and Malitch *et al.* (2017), respectively, for the formation of the metasomatic apatite-rich and chromitite layers in the Finero peridotite. This time overlap, fostered by the Sr-Nd isotopic analogies between the alkaline dykes and the apatite-rich layers, led several authors (Ferrario & Garuti, 1990; Morishita *et al.*, 2003; 2008;

Zaccarini *et al.*, 2004) to associate all these occurrences to a unique alkaline-carbonatitic magmatic event. The generation of such H_2O-CO_2-rich fluids was attributed to mantle upwelling dynamics in a continental rifting setting (Zaccarini *et al.*, 2004).

The 219.22 ± 0.46/0.73 Ma occurrence of alkaline lamprophyres at Predazzo can be easily incorporated in such a context, taking into account that their Sr-Nd isotopic signature totally overlap those of the alkaline dykes and the apatite-rich layers at Finero (Fig. 11; Stähle *et al.*, 1990; 2001; Morishita *et al.*, 2008). The less differentiated alkaline dykes intruded at Finero (Stähle *et al.*, 2001) are also characterized by trace element patterns comparable to those of Predazzo lamprophyres, except for Nb, Ta and Zr, slightly enriched in the former. A marked U-Th depletion characterizes both the Predazzo lamprophyres and the alkaline dykes at Finero, and their REE pattern almost totally overlap, as testified by the Gd_N/Yb_N (1.9) and Dy_N/Yb_N (1.4) ratios of the latters. Furthermore, the Sr-Nb enrichment of Predazzo lamprophyres well matches the main features of the apatite-bearing assemblages at Finero (Zanetti *et al.*, 1999; Fig. 11), confirming the involvement of a carbonate-rich component in their genesis. This is also supported by the presence, in Predazzo lamprophyres, of carbonate ocelli with a dolomite-ankerite composition comparable to that of the interstitial dolomite grains in the Finero peridotite (Zanetti *et al.*, 1999).

According to our findings, Predazzo lamprophyres can be considered as an expression of the 215-225 Ma alkaline-carbonatitic magmatism that intruded the subcontinental mantle portion beneath the Southern Alps (Ferrario & Garuti, 1990; Stähle *et al.*, 1990; 2001; Zanetti *et al.*, 1999; Morishita *et al.*, 2003; 2008; Zaccarini *et al.*, 2004; Matsumoto *et al.*, 2005; Raffone *et al.*, 2006; Malitch *et al.*, 2017). This magmatic pulse, characterized by mantle-upwelling signature, is well distinguished from the previous, subduction-related, K- and LILE-rich metasomatic episode that produced amphibole and phlogopite in the Finero peridotite (Fig. 11; Coltorti & Siena, 1984; Morishita *et al.*, 2003; 2008; Malitch *et al.*, 2017). According to the U-Pb zircon ages (190-180 Ma and 230-180 Ma) proposed by Zanetti *et al.* (2016) and Langone

et al. (2018), the alkaline-carbonatitic metasomatism affected the subcontinentl mantle immediately prior to its exhumation, which was precisely related to the extensional stages of the Alpine Tethys rift.

More than a late-stage episode connected to the Middle Triassic high-K calc-alkaline/shoshonitic magmatism, the generation of Predazzo lamprophyres should be therefore considered, together with the Ditrau lamprophyres, the Brescian Alps basalts and the Finero alkaline-carbonatitic magmas, as a Late Triassic precursor of the Alpine Tethys rifting event. This hypothesis is supported by their depleted Sr-Nd isotopic signature, consistent with a genesis from a mantle source influenced by an asthenospheric contribution. Further evidence is given by the incompatible elements pattern of the alkaline lamprophyres that, when compared to the Ladinian shoshonitic rocks of the Dolomitic Area, appear depleted in U, Th, K and La, more than enriched in Nb and Ta (Fig. 5). Such a feature is consistent with the progressive shift of the magmatism from orogenic-like to anorogenic, and thus to a progressive evolution of the subcontinental mantle source towards a more depleted, asthenosphere-related nature.

CONCLUSIVE REMARKS

The petrological, geochronological and isotopic study of the Predazzo alkaline lamprophyres enabled us to provide new insights on the geodynamic evolution of the Dolomitic Area and the Southern Alps during Middle-Late Triassic. The most relevant findings can be summarized as follows:

1. The compositional spectrum of Predazzo alkaline lamprophyres ranges from camptonites to bostonites, the latters being produced by 35-40% fractional crystallization of olivine, clinopyroxene, amphibole and Ti-magnetite from an initial primitive camptonitic melt.
2. Thermo-, oxy-barometric and hygrometric calculations based on clinopyroxene, amphibole and Ti-magnetite composition suggest that their crystallization occurred in continuity at least between 6.9 and 2.3 kbar, a T decreasing from 1124 to ~1000°C. The oxygen fugacity

of the magmatic system varied between -1 and +1 FMQ, whereas the H_2O content of the lamprophyric melts resulted ≥ 5.8-6.8 wt%, decreasing with decreasing temperature.

3. Amphibole textural and compositional features suggest that the lamprophyre magmatic system was subjected to small scale mixing between variably differentiated and/or volatile rich melts during differentiation, as testified by the variable presence of dissolution-reprecipitation textures and pseudomorphic replacements. Moreover, the occurrence, composition and textural features of carbonate-bearing ocelli suggest that a carbonatitic melt was intimately associated to the alkaline lamprophyric one.
4. $^{40}Ar/^{39}Ar$ ages of Predazzo alkaline lamprophyres demonstrated that they emplaced between 218.90 ± 0.59/0.66 and 219.70 ± 0.73/0.85 Ma (Late Triassic; $^{40}Ar/^{39}Ar$; 2σ; analytical/full systematic uncertainties), suggesting an origin unrelated to the short-lived Ladinian high-K calc-alkaline/shoshonitic magmatism of the Predazzo-Mt. Monzoni intrusions in the Dolomitic Area.
5. The otherness of the alkaline lamprophyres with respect to the Ladinian rocks is fostered by the absence of Ta-Nb-Ti negative anomalies, the presence of U-Th negative peaks, and their HFSE distribution, which point towards a genesis in an intra-plate geodynamic setting, from a garnet-bearing mantle source. This is also confirmed by their $^{87}Sr/^{86}Sr_i$ and $^{143}Nd/^{144}Nd_i$ depleted signature, consistent with a depleted mantle contribution in their source, in contrast to the pure EM I-like signature of the Predazzo-Mt.Monzoni Ladinian intrusions, which was related to a subduction-modified mantle.
6. Mantle melting models suggest that low melting percentages (1.0-2.5%) of a fertile garnet-amphibole-bearing lherzolite can account for the generation of Predazzo lamprophyres. The melting region was probably located between 70 and 80 km of depth.
7. Predazzo lamprophyres are temporally, spatially and geochemically correlable to several magmatic occurrences of the Southern Alps-Carpathians area, including: (i) the Ditrau alkaline lamprophyres (Batki *et al.*, 2014); (ii) the Brescian Alps intra-plate tholeiitic lavas

and dykes (Cassinis *et al.*, 2008); (iii) the alkaline dykes, the apatite-rich and the chromitite layers in the Finero peridotite (Ferrario & Garuti, 1990; Stähle *et al.*, 1990; 2001; Morishita *et al.*, 2003; 2008; Zaccarini *et al.*, 2004; Malitch *et al.*, 2017). A further geochemical and geochronological comparison with the alkaline magmas at Karawanken (Austroalpine domain, Visonà & Zanferrari, 2000) is instead required, since the only available age data for this complex (230±9 Ma, Lippolt & Pidgeon, 1974) overlaps with both the ~237 Ma high-K calc-alkaline/shoshonitic and the 215-225 alkaline magmatic events of the Southern Alps.

8. Rather than a late-stage episode related to the Middle Triassic high-K calc-alkaline/shoshonitic magmatism of the Dolomitic Area, Predazzo lamprophyres should be considered part of the alkaline-carbonatitic magmatic pulse that intruded the subcontinental mantle portion of the Southern Alps at about 215-225 Ma. Such a magmatic event likely represents a precursor of the rifting stage connected to the Alpine Tethys opening, as also suggested by its astenospheric-influenced Sr-Nd isotopic signature. The generation of such H_2O-CO_2-rich alkaline-carbonatitic melts is therefore ascribable to mantle upwelling dynamics in a continental rifting setting (Stähle *et al.*, 1990; 2001; Zaccarini *et al.*, 2004; Batki *et al.*, 2014).
9. Predazzo alkaline lamprophyres can be considered as a geochemical and geochronological marker of the shift from orogenic-like to anorogenic magmatism in the Southern Alps. Their Sr-Nd isotopic signature and incompatible elements pattern suggest that the mantle source that generated the Ladinian (~237 Ma) subduction-related magmas was progressively being depleted, during Late Triassic, by the asthenospheric influx related to the Alpine Tethys opening.

FUNDING

This work was supported by The University Institute for Higher Studies (IUSS) Mobility Research Programme of the University of Ferrara [grant numbers 570, 571] for Long Period, 2016/2017 to [FC] and The Italian National Research Program [PRIN_2015/prot. 20158A9] to [CB].

ACKNOWLEDGEMENTS

NERC are acknowledged for continued funding of the Argon Isotope Facility at SUERC. Alberto Zanetti is acnowledged for LAM-ICP-MS analyses. Anne Kelly, Vincent Gallagher, Ross Dymock and Jim Imlach are thanked for making the Sr and Nd isotopic analyses and the $^{40}Ar/^{39}Ar$ measurements at SUERC.

REFERENCES

Abbas, H., Michail, M., Cifelli, F., Mattei, M., Gianolla, P., Lustrino, M. & Carminati, E. (2018). Emplacement modes of the Ladinian plutonic rocks of the Dolomites: Insights from anisotropy of magnetic susceptibility. *Journal of Structural Geology* **113**, 42-61.

Akinin, V. V., Sobolev, A. V., Ntaflos, T. & Richter, W. (2005). Clinopyroxene megacrysts from Enmelen melanephelinitic volcanoes (Chukchi Peninsula, Russia): application to composition and evolution of mantle melts. *Contributions to Mineralogy and Petrology* **150(1)**, 85-101.

Armienti, P., Corazzato, C., Groppelli, G., Natoli, E. & Pasquarè, G. (2003). Geological and petrographical study of Montecampione Triassic subvolcanic bodies (Southern Alps, Italy): preliminary geodynamic results. *Italian Journal of Geosciences* **2**, 67-78.

Barbieri, G., De Vecchi, G. P., De Zanche, V., Mietto, P. & Sedea, R. (1982). Stratigrafia e petrologia del magmatismo triassico nell'area di Recoaro. Guida alla geologia del Sudalpino centro-orientale. *Società Geologica Italiana - Guide Geologiche Regionali*, 179-187.

Barfod, D. N., Mark, D. F., Tait, A., Dymock, R. C. & Imlach, J. (2014). *Argon extraction from geological samples by CO2 scanning laser step-heating*. In: Jourdan, F., Mark, D.F., & Verati, C. (eds.) *Advances in $^{40}Ar/^{39}Ar$ dating: from archaeology to planetary sciences*. Geological Society of London Special Publication **378**, 79-90.

Barry, T. L., Saunders, A. D., Kempton, P. D., Windley, B. F., Pringle, M. S., Dorjnamjaa, D. & Saandar, S. (2003). Petrogenesis of Cenozoic basalts from Mongolia: evidence for the role of asthenospheric versus metasomatized lithospheric mantle sources. *Journal of Petrology* **44(1)**, 55-91.

Batki, A., Pál-Molnár, E., Dobosi, G. & Skelton, A. (2014). Petrogenetic significance of ocellar camptonite dykes in the Ditrău Alkaline Massif, Romania. *Lithos* **200**, 181-196.

Bébien, J., Blanchet, R., Cadet, J.P., Charvet, J., Chorowicz, J., Lapierre, H. & Rampnoux, J.P. (1978). Le volcanisme Triassique des Dinarides en Yougoslavie: sa place dans l'évolution geotectonique peri-mediterraneenne. *Tectonophysics* **47(1-2)**, 159-176.

Beccaluva, L., Coltorti, M., Saccani, E., Siena, F. & Zeda, O. (2005). *Triassic Magmatism and Jurassic Ophiolites at the Margins of the Adria Plate*. In: Finetti I. R. (ed.) *Crop Project: Deep Seismic Exploration of the Central Mediterranean and Italy*. Elsevier **28**, 607-622.

Bellieni, G., Fioretti, A. M., Marzoli, A. & Visonà, D. (2010). Permo-Paleogene magmatism in the eastern Alps. *Rendiconti Lincei* **21**, S51-S71.

Beltrán-Triviño, A., Winkler, W., von Quadt, A. & Gallhofer, D. (2016). Triassic magmatism on the transition from Variscan to Alpine cycles: evidence from U–Pb, Hf, and geochemistry of detrital minerals. *Swiss Journal of Geosciences* **109(3)**, 309-328.

Bernoulli, D. & Lemoine, M. (1980). Birth and Early Evolution of the Tethys: the Overall Situation. *Mémoires du Bureau de recherches géologiques et minières* **115**, 168-179.

Bianchini, G., Natali, C., Shibata, T. & Yoshikawa, M. (2018). Basic dykes crosscutting the crystalline basement of Valsugana (Italy): new evidence of early Triassic volcanism in the Southern Alps. *Tectonics* **37(7)**, 2080-2093.

Bonadiman, C., Coltorti, M. & Siena, F. (1994). Petrogenesis and *T*-fO_2 estimates of Mt. Monzoni complex (Central Dolomites, Southern Alps): a Triassic shoshonitic intrusion in a trascurrent geodynamic setting. *European Journal of Mineralogy* **6**, 943-966.

Brack, P., Mundil, R., Oberli, F., Meier, M. & Rieber, H. (1996). Biostratigraphic and radiometric age data question the Milankovitch characteristics of the Latemar cycles (Southern Alps, Italy). *Geology* **24(4)**, 371-375.

Buckley, H. A. & Woolley, A. R. (1990). Carbonates of the magnesite-siderite series from four carbonatite complexes. *Mineralogical Magazine* **54(376)**, 413-418.

Carraro, A. & Visonà, D. (2003). Mantle xenoliths in Triassic camptonite dykes of the Predazzo Area (Dolomites, Northern Italy). *European Journal of Mineralogy* **15(1)**, 103-115.

Casetta, F., Coltorti, M., Ickert, R. B., Bonadiman, C., Giacomoni, P. P. & Ntaflos, T. (2018a). Intrusion of shoshonitic magmas at shallow crustal depth: *T–P* path, H_2O estimates, and AFC modeling of the Middle Triassic Predazzo Intrusive Complex (Southern Alps, Italy). *Contributions to Mineralogy and Petrology* **173(7)**, 57.

Casetta, F., Coltorti, M. & Marrocchino, E. (2018b). Petrological evolution of the Middle Triassic Predazzo Intrusive Complex, Italian Alps. *International Geology Review* **60(8)**, 977-997.

Cassinis, G., Cortesogno, L., Gaggero, L., Perotti, C. R. & Buzzi, L. (2008). Permian to Triassic geodynamic and magmatic evolution of the Brescian Prealps (eastern Lombardy, Italy): *Italian Journal of Geosciences* **127(3)**, 501-518.

Castellarin, A., Lucchini, F., Rossi, P. L., Selli, L. & Simboli, G. (1988). The Middle Triassic magmatic-tectonic arc development in the Southern Alps. *Tectonophysics* **146(1-4)**, 79-89.

Coltorti, M. & Siena, F. (1984). Mantle tectonite and fractionate peridotite at Finero (Italian Western Alps). *Neues Jahrbuch fur Mineralogie-Abhandlungen* **149(3)**, 225-244.

Dal Piaz, G., Bistacchi, A. & Massironi, M. (2003). Geological outline of the Alps. *Episodes* **26(3)**, 175-180.

Dallmeyer, D.R., Kräutner, H.G. & Neubauer, F. (1997). Middle-late Triassic $^{40}Ar/^{39}Ar$ hornblende ages for early intrusions within the Ditrau alkaline massif, Rumania: Implications for Alpine rifting in the Carpathian orogen. *Geologica Carpathica* **48(6)**, 347-352.

Doglioni, C. (1984). Triassic diapiric structure in the central Dolomites (Northen Italy). *Eclogae Geologicae Helvetiae* **77**, 2.

Doglioni, C. (1987). Tectonics of the Dolomites (Southern Alps, Northern Italy). *Journal of Structural Geology* **9**, 181-193.

Doglioni, C. (2007). Tectonics of the Dolomites. *Bulletin für angewandte Geologie* **12(2)**, 11-15.

Doglioni, C., & Carminati, E. (2008). Structural styles and Dolomites field trip. *Memorie Descrittive della Carta Geologica d'Italia* **82**, 301.

Ellis, B. S., Mark, D. F., Pritchard, C. J. & Wolff, J. A. (2012). Temporal dissection of the Huckleberry Ridge Tuff using the $^{40}Ar/^{39}Ar$ dating technique. *Quaternary Geochronology* **9**, 34-41.

Falloon, T. J. & Green, D. H. (1988). Anhydrous partial melting of peridotite from 8 to 35 kb and the petrogenesis of MORB. *Journal of Petrology* **1**, 379-414.

Ferrario, A. & Garuti, G. (1990). Platinum-group mineral inclusions in chromitites of the Finero mafic-ultramafic complex (Ivrea-Zone, Italy). *Mineralogy and Petrology* **41(2-4)**, 125-143.

Frost, D.J. (2006). The stability of hydrous mantle phases. *Reviews in Mineralogy and Geochemistry* **62(1)**, 243-271.

Fujimaki, H., Tatsumoto, M. & Aoki, K. I. (1984). Partition coefficients of Hf, Zr, and REE between phenocrysts and groundmasses. *Journal of Geophysical Research: Solid Earth* **89(S02)**, B662-B672.

Fumagalli, P., Zanchetta, S. & Poli, S. (2009). Alkali in phlogopite and amphibole and their effects on phase relations in metasomatized peridotites: a high-pressure study. *Contributions to Mineralogy and Petrology* **158(6)**, 723.

Galassi, B., Monese, A., Ogniben, G., Siena, F. & Vaccaro, C. (1994). Age and nature of lamprophyric dykes at Calceranica (Trento). *Mineralogica et Petrographica Acta* **37**, 163-171.

Gasparotto, G. & Simboli, G. (1991). Mineralogia, petrografia e schemi evolutivi delle magmatiti triassiche del complesso di Cima Pape (Dolomiti Orientali). *Mineralogica et Petrografica Acta* **34**, 205-234.

Giacomoni, P. P., Coltorti, M., Bryce, J. G., Fahnestock, M. F. & Guitreau, M. (2016). Mt. Etna plumbing system revealed by combined textural, compositional, and thermobarometric studies in clinopyroxenes. *Contributions to Mineralogy and Petrology* **171(4)**, 34.

Giacomoni, P. P., Ferlito, C., Coltorti, M., Bonadiman, C. & Lanzafame, G. (2014). Plagioclase as archive of magma ascent dynamics on "open conduit" volcanoes: The 2001-2006 eruptive period at Mt. Etna. *Earth-Science Reviews* **138**, 371-393.

Gianolla, P. (1992). Evoluzione mediotriassica del vulcanismo di Rio Freddo (Api Giulie, Italia). *Memorie di Scienze Geologiche* **44**, 193-209.

Gozzi, F., Gaeta, M., Freda, C., Mollo, S., Di Rocco, T., Marra, F., ... & Pack, A. (2014). Primary magmatic calcite reveals origin from crustal carbonate. *Lithos* **190**, 191-203.

Hammouda, T., & Keshav, S. (2015). Melting in the mantle in the presence of carbon: Review of experiments and discussion on the origin of carbonatites. *Chemical Geology* **418**, 171-188.

Hawthorne, F. C., Oberti, R., Harlow, G. E., Maresch, W. V., Martin, R. F., Schumacher, J. C. & Welch, M.D. (2012). Nomenclature of the amphibole supergroup. *American Mineralogist* **97(11-12)**, 2031-2048.

Hay, R. L. & O'Neil, J. R. (1983). Carbonatite tuffs in the Laetolil Beds of Tanzania and the Kaiserstuhl in Germany. *Contributions to Mineralogy and Petrology* **82(4)**, 403-406.

Hogarth, D. D. (1989). *Pyrochlore, apatite and amphibole: distinctive minerals in carbonatite*. In: Bell, K. (ed.) *Carbonatites: Genesis and Evolution*. Unwin Hyman, London, 103-148.

Ickert, R. B. (2013). Algorithms for estimating uncertainties in initial radiogenic isotope ratios and model ages. *Chemical Geology* **340**, 131-138.

Ishibashi H. (2013). Spinel-melt oxygen barometry: a method and application to Cenozoic alkali basaltic magmas from the Higashi-Matsuura district, NW Kyushu. *Japan Geoscience Reports* **40**, 21-32.

Kinzler, R. J. & Grove, T. L. (1992). Primary magmas of mid-ocean ridge basalts 1. Experiments and methods. *Journal of Geophysical Research: Solid Earth* **97(B5)**, 6885-6906.

Kress, V. C. & Carmichael, I. S. (1991). The compressibility of silicate liquids containing Fe_2O_3 and the effect of composition, temperature, oxygen fugacity and pressure on their redox states. *Contributions to Mineralogy and Petrology* **108(1-2)**, 82-92.

Langone, A., Zanetti, A., Daczko, N. R., Piazolo, S., Tiepolo, M. & Mazzucchelli, M. (2018). Zircon U-Pb Dating of a Lower Crustal Shear Zone: A Case Study From the Northern Sector of the Ivrea-Verbano Zone (Val Cannobina, Italy). *Tectonics* **37(1)**, 322-342.

Leake, B. E., Woolley, A. R., Arps, C. E. S., Birch, W. D., Gilbert, M. C., Grice, J. D., … & Linthout, K. (1997). Nomenclature of amphiboles: report of the subcommittee on amphiboles of the International Mineralogical Association Commission on New Minerals and Mineral Names. *Mineralogical Magazine* **61**, 295-321.

Leat, P. T., Riley, T. R., Storey, B. C., Kelley, S. P. & Millar, I. L. (2000). Middle Jurassic ultramafic lamprophyre dyke within the Ferrar magmatic province, Pensacola Mountains, Antarctica. *Mineralogical Magazine* **64(1)**, 95-111.

Lee, J-Y., Marti, K., Severinghaus, J. P., Kawamura, K., Yoo, H. S., Lee, J. B., & Kim, J. S. (2006). A redetermination of the isotopic abundances of atmospheric Ar. *Geochimica et Cosmochimica Acta* **70**, 4507-4512.

Le Maitre, R.W., Bateman, P., Dudek, A., Keller, J., Lameyre, L., Sabine, P. A., ... and Zanettin, B., 1989. A classification of igneous rocks and glossary of terms: recommendations of the IUGS Commission on the Systematics of Igneous Rocks.

Le Maitre, R. W., Streckeisen, A., Zanettin, B., Le Bas, M. J., Bonin, B., Bateman, P., … & Lameyre, J. (2002). *Igneous rocks. A classification and glossary of terms. Recommendations of the IUGS Subcomission on the Systematics of Igneous Rocks.* Cambridge University Press.

Le Roex, A. P. & Lanyon, R. (1998). Isotope and trace element geochemistry of Cretaceous Damaraland lamprophyres and carbonatites, northwestern Namibia: Evidence for plume-lithosphere interactions. *Journal of Petrology* **39(6)**, 1117-1146.

Lippolt, H. & Pidgeon, R. (1974). Isotopic mineral ages of a diorite from the Eisenkappel intrusion, Austria. *Zeitschrift für Naturforschung* **29a**.

Locock, A. J. (2014). An Excel spreadsheet to classify chemical analyses of amphiboles following the IMA 2012 recommendations. *Computers & Geosciences* **62**, 1-11.

Lu, Y. J., McCuaig, T. C., Li, Z. X., Jourdan, F., Hart, C. J., Hou, Z. Q. & Tang, S.H. (2015). Paleogene post-collisional lamprophyres in western Yunnan, western Yangtze Craton: mantle source and tectonic implications. *Lithos* **233**, 139-161.

Lucchini, F., Mezzetti, R. & Simboli, G. (1969). The lamprophyres of the area Predazzo-Monzoni: camptonites. *Mineralogica et Petrografica Acta* **15**, 109-145.

Lucchini, F., Rossi, P. L. & Simboli, G. (1982). *Il magmatismo triassico dell'area di Predazzo (Alpi Meridionali, Italia)*. In: Castellarin, A. & Vai, G. B. (eds.). *Guida alla Geologia del Sudalpino centro-orientale*. Guide Geologiche Regionali Società Geologica Italiana, 221-230.

Lugmair, G. W. & Marti, K. (1978). Lunar initial $^{143}Nd/^{144}Nd$: differential evolution of Lunar crust and mantle. *Earth and Planetary Science Letters* **39**, 349-357.

Malitch, K. N., Belousova, E. A., Griffin, W. L., Badanina, I. Y., Knauf, V. V., O'Reilly, S. Y. & Pearson, N.J. (2017). Laurite and zircon from the Finero chromitites (Italy): New insights into evolution of the subcontinental mantle. *Ore Geology Reviews* **90**, 210-225.

Mandler, B. E. & Grove, T. L. (2016). Controls on the stability and composition of amphibole in the Earth's mantle. *Contributions to Mineralogy and Petrology* **171(8-9)**, 68.

Mark, D. F., Rice, C. M., Lee, M. R., Fallick, A. E., Boyce, A., Trewin, N. H. & Lee, J. K. W. (2011a). $^{40}Ar/^{39}Ar$ dating of hydrothermal activity, biota and gold mineralization in the Rhynie hot-spring system, Aberdeenshire, Scotland. *Geochimica et Cosmochimica Acta* **75**, 555-569.

Mark, D. F., Stuart, F. M. & De Podesta, M. (2011b). New high-precision measurements of the isotopic composition of atmospheric argon. *Geochimica et Cosmochimica Acta* **75(23)**, 7494-7501.

Marrocchino, E., Coltorti, M., Visonà, D. & Thirwall, M. F. (2002). Petrology of Predazzo magmatic complex (Trento, Italy). *Geochimica et Cosmochimica Acta* **66(15a)**, A486-A486.

Matsumoto, T., Morishita, T., Matsuda, J. I., Fujioka, T., Takebe, M., Yamamoto, K. & Arai, S. (2005). Noble gases in the Finero phlogopite-peridotites, western Italian Alps. *Earth and Planetary Science Letters* **238(1-2)**, 130-145.

Mazzucchelli, M., Rivalenti, G., Brunelli, D., Zanetti, A. & Boari, E. (2009). Formation of highly refractory dunite by focused percolation of pyroxenite-derived melt in the Balmuccia peridotite massif (Italy). *Journal of Petrology* **50(7)**, 1205-1233.

McKenzie, D. A. N. & O'nions, R. K. (1991). Partial melt distributions from inversion of rare earth element concentrations. *Journal of Petrology* **32(5)**, 1021-1091.

Meschede, M. (1986). A method of discriminating between different types of mid-ocean ridge basalts and continental tholeiites with the Nb-Zr-Y diagram. *Chemical geology* **56(3-4)**, 207-218.

Mietto, P., Manfrin, S., Preto, N., Rigo, M., Roghi, G., Furin, S., Gianolla, P., Posenato, R., ... & Bowring, S.A. (2012). The Global Boundary Stratotype Section and Point (GSSP) of the Carnian Stage (Late Triassic) at Prati di Stuores/ Stuores Wiesen Section (Southern Alps, NE Italy). *Episodes* **35(3)**, 414-430.

Moore, J. M., Kuhn, B. K., Mark, D. F. & Tsikos, H. (2011). A sugilite-bearing assemblage from the Wolhaarkop breccia, Bruce iron-ore mine, South Africa: Evidence for alkali metasomatism and ^{40}Ar-^{39}Ar dating. *European Journal of Mineralogy* **23(4)**, 661-673.

Morgan, L. E., Mark, D. F., Imlach, J., Barfod, D. & Dymock, R. (2014). FCs-EK: a new sampling of the Fish Canyon Tuff $^{40}Ar/^{39}Ar$ neutron flux monitor. *Geological Society of London, Special Publications* **378(1)**, 63-67.

Morimoto, N. (1988). Nomenclature of pyroxenes. *Mineralogy and Petrology* **39(1)**, 55-76.

Morishita, T., Arai, S. & Tamura, A. (2003). Petrology of an apatite-rich layer in the Finero phlogopite–peridotite, Italian Western Alps; implications for evolution of a metasomatising agent. *Lithos* **69(1-2)**, 37-49.

Morishita, T., Hattori, K. H., Terada, K., Matsumoto, T., Yamamoto, K., Takebe, M., ... & Arai, S. (2008). Geochemistry of apatite-rich layers in the Finero phlogopite–peridotite massif (Italian Western Alps) and ion microprobe dating of apatite. *Chemical Geology* **251(1-4)**, 99-111.

Morogan, V., Upton, B. G. J., & Fitton, J. G. (2000). The petrology of the Ditrau alkaline complex, Eastern Carpathians. *Mineralogy and Petrology* **69(3-4)**, 227-265.

Morten, L. (1980). Mineral chemistry of ultramafic inclusions from the Predazzo volcanic rocks. Dolomite Region, north Italy. *Journal of Mineralogy and Geochemistry* **138**, 259-273.

Mukasa, S.B. & Shervais, J. W. (1999). Growth of subcontinental lithosphere: evidence from repeated dike injections in the Balmuccia lherzolite massif, Italian Alps. *Lithos* **48**, 287-316.

Mundil, R., Brack, P. & Laurenzi, M. A. (1996). High resolution U/Pb single zircon age determinations: new constraints on the timing of Middle Triassic magmatism in the Southern Alps. *Conference abstract, 78° Riunione estiva S.G.I.*

Oberti, R., Cannillo, E. & Toscani, G. (2012). How to name amphiboles after the IMA2012 report: rules of thumb and a new PC program for monoclinic amphiboles. *Periodico di Mineralogia* **81(2)**, 257-267.

Pál-Molnár, E., Batki, A., Almási, E., Kiss, B., Upton, B. G., Markl, G., ... & Harangi, S. (2015). Origin of mafic and ultramafic cumulates from the Ditrău Alkaline Massif, Romania. *Lithos* **239**, 1-18.

Pamic, J. J. (1984). Triassic magmatism of the Dinarides in Yugoslavia. *Tectonophysics* **109(3-4)**, 273-307.

Pană, D., Balintoni, I. & Heaman, L. (2000). Precise U-Pb zircon dating of the syenite phase from the Ditrau alkaline igneous complex. *Studia UBB Geologia* **45(1)**, 79-90.

Pandey, A., Rao, N. C., Chakrabarti, R., Pandit, D., Pankaj, P., Kumar, A. & Sahoo, S. (2017a). Petrogenesis of a Mesoproterozoic shoshonitic lamprophyre dyke from the Wajrakarur kimberlite field, eastern Dharwar craton, southern India: geochemical and Sr-Nd isotopic evidence for a modified sub-continental lithospheric mantle source. *Lithos* **292**, 218-233.

Pandey, A., Rao, N. C., Pandit, D., Pankaj, P., Pandey, R., Sahoo, S. & Kumar, A. (2017b). Subduction–tectonics in the evolution of the eastern Dharwar craton, southern India: Insights from the post-collisional calc-alkaline lamprophyres at the western margin of the Cuddapah basin. *Precambrian Research* **298**, 235-251.

Pearce, J. A. (1982). Trace element characteristics of lavas from destructive plate boundaries. *Andesites* **8**, 525-548.

Pearce, J. A. & Norry, M. J. (1979). Petrogenetic implications of Ti, Zr, Y, and Nb variations in volcanic rocks. *Contributions to Mineralogy and Petrology* **69(1)**, 33-47.

Pe-Piper, G. (1982). Geochemistry, tectonic setting and metamorphism of mid-Triassic volcanic rocks of Greece. *Tectonophysics* **85(3-4)**, 253-272.

Pe-Piper, G. (1983). Triassic shoshonites and andesites, Lakmon Mountains, western continental Greece: Differences in primary geochemistry and sheet silicate alteration products. *Lithos* **16(1)**, 23-33.

Pe-Piper, G. (1998). The nature of Triassic extension-related magmatism in Greece: evidence from Nd and Pb isotope geochemistry. *Geological Magazine* **135(3)**, 331-348.

Petrone, C. M., Braschi, E., Francalanci, L., Casalini, M. & Tommasini, S. (2018). Rapid mixing and short storage timescale in the magma dynamics of a steady-state volcano. *Earth and Planetary Science Letters* **492**, 206-221.

Pilet, S., Ulmer, P. & Villiger, S. (2010). Liquid line of descent of a basanitic liquid at 1.5 GPa: constraints on the formation of metasomatic veins. *Contributions to Mineralogy and Petrology* **159(5)**, 621-643.

Pinzuti, P., Humler, E., Manighetti, I. & Gaudemer, Y. (2013). Petrological constraints on melt generation beneath the Asal Rift (Djibouti) using quaternary basalts. *Geochemistry, Geophysics, Geosystems* **14(8)**, 2932-2953.

Pouchou, J. L. & Pichoir, F. (1991). *Quantitative analysis of homogeneous or stratified microvolumes applying the model "PAP"*. In: *Electron probe quantitation*. Springer US, 31-75.

Putirka, K. D., Johnson, M., Kinzler, R., Longhi, J. & Walker, D. (1996). Thermobarometry of mafic igneous rocks based on clinopyroxene-liquid equilibria, 0–30 kbar. *Contributions to Mineralogy and Petrology* **123(1)**, 92-108.

Putirka, K. D. (2008). Thermometers and barometers for volcanic systems. *Reviews in Mineralogy and Geochemistry* **69(1)**, 61-120.

Putirka, K. D. (2016). Amphibole thermometers and barometers for igneous systems and some implications for eruption mechanisms of felsic magmas at arc volcanoes. *American Mineralogist* **101(4)**, 841-858.

Raffone, N., Le Fèvre, B., Ottolini, L., Vannucci, R. & Zanetti, A. (2006). Light-lithophile element metasomatism of Finero peridotite (W Alps): a secondary-ion mass spectrometry study. *Microchimica Acta* **155(1-2)**, 251-255.

Renne, P. R., Deino, A. L., Hames, W. E., Heizler, M. T., Hemming, S. R., Hodges, K. V., Koppers, A. A. P., Mark, D. F., … & Wijbrans, J.R. (2009). Data Reporting Norms for $^{40}Ar/^{39}Ar$ Geochronology. *Quaternary Geochronology* **4**, 346-352.

Renne, P. R., Mundil, R., Balco, G., Min, K. & Ludwig, K. R. (2010). Joint determination of ^{40}K decay constants and $^{40}Ar^*/^{40}K$ for the Fish Canyon sanidine standard, and improved accuracy for $^{40}Ar/^{39}Ar$ geochronology. *Geochimica et Cosmochimica Acta* **74**, 5349-5367.

Renne, P. R., Balco, G., Ludwig, K. R., Mundil, R. & Min, K. (2011). Response to comment by W.H. Schwarz *et al.* on 'Joint determination of ^{40}K decay constants and $^{40}Ar^*/^{40}K$ for the Fish Canyon sanidine standard, and improved accuracy for $^{40}Ar/^{39}Ar$ geochronology' by P.R. Renne *et al.*, 2010. *Geochimica et Cosmochimica Acta* **75**, 5097-5100.

Ridolfi, F., Renzulli, A. & Puerini, M. (2010). Stability and chemical equilibrium of amphibole in calc-alkaline magmas: an overview, new thermobarometric formulations and application to subduction-related volcanoes. *Contributions to Mineralogy and Petrology* **160(1)**, 45-66.

Ridolfi, F., Zanetti, A., Renzulli, A., Perugini, D., Holtz, F. & Oberti, R. (2018). AMFORM, a new mass-based model for the calculation of the unit formula of amphiboles from electron microprobe analyses. *American Mineralogist* **103**, 1112-1125.

Robinson, J. A. C. & Wood, B. J. (1998). The depth of the spinel to garnet transition at the peridotite solidus. *Earth and Planetary Science Letters* **164(1-2)**, 277-284.

Rock, N. M. S. (1987). The nature and origin of lamprophyres: an overview. *Geological Society of London, Special Publications* **30(1)**, 191-226.

Rock, N. M. S. (1991). *Lamprophyres*. Springer.

Rotenberg, E., Davis, D. W., Amelin, Y., Ghosh, S. & Bergquist, B. A. (2012). Determination of the decay-constant of ^{87}Rb by laboratory accumulation of ^{87}Sr. *Geochimica et Cosmochimica Acta* **85**, 41-57.

Ruiz-Agudo, E., Putnis, C. V. & Putnis, A. (2014). Coupled dissolution and precipitation at mineral–fluid interfaces. *Chemical Geology* **383**, 132-146.

Saccani, E. (2015). A new method of discriminating different types of post-Archean ophiolitic basalts and their tectonic significance using Th-Nb and Ce-Dy-Yb systematics. *Geoscience Frontiers* **6(4)**, 481-501.

Scarrow, J. H., Molina, J. F., Bea, F., Montero, P. & Vaughan, A. P. (2011). Lamprophyre dikes as tectonic markers of late orogenic transtension timing and kinematics: A case study from the Central Iberian Zone. *Tectonics*, **30(4)**.

Schmid, M. S., Bernoulli, D., Fügenschuh, B., Georgiev, N., Kounov, A., Matenco, L., Oberhansli, R., Pleuger, J., Schefer, S., Ustaszewski, K. & Van Hinsbergen, D. (2016). Tectonic units of the Alpine collision zone between Eastern Alps and Western Turkey: *Unpublished map*.

Schmid, S. M., Bernoulli, D., Fügenschuh, B., Matenco, L., Schefer, S., Schuster, R., Tischler, M. & Ustaszewski, K. (2008). The Alpine-Carpathian-Dinaridic orogenic system: correlation and evolution of tectonic units. *Swiss Journal of Geosciences* **101(1)**, 139-183.

Schmidt, K. H., Bottazzi, P., Vannucci, R. & Mengel, K. (1999). Trace element partitioning between phlogopite, clinopyroxene and leucite lamproite melt. *Earth and Planetary Science Letters* **168(3)**, 287-299.

Seghedi, I., Downes, H., Vaselli, O., Szakács, A., Balogh, K. & Pécskay, Z. (2004). Post-collisional Tertiary-Quaternary mafic alkalicmagmatism in the Carpathian–Pannonian region: a review. *Tectonophysics* **393**, 43–62.

Shaw, D. M. (1970). Trace element fractionation during anatexis. *Geochimica et Cosmochimica Acta* **34(2)**, 237-243.

Sloman, L. E. (1989). Triassic shoshonites from the dolomites, northern Italy: Alkaline arc rocks in a strike-slip setting. *Journal of Geophysical Research: Solid Earth* **94(B4)**, 4655-4666.

Smith, E. I., Sanchez, A., Walker, J. D. & Wang, K. (1999). Geochemistry of mafic magmas in the Hurricane Volcanic field, Utah: implications for small-and large-scale chemical variability of the lithospheric mantle. *The Journal of Geology* **107(4)**, 433-448.

Soder, C. & Romer, R. L. (2018). Post-collisional potassic–ultrapotassic magmatism of the Variscan Orogen: implications for mantle metasomatism during continental subduction. *Journal of Petrology* **59(6)**, 1007-1034.

Stahle, V., Frenzel, G., Hess, J. C., Saupé, F., Schmidt, S. T. & Schneider, W. (2001). Permian metabasalt and Triassic alkaline dykes in the northern Ivrea zone: clues to the post-Variscan geodynamic evolution of the Southern Alps. *Schweizerische Mineralogische und Petrographische Mitteilungen* **81(1)**, 1-21.

Stähle, V., Frenzel, G., Kober, B., Michard, A., Puchelt, H. & Schneider, W. (1990). Zircon syenite pegmatites in the Finero peridotite (Ivrea zone): evidence for a syenite from a mantle source. *Earth and Planetary Science Letters* **101(2-4)**, 196-205.

Stampfli, G.M. (2005). *Plate Tectonics of the Apulia-Adria Microcontinents*. In: Finetti, I. R. (ed.) *Crop Project: Deep Seismic Exploration of the Central Mediterranean and Italy*. Elsevier **28**, 747-766.

Stampfli, G. M. & Borel, G. D. (2002). A plate tectonic model for the Paleozoic and Mesozoic constrained by dynamic plate boundaries and restored synthetic oceanic isochrones. *Earth and Planetary Science Letters* **196(1)**, 17-33.

Stampfli, G. M. & Borel, G. D. (2004). *The TRANSMED transects in space and time: constraints on the paleotectonic evolution of the Mediterranean domain*. In: The TRANSMED Atlas: The Mediterranean region from crust to mantle, 53-80.

Stampfli, G. M., Borel, G. D., Marchant, R. & Mosar, J. (2002). Western Alps geological constraints on western Tethyan reconstructions. *Journal of the Virtual Explorer* **8**, 77.

Stoppa, F. (2008). *Alkaline and ultramafic lamprophyres in Italy: Distribution, mineral phases, and bulk rock data. Deep-Seated Magmatism, Its Sources and Plumes*. Publishing House of the Institute of Geography, SB RAS, 209-238.

Stoppa, F., Rukhlov, A.S., Bell, K., Schiazza, M. & Vichi, G. (2014). Lamprophyres of Italy: early cretaceous alkaline lamprophyres of southern Tuscany, Italy. *Lithos* **188**, 97-112.

Storck, J-C., Brack, P., Wotzlaw, J-F & Ulmer, P. (2018). Timing and evolution of Middle Triassic magmatism in the Southern Alps (Northern Italy). *Journal of the Geological Society* **123**.

Sun, S. & McDonough, W. F. (1989). *Chemical and isotopic systematics of oceanic basalts: implication for mantle and processes*. In: Saunders A. D. & Norry M. J. (eds.) *Magmatism in the Ocean Basins*. Geological Society, Special Publications, **42**, 313-345.

Takahashi, E. & Kushiro, I. (1983). Melting of a dry peridotite at high pressures and basalt magma genesis. *American Mineralogist* **68(9-10)**, 859-879.

Tiepolo, M., Bottazzi, P., Palenzona, M. & Vannucci, R. (2003). A laser probe coupled with ICP–double-focusing sector-field mass spectrometer for in situ analysis of geological samples and U-Pb dating of zircon. *The Canadian Mineralogist* **41(2)**, 259-272.

Tindle, A. G. & Webb, P. C. (1994). PROBE-AMPH - a spreadsheet program to classify microprobe-derived amphibole analyses. *Computer and Geosciences* **20**, 1201-1228.

Traill, R. J. & Lachance, G. R. (1966). A practical solution to the matrix problem in X-ray analysis. II. Application to a multicomponent alloy system. Canadian Spectroscopy **11(3)**, 63-71.

Tumiati, S., Fumagalli, P., Tiraboschi, C. & Poli, S. (2013). An experimental study on COH-bearing peridotite up to 3.2 GPa and implications for crust–mantle recycling. *Journal of Petrology* **54(3)**, 453-479.

Ubide, T., Galé, C., Arranz, E., Lago, M. & Larrea, P. (2014). Clinopyroxene and amphibole crystal populations in a lamprophyre sill from the Catalonian Coastal Ranges (NE Spain): a record of magma history and a window to mineral-melt partitioning. *Lithos* **184**, 225-242.

Vardabasso, S. (1929). Rapporti tra attività magmatica e vicende tettoniche nella provincia petrografica di Predazzo. *Studi Trentini di Scienze Naturali* **11**.

Vichi, G., Stoppa, F. & Wall, F. (2005). The carbonate fraction in carbonatitic Italian lamprophyres. *Lithos* **85(1-4)**, 154-170.

Visonà, D. & Zanferrari, A (2000). Some constraints on geochemical features in the Triassic mantle of the easternmost Austroalpine-Southalpine domain: evidence from the Karawanken pluton (Carinthia, Austria). *International Journal of Earth Sciences* **89(1)**, 40-51.

Voshage, H., Hunziker, J. C., Hofmann, A. W. & Zingg, A. (1987). A Nd and Sr isotopic study of the Ivrea zone, Southern Alps, N-Italy. *Contributions to Mineralogy and Petrology* **97**, 31-42.

Wood, D.A. (1980). The application of a Th-Hf-Ta diagram to problems of tectonomagmatic classification and to establishing the nature of crustal contamination of basaltic lavas of the British Tertiary Volcanic Province. *Earth and Planetary Science Letters* **50(1)**, 11-30.

Woolley, A. R., Bergman, S. C., Edgar, A. D., Le Bas, M. J., Mitchell, R. H., Rock, N. M. S. & Scott Smith, B. H. (1996). Classification of lamprophyres, lamproites, kimberlites, and the kalsilitic, melilitic, and leucitic rocks. *The Canadian Mineralogist* **34(2)**, 175-186.

Workman, R. K. & Hart, S. R. (2005). Major and trace element composition of the depleted MORB mantle (DMM). *Earth and Planetary Science Letters* **231(1)**, 53-72.

Wotzlaw, J. F., Brack, P. & Storck, J. C. (2018). High-resolution stratigraphy and zircon U–Pb geochronology of the Middle Triassic Buchenstein Formation (Dolomites, northern Italy):

precession-forcing of hemipelagic carbonate sedimentation and calibration of the Anisian-Ladinian boundary interval. *Journal of the Geological Society* **175(1)**, 71-85.

Zaccarini, F., Stumpfl, E. F. & Garuti, G. (2004). Zirconolite and Zr–Th–U minerals in chromitites of the Finero complex, Western Alps, Italy: evidence for carbonatite-type metasomatism in a subcontinental mantle plume. *The Canadian Mineralogist* **42(6)**, 1825-1845.

Zack, T. & Brumm, R. (1998). *Ilmenite/liquid partition coefficients of 26 trace elements determined through ilmenite/clinopyroxene partitioning in garnet pyroxene*. In: Gurney, J. J., Gurney, J. L., Pascoe, M. D. & Richardson, S. H. (eds.) *7th International Kimberlite Conference*. Red Roof Design, Cape Town, 986-988.

Zaitsev, A. N., Sitnikova, M. A., Subbotin, V. V., Fernández-Suárez, J., Jeffries, T. E. & Wall, F. (2004). Sallanlatvi complex: a rare example of magnesite and siderite carbonatites. Phoscorites and carbonatites from mantle to mine: the key example of the Kola Alkaline Province. *Mineralogical Society of London*, 201-245.

Zanetti, A., Giovanardi, T., Langone, A., Tiepolo, M., Wu, F. Y., Dallai, L. & Mazzucchelli, M. (2016). Origin and age of zircon-bearing chromitite layers from the Finero phlogopite peridotite (Ivrea-Verbano Zone, Western Alps) and geodynamic consequences. *Lithos* **262**, 58-74.

Zanetti, A., Mazzucchelli, M., Rivalenti, G. & Vannucci, R. (1999). The Finero phlogopite-peridotite massif: an example of subduction-related metasomatism. *Contributions to Mineralogy and Petrology* **134(2-3)**, 107-122.

Zanetti, A., Mazzucchelli, M., Sinigoi, S., Giovanardi, T., Peressini, G. & Fanning, M. (2013). SHRIMP U–Pb Zircon Triassic intrusion age of the Finero mafic complex (Ivrea–Verbano zone, Western Alps) and its geodynamic implications. *Journal of Petrology* **54(11)**, 2235-2265.

Ziegler, P. A. & Stampfli, G. M. (2001). Late Palaeozoic-Early Mesozoic plate boundary reorganization: collapse of the Variscan orogen and opening of Neotethys. *Natura Bresciana* **25**, 17-34.

Zindler, A. & Hart, S. R. (1986). Chemical geodynamics. *Annual Review of Earth and Planetary Sciences* **14**, 493-571.

FIGURE CAPTIONS

Fig. 1. (colour online)

(**a**) Map of the tectonic units of the eastern portion of the Alps (partly modified from Castellarin *et al.*, 1988; Dal Piaz *et al.*, 2003; Schmid *et al.*, 2016). LO: Ligurian Ophiolites; AM: deformed Adriatic margin; AD: Adriatic Microplate; SA: Southern Alps; DI: Dinarides; SM: Southern margin of Meliata; HB: Eoalpine High-Pressure Belt; TW: Tauern tectonic Window; EW: Engadine tectonic Window; OTW: Ossola-Tessin tectonic Window; EA: Eastern Austroalpine; H: Helvetic domain; M: Molasse foredeep. The Middle Triassic magmatic occurrences in the Southern Alps domain are evidenced in black. They are, from west to east: Brescian Alps, Alto Vicentino, Valsugana, Dolomitic Area, Carnia and Karawanken. (**b**) Simplified geological map of the Predazzo Intrusive Complex (PIC), showing the occurrence of lamprophyric dykes (modified from Casetta *et al.*, 2018*a*).

Fig. 2. (colour online)

(**a**) Lamprophyric dyke intruded in the Granitic Unit (GU) syenogranite at Predazzo. (**b**) Amphibole megacrysts (indicated by the arrow) and (**c**) clinopyroxenitic xenolith included in the lamprophyric rocks. On the right, photomicrographs in transmitted plane-polarized light of (**d**) a camptonitic and (**e**) bostonitic lamprophyre (sample MA1).

Fig. 3. (colour online)

Total Alkali vs. Silica (TAS) diagram (Le Maitre *et al.*, 2002) and K_2O vs. Na_2O diagram (insert up on the left) showing the composition of Predazzo camptonitic and bostonitic lamprophyres. Fields indicate the composition of the Shoshonitic Silica Saturated (SS), Shoshonitic Silica Undersaturated (SU) and Granitic Unit (GU) of the Predazzo Intrusive Complex (from Casetta *et al.*, 2018*a*; 2018*b*).

Fig. 4. (colour online)

(**a**) Co, (**b**) Cr, (**c**) Ni and (**d**) Zr vs. MgO variation diagrams for Predazzo lamprophyres.

Fig. 5. (colour online)

Chondrite-normalized (Sun & McDonough, 1989) trace element (**a**) and REE patterns (**b**) of Predazzo camptonitic and bostonitic dykes. The OIB pattern (Sun & McDonough, 1989), the average composition of the worldwide camptonites (Rock, 1991), Italian lamprophyres (Galassi *et al.*, 1994; Vichi *et al.*, 2005; Stoppa *et al.*, 2008; 2014), Ditrau lamprophyres (Batki *et al.*, 2014) and Predazzo Intrusive Complex Shoshonitic Silica Saturated (SS) and Undersaturated (SU) rocks (Casetta *et al.*, 2018a; 2018*b*) are reported for comparison.

Fig. 6. (colour online)

Mineral phase classification diagrams showing the composition of the main crystals of Predazzo camptonites and bostonite. (**a**) Orthoclase-Albite-Anorthite ternary diagram for plagioclase and K-Feldspar; (**b**) Rutile-Wustite-Hematite ternary diagram for Fe-Ti oxide; (**c**) Wollastonite-Enstatite-Ferrosilite diagram for clinopyroxene. (**d**) TiO_2 and (**e**) Na_2O vs. Mg# diagrams for amphibole crystals, discriminating between the five textural types (see text).

Fig. 7. (colour online)

Photomicrographs in transmitted plane-polarized light, back scattered SEM images and core-to-rim compositional (Mg# and TiO_2) profiles of (**a**) *Type 1*, (**b**) *Type 2*, (**c**) *Type 3*, (**d**) *Type 4* and (**e**) *Type 5* amphiboles recognized in Predazzo camptonites and bostonite. For each amphibole type, the determination of the water content (H_2O wt%) dissolved in the melt obtained by the equation of Ridolfi *et al.* (2010) and the crystallization temperature (*T* °C) calculated by means of Putirka (2016) thermometer are also reported.

Fig. 8. (colour online)

Chondrite-normalized (Sun & McDonough, 1989) trace element (**a, c**) and REE (**b, d**) patterns of amphibole (Amph) and clinopyroxene (Cpx) crystals. Solid lines: core composition; dotted lines: rim composition.

Fig. 9. (colour online)

Compositional and textural features of the carbonate ocelli inside Predazzo lamprophyres. (**a**) Calcite-magnesite-siderite ternary diagram and (**b**) SrO+MnO vs. CaO/MgO diagram (after Vichi *et al.*, 2005) showing the composition of carbonates from the inner and outer portions of the ocelli. (**c, d, e**) Back scattered SEM images of carbonate ocelli composed of (**c, d**) both dolomite-ankerite/magnesite-siderite or (**e**) dolomite-ankerite crystals only. The flow-aligned tangential growth of amphibole, plagioclase and clinopyroxene is particularly evident in (**d**) and (**e**).

Fig. 10. (colour online)

$^{40}Ar/^{39}Ar$ Age spectra for mineral separates from Predazzo camptonites, with apparent ages and K/Ca ratios spectra plotted against the cumulative percentage of ^{39}Ar released. (**a**) Age spectrum yielded by amphibole crystals from sample FF37; (**b**) age spectrum yielded by plagioclase crystals from sample FF2. Plateau ages are indicated in bold.

Fig. 11. (colour online)

$^{87}Sr/^{86}Sr$ vs. $^{143}Nd/^{144}Nd$ diagram showing the isotopic signature of Predazzo lamprophyres corrected to 220 Ma. Fields indicate the Sr-Nd isotopic signature of the: Finero (Voshage *et al.*, 1987), Balmuccia and Baldissero peridotites (Mukasa & Shervais 1999; Mazzucchelli *et al.*, 2009); alkaline dykes intruded in the Finero peridotite (220 Ma; Stahle *et al.*, 2001); apatite-rich layers of the Finero peridotite (215 Ma; Morishita *et al.*, 2008); Ditrau lamprophyres (220 Ma; Batki *et al.*, 2014); Predazzo Intrusive Complex (PIC) Shoshonitic Silica Saturated (SS) and Undersaturated (SU) rocks (234 Ma; Casetta *et al.*, 2018*a*). DMM (Workman & Hart, 2005) and EMI (Zindler & Hart, 1986) mantle end-members (corrected to 220 Ma) are also reported for comparison.

Fig. 12. (colour online)

(**a**) Al_2O_3/TiO_2 and (**b**) FeO vs. MgO diagrams showing the Fractional Crystallization (FC) vectors used to simulate the compositional trend of Predazzo lamprophyres. The dotted vectors represent the contribution of the single mineral phases during FC; the black solid arrows represent the sum vector at 35% FC. The relative percentages of fractionation of the single phases are also reported. Ol = olivine; Cpx = clinopyroxene; Amph = amphibole; Ti-mt = Ti-magnetite.

Fig. 13. (colour online)

Trace element discrimination diagrams for Predazzo lamprophyres: (**a**) Th_N vs. Nb_N diagram (Saccani, 2015); (**b**) Ti/Y vs. Nb/Y diagram (Pearce, 1982); (**c**) Zr/Y vs. Zr diagram (Pearce and Norry, 1979); (**d**) Th-Hf-Ta ternary diagram (Wood, 1980); (**e**) Zr-Nb-Y ternary diagram (Meschede, 1986). Fractional Crystallizazion (FC) and Assimilation and Fractional Crystallization (AFC) vectors reported in (**a**) are in accordance with Saccani (2015).

Fig. 14. (colour online)

(**a**) Nb/La vs. La/Yb diagram (Smith *et al.*, 1999) used to discriminate between the contribution of lithosphere and asthenosphere in the mantle source of Predazzo lamprophyres. (**b**) Gd/Yb vs. La/Yb and (**c**) Sm/Yb vs. La/Sm diagrams for Predazzo less differentiated camptonites. Melting curves in (**b**) and (**c**) are modelled using the non-modal batch melting equations of Shaw (1970). Starting mantle sources: I = Sp-lherzolite with DMM composition (Workman & Hart, 2005); II = Sp-lherzolite; III = Grt-lherzolite; IV = Sp-Grt-Amph-lherzolite; V = Grt-Amph-lherzolite; VI = Grt-Phlog-lherzolite. Starting REE composition of II, III, IV, V and VI sources is fertile PM of Sun & McDonough (1989). Source modal composition, melting proportions and partition coefficients for olivine, orthopyroxene, clinopyroxene, spinel, garnet, amphibole and phlogopite are reported in Table 9. (**d**) Chondrite-normalized (Sun & McDonough, 1989) REE patterns of Predazzo less differentiated camptonites compared to those simulated by partial melting of a garnet-amphibole-lherzolite (curve V) at partial melting degrees of 0.5 to 10%.

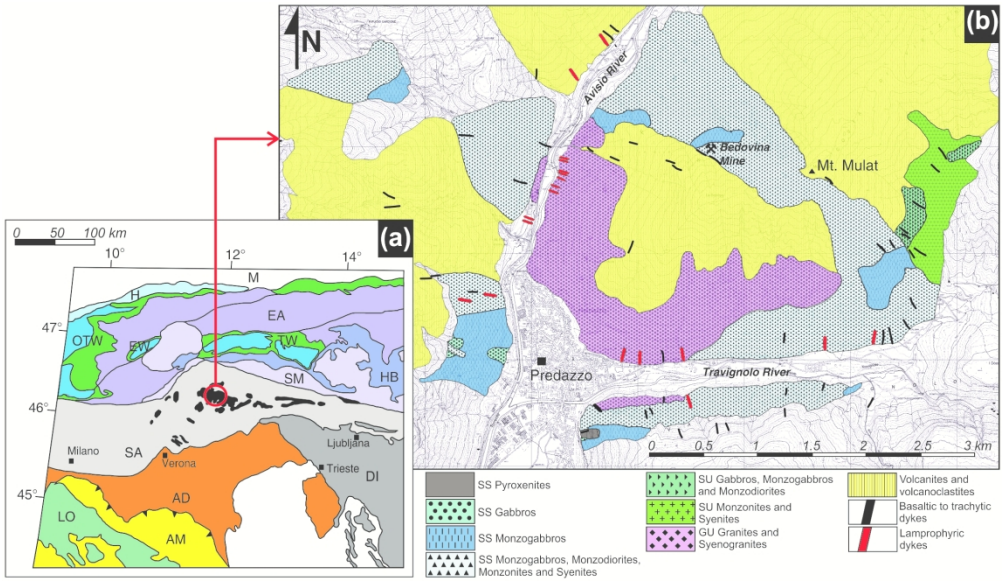

Fig. 1. (colour online)
(a) Map of the tectonic units of the eastern portion of the Alps (partly modified from Castellarin et al., 1988; Dal Piaz et al., 2003; Schmid et al., 2016). LO: Ligurian Ophiolites; AM: deformed Adriatic margin; AD: Adriatic Microplate; SA: Southern Alps; DI: Dinarides; SM: Southern margin of Meliata; HB: Eoalpine High-Pressure Belt; TW: Tauern tectonic Window; EW: Engadine tectonic Window; OTW: Ossola-Tessin tectonic Window; EA: Eastern Austroalpine; H: Helvetic domain; M: Molasse foredeep. The Middle Triassic magmatic occurrences in the Southern Alps domain are evidenced in black. They are, from west to east: Brescian Alps, Alto Vicentino, Valsugana, Dolomitic Area, Carnia and Karawanken. (b) Simplified geological map of the Predazzo Intrusive Complex (PIC), showing the occurrence of lamprophyric dykes (modified from Casetta et al., 2018a).

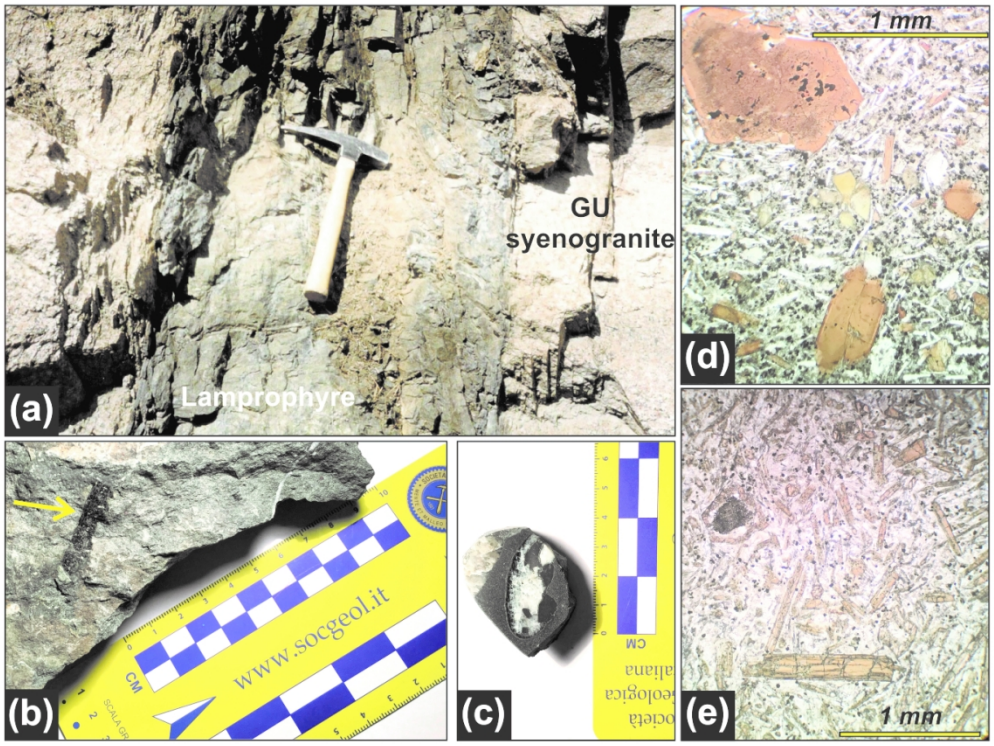

Fig. 2. (colour online)
(a) Lamprophyric dyke intruded in the Granitic Unit (GU) syenogranite at Predazzo. (b) Amphibole megacrysts (indicated by the arrow) and (c) clinopyroxenitic xenolith included in the lamprophyric rocks. On the right, photomicrographs in transmitted plane-polarized light of (d) a camptonitic and (e) bostonitic lamprophyre (sample MA1).

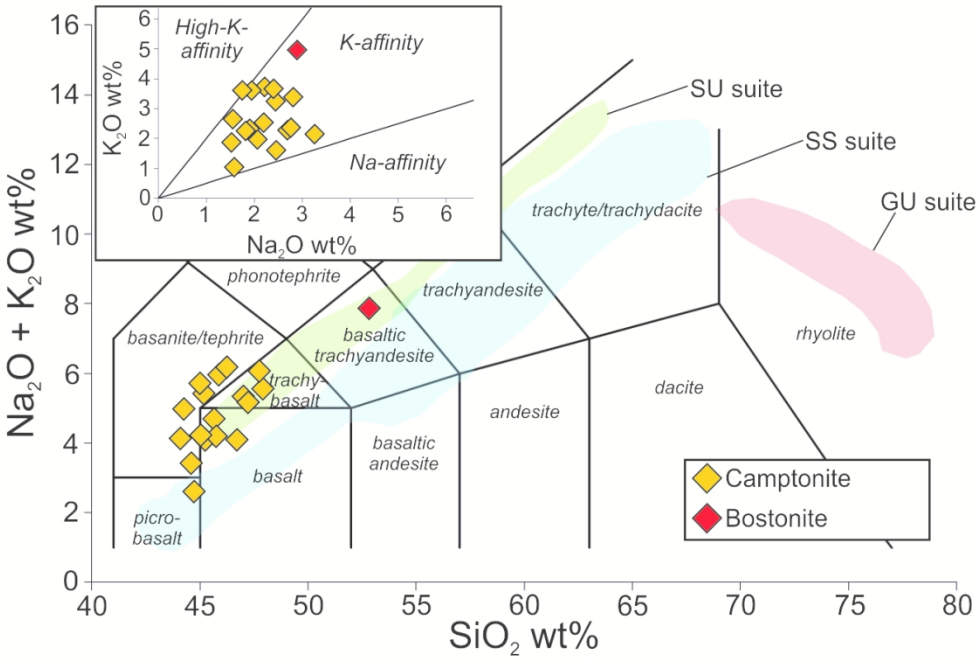

Fig. 3. (colour online)
Total Alkali vs. Silica (TAS) diagram (Le Maitre et al., 2002) and K2O vs. Na2O diagram (insert up on the left) showing the composition of Predazzo camptonitic and bostonitic lamprophyres. Fields indicate the composition of the Shoshonitic Silica Saturated (SS), Shoshonitic Silica Undersaturated (SU) and Granitic Unit (GU) of the Predazzo Intrusive Complex (from Casetta et al., 2018a; 2018b).

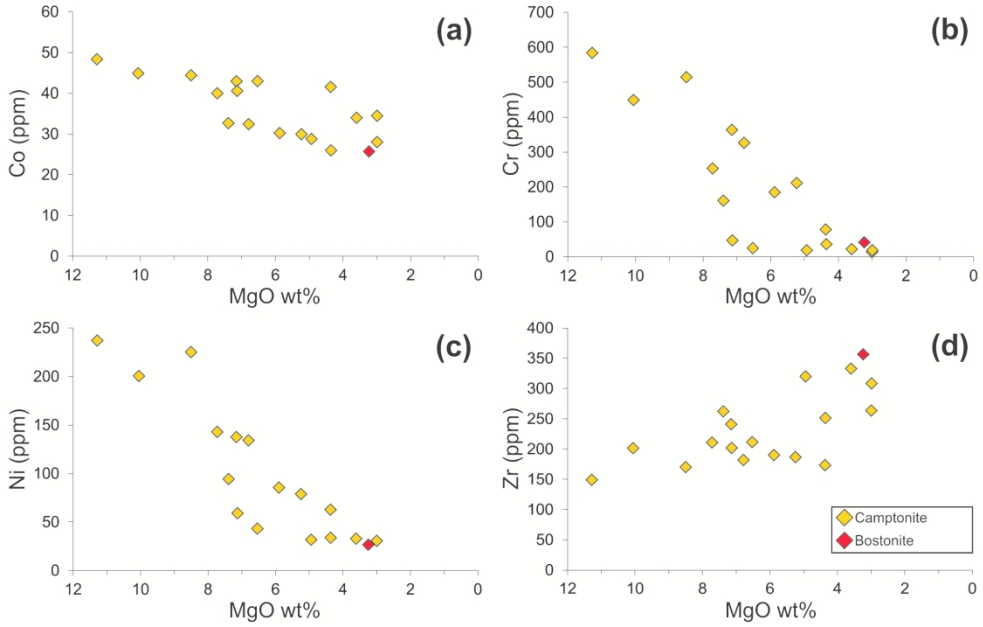

Fig. 4. (colour online)
(a) Co, (b) Cr, (c) Ni and (d) Zr vs. MgO variation diagrams for Predazzo lamprophyres.

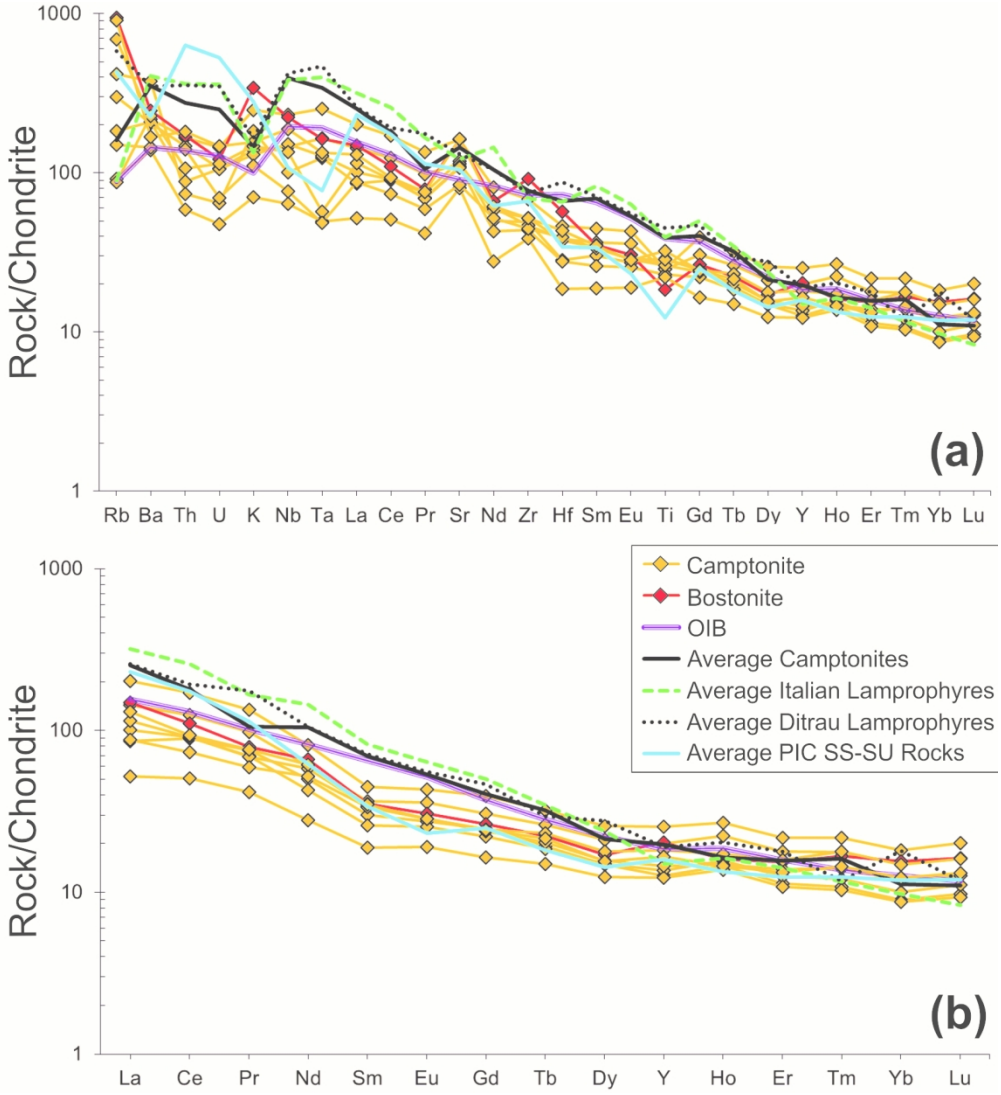

Fig. 5. (colour online)
Chondrite-normalized (Sun & McDonough, 1989) trace element (a) and REE patterns (b) of Predazzo camptonitic and bostonitic dykes. The OIB pattern (Sun & McDonough, 1989), the average composition of the worldwide camptonites (Rock, 1991), Italian lamprophyres (Galassi et al., 1994; Vichi et al., 2005; Stoppa et al., 2008; 2014), Ditrau lamprophyres (Batki et al., 2014) and Predazzo Intrusive Complex Shoshonitic Silica Saturated (SS) and Undersaturated (SU) rocks (Casetta et al., 2018a; 2018b) are reported for comparison.

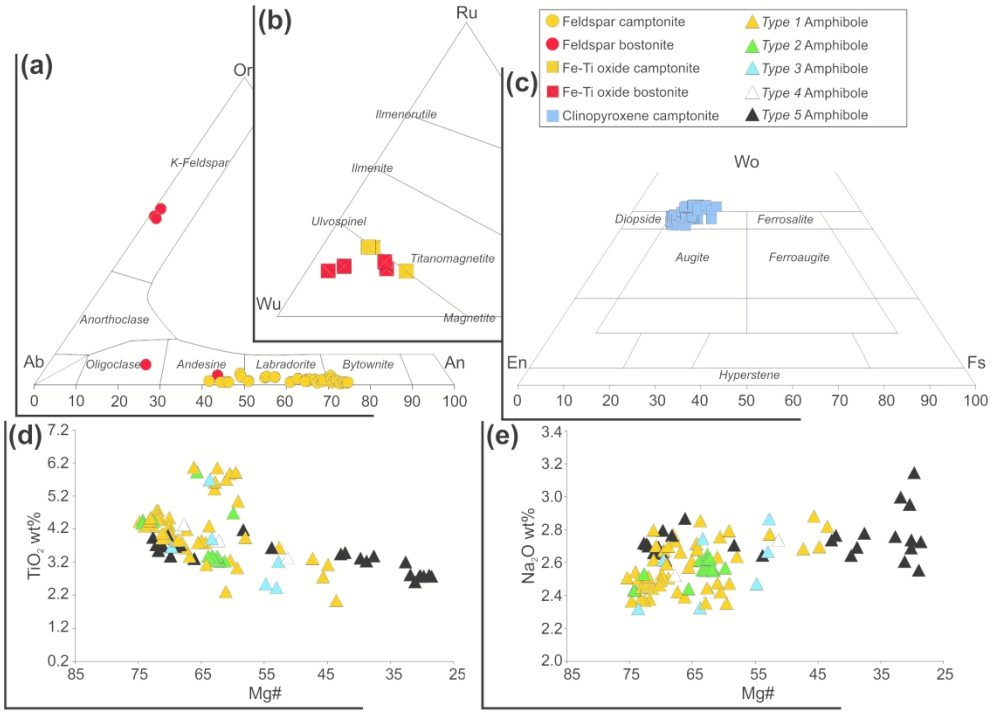

Fig. 6. (colour online)
Mineral phase classification diagrams showing the composition of the main crystals of Predazzo camptonites and bostonite. (a) Orthoclase-Albite-Anorthite ternary diagram for plagioclase and K-Feldspar; (b) Rutile-Wustite-Hematite ternary diagram for Fe-Ti oxide; (c) Wollastonite-Enstatite-Ferrosilite diagram for clinopyroxene. (d) TiO2 and (e) Na2O vs. Mg# diagrams for amphibole crystals, discriminating between the five textural types (see text).

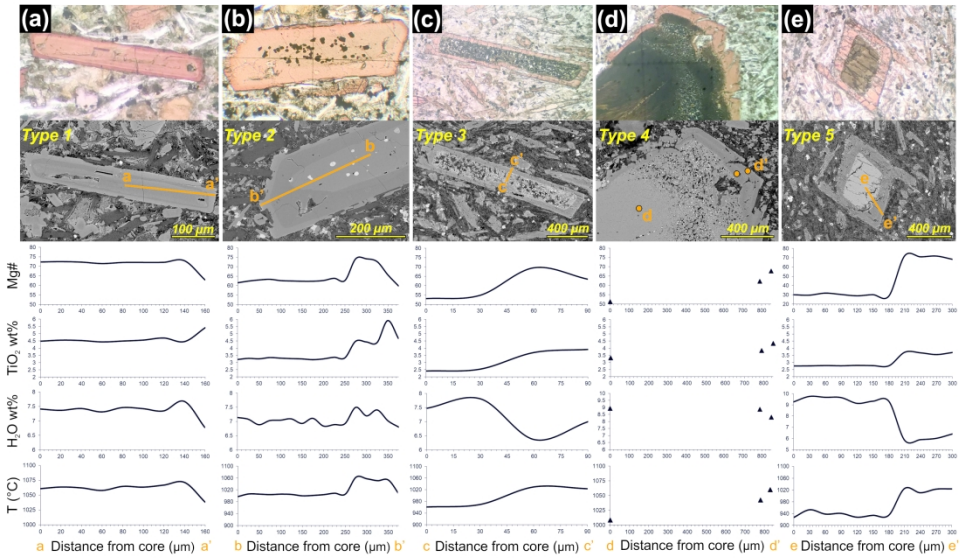

Fig. 7. (colour online)
Photomicrographs in transmitted plane-polarized light, back scattered SEM images and core-to-rim compositional (Mg# and TiO2) profiles of (a) Type 1, (b) Type 2, (c) Type 3, (d) Type 4 and (e) Type 5 amphiboles recognized in Predazzo camptonites and bostonite. For each amphibole type, the determination of the water content (H2O wt%) dissolved in the melt obtained by the equation of Ridolfi et al. (2010) and the crystallization temperature (T °C) calculated by means of Putirka (2016) thermometer are also reported.

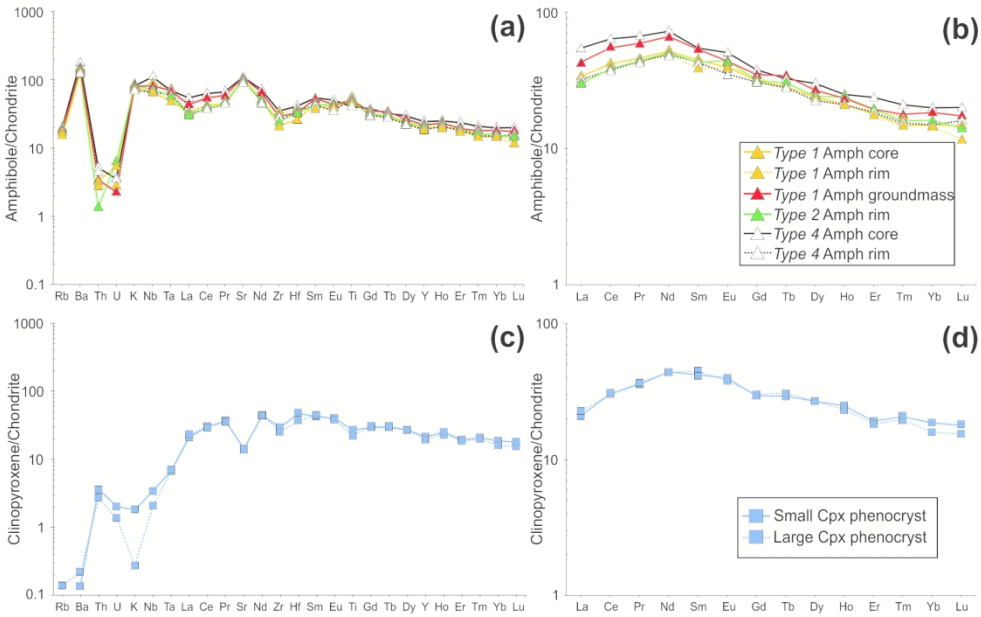

Fig. 8. (colour online)
Chondrite-normalized (Sun & McDonough, 1989) trace element (a, c) and REE (b, d) patterns of amphibole (Amph) and clinopyroxene (Cpx) crystals. Solid lines: core composition; dotted lines: rim composition.

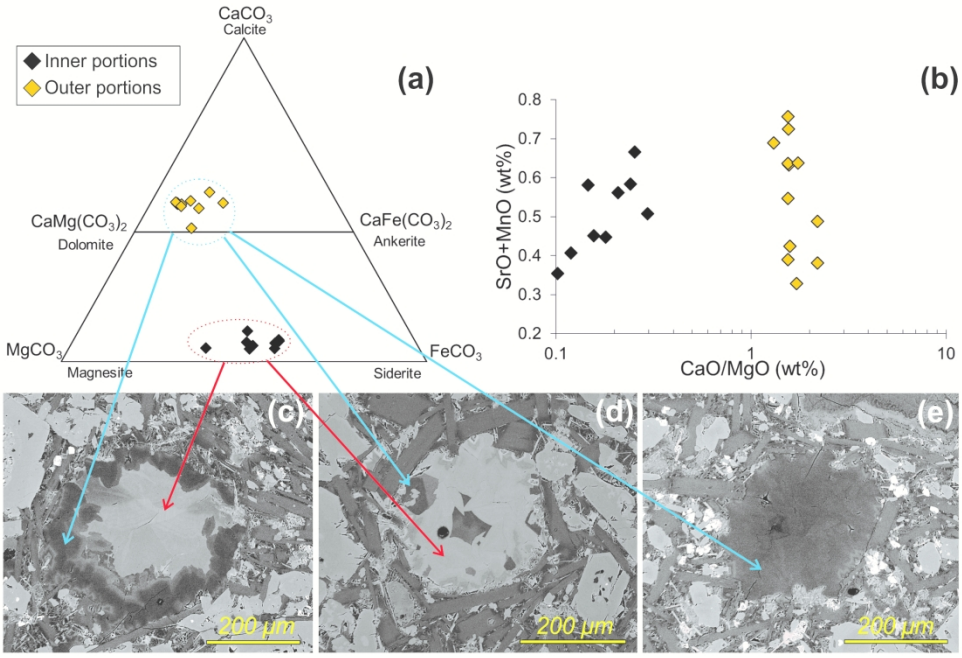

Fig. 9. (colour online)
Compositional and textural features of the carbonate ocelli inside Predazzo lamprophyres. (a) Calcite-magnesite-siderite ternary diagram and (b) SrO+MnO vs. CaO/MgO diagram (after Vichi et al., 2005) showing the composition of carbonates from the inner and outer portions of the ocelli. (c, d, e) Back scattered SEM images of carbonate ocelli composed of (c, d) both dolomite-ankerite/magnesite-siderite or (e) dolomite-ankerite crystals only. The flow-aligned tangential growth of amphibole, plagioclase and clinopyroxene is particularly evident in (d) and (e).

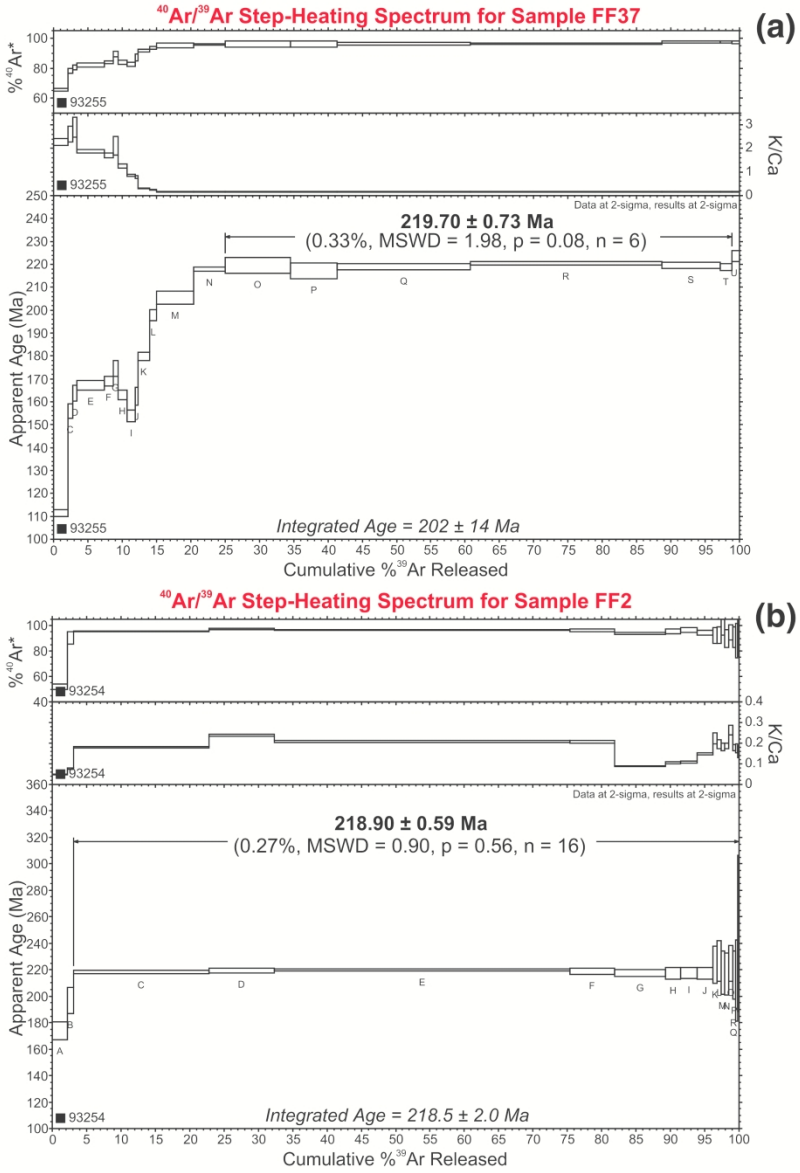

Fig. 10. (colour online)
40Ar/39Ar Age spectra for mineral separates from Predazzo camptonites, with apparent ages and K/Ca ratios spectra plotted against the cumulative percentage of 39Ar released. (a) Age spectrum yielded by amphibole crystals from sample FF37; (b) age spectrum yielded by plagioclase crystals from sample FF2. Plateau ages are indicated in bold.

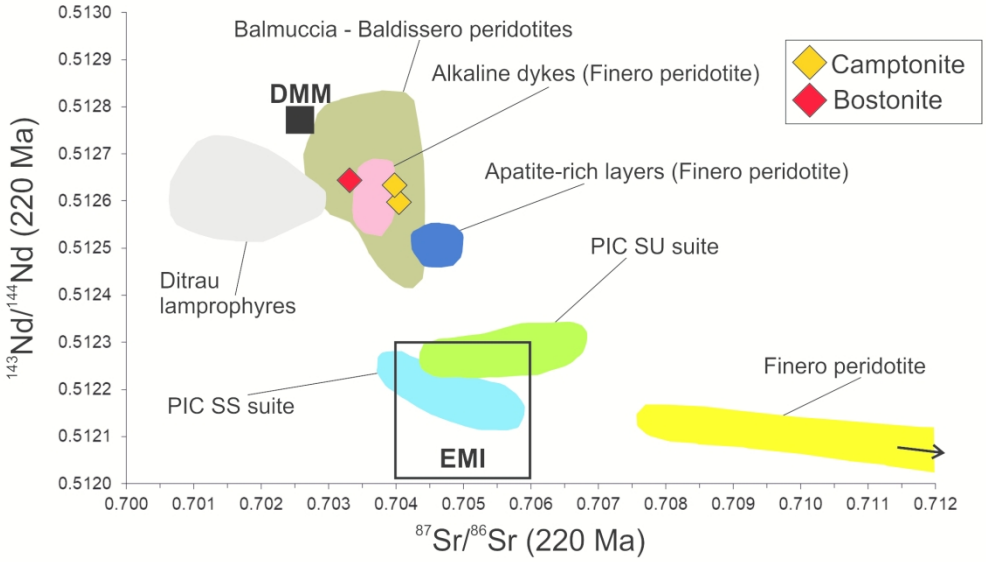

Fig. 11. (colour online)
87Sr/86Sr vs. 143Nd/144Nd diagram showing the isotopic signature of Predazzo lamprophyres corrected to 220 Ma. Fields indicate the Sr-Nd isotopic signature of the: Finero (Voshage et al., 1987), Balmuccia and Baldissero peridotites (Mukasa & Shervais 1999; Mazzucchelli et al., 2009); alkaline dykes intruded in the Finero peridotite (220 Ma; Stahle et al., 2001); apatite-rich layers of the Finero peridotite (215 Ma; Morishita et al., 2008); Ditrau lamprophyres (220 Ma; Batki et al., 2014); Predazzo Intrusive Complex (PIC) Shoshonitic Silica Saturated (SS) and Undersaturated (SU) rocks (234 Ma; Casetta et al., 2018a). DMM (Workman & Hart, 2005) and EMI (Zindler & Hart, 1986) mantle end-members (corrected to 220 Ma) are also reported for comparison.

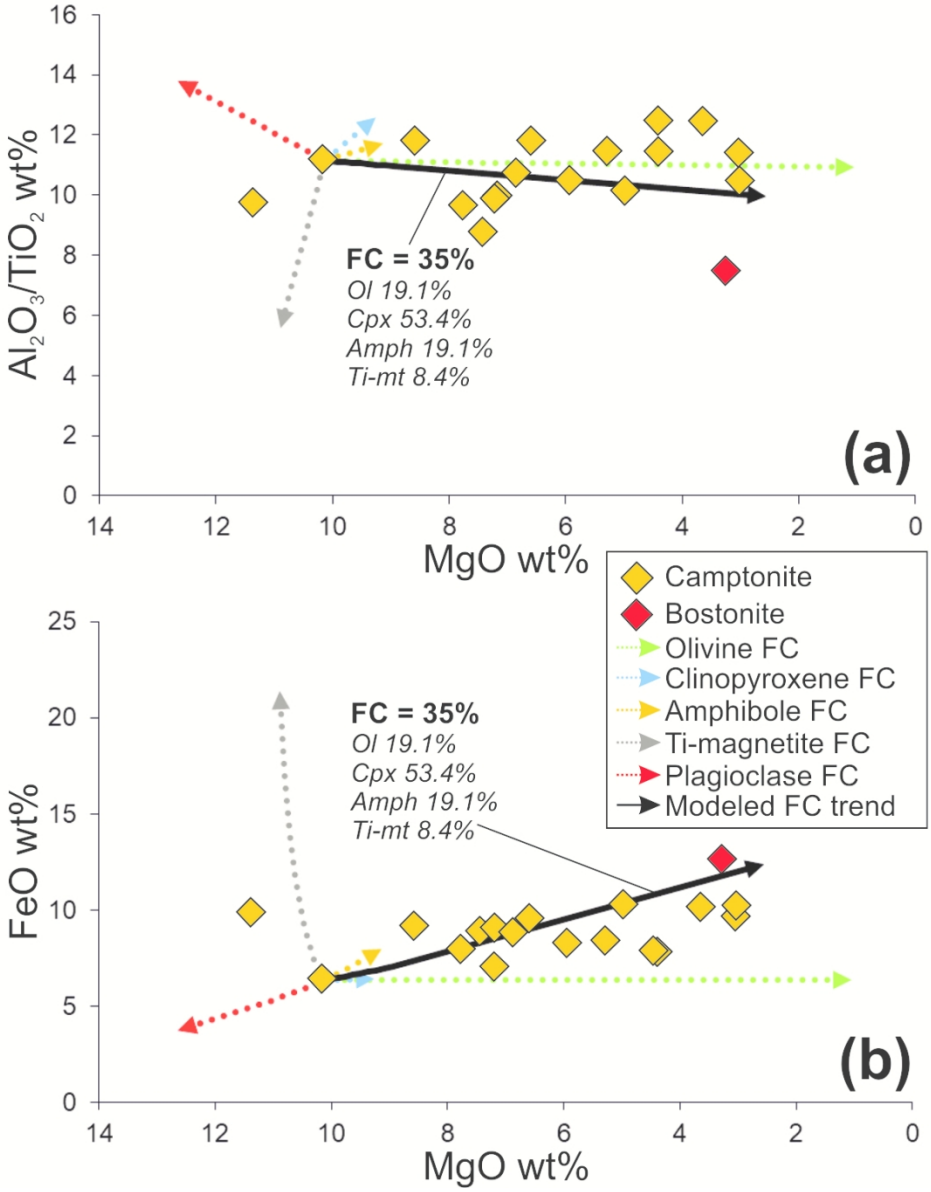

Fig. 12. (colour online)
(a) Al2O3/TiO2 and (b) FeO vs. MgO diagrams showing the Fractional Crystallization (FC) vectors used to simulate the compositional trend of Predazzo lamprophyres. The dotted vectors represent the contribution of the single mineral phases during FC; the black solid arrows represent the sum vector at 35% FC. The relative percentages of fractionation of the single phases are also reported. Ol = olivine; Cpx = clinopyroxene; Amph = amphibole; Ti-mt = Ti-magnetite.

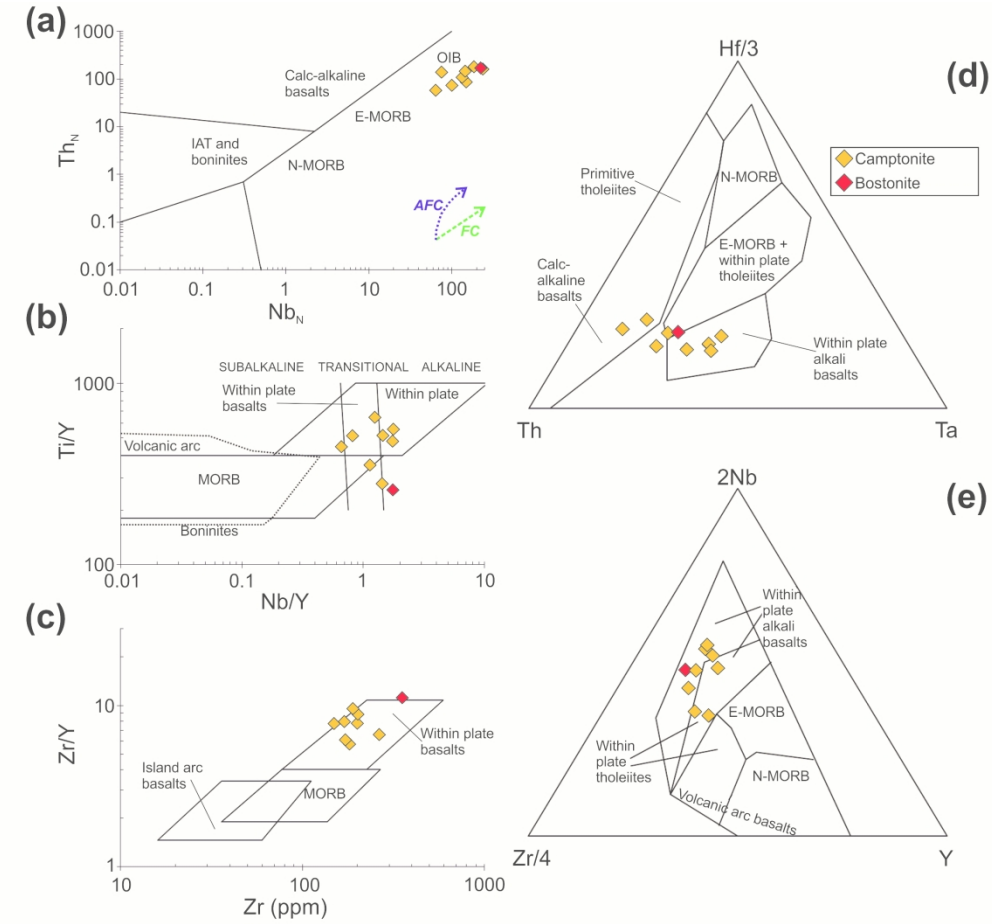

Fig. 13. (colour online)
Trace element discrimination diagrams for Predazzo lamprophyres: (a) ThN vs. NbN diagram (Saccani, 2015); (b) Ti/Y vs. Nb/Y diagram (Pearce, 1982); (c) Zr/Y vs. Zr diagram (Pearce and Norry, 1979); (d) Th-Hf-Ta ternary diagram (Wood, 1980); (e) Zr-Nb-Y ternary diagram (Meschede, 1986). Fractional Crystallizazion (FC) and Assimilation and Fractional Crystallization (AFC) vectors reported in (a) are in accordance with Saccani (2015).

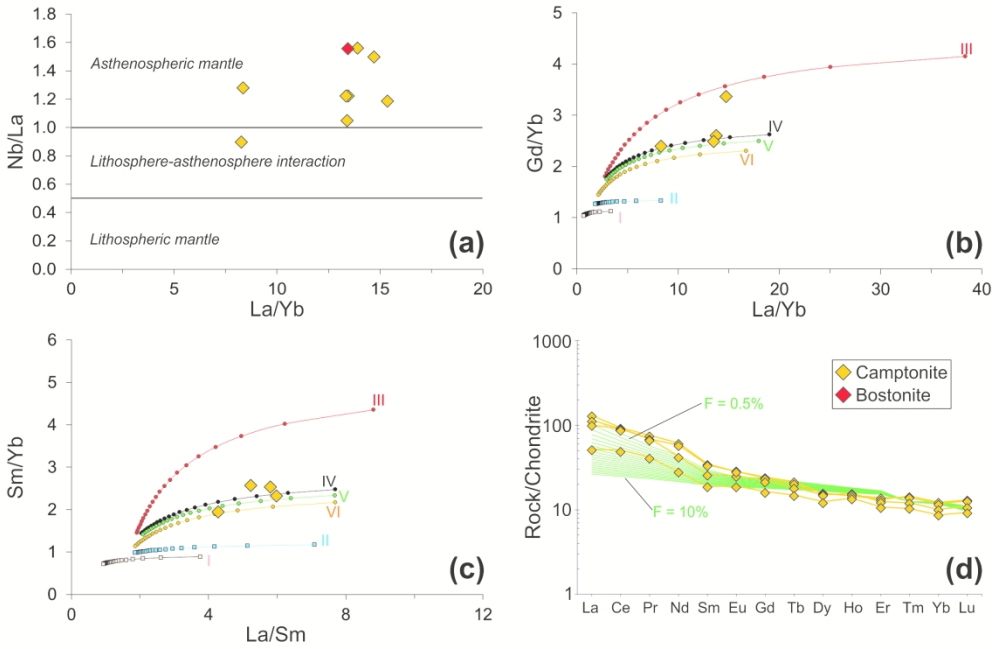

Fig. 14. (colour online)
(a) Nb/La vs. La/Yb diagram (Smith et al., 1999) used to discriminate between the contribution of lithosphere and asthenosphere in the mantle source of Predazzo lamprophyres. (b) Gd/Yb vs. La/Yb and (c) Sm/Yb vs. La/Sm diagrams for Predazzo less differentiated camptonites. Melting curves in (b) and (c) are modelled using the non-modal batch melting equations of Shaw (1970). Starting mantle sources: I = Sp-lherzolite with DMM composition (Workman & Hart, 2005); II = Sp-lherzolite; III = Grt-lherzolite; IV = Sp-Grt-Amph-lherzolite; V = Grt-Amph-lherzolite; VI = Grt-Phlog-lherzolite. Starting REE composition of II, III, IV, V and VI sources is fertile PM of Sun & McDonough (1989). Source modal composition, melting proportions and partition coefficients for olivine, orthopyroxene, clinopyroxene, spinel, garnet, amphibole and phlogopite are reported in Table 9. (d) Chondrite-normalized (Sun & McDonough, 1989) REE patterns of Predazzo less differentiated camptonites compared to those simulated by partial melting of a garnet-amphibole-lherzolite (curve V) at partial melting degrees of 0.5 to 10%.

Table 1: Whole rock major, trace element composition and $^{87}Sr/^{86}Sr$ and $^{143}Nd/^{144}Nd$ isotopes of Predazzo lamprophyres. Fe_2O_3 and FeO were calculated by considering a Fe_2O_3/ FeO ratio of 0.15, in agreement with a fO_2 around FMQ buffer (Kress & Carmichael, 1991). Mg# = Mg/[Mg+Fe^{2+}] mol%; n.d. = not detected. All trace element (ppm) were analysed by ICP-MS except Pb, Zn, Ni, Co, Cr, V and Ba (XRF). The trace element composition of samples labelled with (*) was entirely determined by XRF. Sr-Nd isotopic ratios were corrected for 220 Ma of radiogenic ingrowth using the trace element abundances determined by ICP-MS, the decay rates of Rotenberg *et al.* (2012) and Lugmair & Marti (1978). Initial ratios (i) and uncertainties (2σ) were propagated according to Ickert (2013). Camp: Camptonite; Bost: Bostonite

Lithology	Camp	Camp	Camp	Camp	Camp	Camp	Camp	Camp	Camp	Camp	Camp	Camp	Camp	Camp	Camp	Camp	Camp	Bost
Sample	222*	A 71*	FF2*	FF17*	FF22*	FF26*	S3*	FF37*	FF38*	EM97	EM99	FF14	EM20A	EM87	EM37A	FC80	MA5	MA1
Oxide (wt%)																		
SiO_2	47.22	47.90	45.00	44.29	45.02	46.20	47.72	45.86	45.63	45.74	47.00	44.07	45.24	44.59	44.73	45.16	46.67	52.81
TiO_2	2.00	1.83	1.87	2.13	2.31	2.30	2.00	1.82	1.91	2.14	1.85	2.41	1.84	1.71	1.65	1.96	2.13	1.37
Al_2O_3	16.74	18.82	17.97	17.01	16.23	18.15	17.77	18.46	18.36	17.62	18.78	15.29	16.39	15.75	16.25	17.74	16.65	17.45
Fe_2O_3	1.50	1.33	1.49	1.26	1.30	1.63	1.15	1.63	1.55	1.37	1.37	1.46	1.41	1.55	1.29	1.31	1.50	0.98
FeO	9.99	8.83	9.91	8.45	8.65	10.86	7.65	10.83	10.32	9.15	9.10	9.74	9.38	10.30	8.54	8.71	10.02	6.53
MnO	0.23	0.19	0.23	0.19	0.23	0.17	0.18	0.18	0.15	0.20	0.20	0.18	0.22	0.20	0.20	0.18	0.17	0.16
MgO	5.24	4.93	2.99	7.72	7.15	4.36	7.39	3.60	6.53	5.88	3.00	10.06	6.80	8.49	11.28	7.13	4.37	3.23
CaO	11.25	9.71	13.88	13.43	14.24	9.05	9.66	10.73	10.26	13.03	12.49	11.92	13.81	13.21	12.86	11.80	13.95	8.83
Na_2O	2.77	1.95	2.45	2.73	1.92	2.81	2.40	2.23	2.20	1.56	1.75	1.89	2.08	1.54	1.59	3.27	2.47	2.90
K_2O	2.38	3.61	3.25	2.27	2.29	3.37	3.66	3.74	2.48	2.64	3.58	2.25	2.01	1.89	1.02	2.14	1.61	4.97
P_2O_5	0.68	0.90	0.95	0.51	0.65	1.10	0.43	0.92	0.60	0.65	0.86	0.73	0.81	0.78	0.60	0.60	0.44	0.77
Tot.	100.00	100.00	100.00	100.00	100.00	100.00	100.00	100.00	100.00	100.00	100.00	100.00	100.00	100.00	100.00	100.00	100.00	100.00
Mg#	48.30	49.90	34.97	61.94	59.58	41.68	63.24	37.20	52.99	53.41	36.96	64.77	56.34	59.52	70.19	59.33	43.75	46.88
LOI	6.65	3.72	6.39	4.92	5.41	5.88	5.52	5.53	4.81	5.33	6.53	5.70	6.11	5.13	6.68	5.17	7.36	5.94
Trace element (ppm)																		
Pb	28.0	8.20	12.0	13.0	10.0	11.0	15.4	26.0	13.7	5.60	22.2	11.0	12.2	15.8	21.4	16.0	34.0	8.7
Zn	128	79.5	69.0	65.0	79.0	119	143	124	216	110	122	97.0	90.1	88.0	107	80.7	145	77.9
Ni	79.0	31.8	31.0	143	138	34.0	94.5	33.0	43.3	85.5	30.9	201	135	226	237	59.4	62.8	27.3
Co	30.0	28.8	28.0	40.0	43.0	26.0	32.7	34.0	43.0	30.3	34.5	45.0	32.4	44.4	48.4	40.6	41.6	25.8
Cr	211	19.8	14.0	254	364	37.0	161	23.0	24.9	185	16.0	449	326	514	585	46.8	78.9	42.2
V	144	112	124	238	231	134	197	130	187	222	125	220	167	170	212	191	223	92.8
Rb	52.0	82.8	239	114	48.0	105	102	238	54.0	146	242	318	105	63.9	32.0	30.5	52.7	331
Ba	535	790	528	542	510	571	991	522	576	910	525	405	496	504	334	546	350	590
Sr	1187	1305	1247	661	807	1545	1085	1183	1069	862	1175	1190	829	795	581	780	609	1181
Nb	45.0	58.4	60.0	16.0	30.0	72.0	n.d.	63.0	n.d.	24.9	56.9	46.2	35.8	37.2	15.8	33.3	18.8	55.2
Zr	187	321	309	211	241	251	262	333	212	190	264	201	182	170	150	202	173	356
Hf										3.03	4.96	4.62	4.08	2.95	1.99	4.02	4.19	6.11
U										0.52	1.16	1.18	0.86	0.85	0.38	0.91	0.56	0.98
Th										2.13	4.83	5.26	4.29	2.55	1.71	3.10	4.09	4.96
Y	22.0	31.6	25.0	24.0	23.0	26.0	33.3	27.0	30.3	19.9	39.8	26.0	31.4	21.5	19.4	22.8	28.5	31.9
Ta										1.74	3.53	1.88	2.32	1.80	0.69	0.80	0.68	2.30
La	45.0	71.5	38.0	11.0	27.0	61.0	55.9	37.0	48.4	20.4	47.7	30.9	34.0	23.8	12.3	27.2	20.8	35.4
Ce	79.0	121	125	64.0	42.0	109	93.8	86.0	49.5	54.8	105	57.2	76.2	55.9	31.1	55.6	45.1	67.5
Pr										7.17	12.8	7.21	9.27	6.61	3.96	6.53	5.65	7.51
Nd										23.4	37.8	28.7	28.1	20.0	13.0	27.2	24.3	31.0
Sm										4.62	6.86	5.32	5.58	3.98	2.88	5.19	5.13	5.37
Eu										1.58	2.50	1.64	2.08	1.48	1.11	1.65	1.65	1.77
Gd										5.10	8.08	5.01	6.29	4.54	3.39	4.92	5.05	5.45
Tb										0.72	1.20	0.81	0.98	0.69	0.56	0.76	0.86	0.84
Dy										3.76	6.53	3.96	5.39	3.81	3.16	3.99	4.53	4.34
Ho										0.82	1.52	0.83	1.26	0.89	0.78	0.84	0.98	0.91
Er										1.88	3.59	2.20	2.97	2.07	1.80	2.31	2.61	2.55
Tm										0.28	0.55	0.37	0.45	0.31	0.26	0.36	0.45	0.43
Yb										1.52	3.10	2.09	2.54	1.71	1.48	2.02	2.52	2.64
Lu										0.25	0.51	0.33	0.41	0.28	0.24	0.32	0.41	0.41
$^{87}Sr/^{86}Sr$												0.706376				0.704373		0.705787
$^{87}Rb/^{86}Sr$												0.7733				0.1129		0.8098
$^{87}Sr/^{86}Sr_{(i)}$												0.703996				0.704025		0.703295
2σ												0.000031				0.000020		0.000030
$^{143}Nd/^{144}Nd$												0.512795				0.512765		0.512796
$^{147}Sm/^{144}Nd$												0.1118				0.1152		0.1047
$^{143}Nd/^{144}Nd_{(i)}$												0.512634				0.512599		0.512645
2σ												0.000006				0.000006		0.000007

Table 2: Major element core to rim analyses and a.p.f.u. calculation of representative amphibole types from Predazzo lamprophyres. A.p.f.u. were calculated using the Lockock (2014) computation; the classification follows the recommendations of the IMA-CNMNC subcommittee on amphiboles (Hawthorne *et al.*, 2012; Oberti *et al.*, 2012)

Sample	FC80 - Camptonite									FC80 – Camptonite														
Amphibole type	*Type 1*									*Type 2*														
Name	Am1_c	Am1_tr1	Am1_tr2	Am1_tr3	Am1_tr4	Am1_tr5	Am1_tr6	Am1_tr7	Am1_r	Am4_c	Am4_tr1	Am4_tr2	Am4_tr3	Am4_tr4	Am4_tr5	Am4_tr6	Am4_tr7	Am4_tr8	Am4_tr9	Am4_tr10	Am4_tr11	Am4_tr12	Am4_tr13	Am4_tr14	Am4_r
Oxyde (wt%)																								
SiO_2	39.456	39.460	39.315	39.213	39.224	39.412	39.345	38.865	39.353	39.687	39.567	39.625	39.816	39.634	39.599	39.801	39.721	39.715	39.835	39.503	39.735	39.958	40.207	39.575	40.113
TiO_2	4.475	4.548	4.522	4.426	4.487	4.553	4.696	4.450	5.407	3.208	3.285	3.254	3.343	3.300	3.269	3.248	3.195	3.249	3.362	3.320	4.475	4.431	4.384	5.920	4.671
Al_2O_3	15.137	15.130	15.154	15.117	15.197	15.145	15.034	15.553	12.907	14.502	14.608	14.513	14.422	14.436	14.522	14.435	14.547	14.532	14.488	14.456	15.007	14.708	14.618	13.098	12.745
Cr_2O_3	0.097	0.081	0.087	0.076	0.073	0.068	0.080	0.121	0.007	0.000	0.009	0.001	0.000	0.000	0.002	0.001	0.000	0.002	0.000	0.000	0.129	0.120	0.016	0.012	0.000
FeO_{TOT}	9.284	9.253	9.265	9.664	9.351	9.382	9.334	8.918	12.204	13.256	12.909	12.811	12.658	12.748	12.854	13.007	12.910	12.864	12.407	12.899	8.558	8.650	9.197	11.280	13.322
MnO	0.097	0.081	0.136	0.101	0.096	0.084	0.096	0.125	0.196	0.159	0.169	0.136	0.126	0.137	0.154	0.109	0.178	0.164	0.156	0.159	0.096	0.091	0.116	0.148	0.241
MgO	13.584	13.675	13.509	13.571	13.512	13.570	13.542	13.502	11.614	11.909	12.036	12.258	12.291	12.007	12.016	12.078	11.991	12.153	12.317	12.191	13.842	13.973	13.753	12.134	11.133
CaO	11.901	11.897	11.745	11.572	11.933	11.770	11.927	11.963	11.900	11.360	11.429	11.461	11.459	11.448	11.441	11.544	11.481	11.347	11.473	11.542	12.205	12.128	12.027	12.359	11.833
Na_2O	2.456	2.482	2.452	2.437	2.502	2.516	2.514	2.448	2.577	2.549	2.612	2.591	2.548	2.637	2.605	2.551	2.583	2.607	2.609	2.544	2.430	2.434	2.529	2.433	2.570
K_2O	1.164	1.142	1.162	1.115	1.147	1.119	1.135	1.182	1.053	1.180	1.192	1.206	1.165	1.189	1.185	1.246	1.208	1.249	1.231	1.199	1.148	1.157	1.026	1.045	1.105
NiO	0.003	0.011	0.004	0.000	0.015	0.000	0.046	0.034	0.000	0.004	0.000	0.037	0.015	0.004	0.000	0.004	0.000	0.008	0.031	0.000	0.014	0.020	0.057	0.000	0.000
F	0.339	0.265	0.178	0.360	0.290	0.270	0.379	0.327	0.585	0.110	0.281	0.263	0.221	0.275	0.238	0.237	0.083	0.209	0.185	0.226	0.263	0.337	0.295	0.476	0.579
Cl	0.000	0.028	0.000	0.041	0.000	0.030	0.066	0.020	0.036	0.047	0.000	0.000	0.074	0.031	0.000	0.013	0.026	0.000	0.053	0.000	0.000	0.036	0.000	0.049	0.000
Tot.	97.993	98.054	97.529	97.694	97.826	97.919	98.194	97.508	97.837	97.970	98.097	98.155	98.137	97.846	97.885	98.274	97.923	98.098	98.149	98.039	97.905	98.042	98.225	98.528	98.310
Mg#	**72.3**	**72.5**	**72.2**	**71.4**	**72.0**	**72.0**	**72.1**	**73.0**	**62.9**	**61.6**	**62.4**	**63.0**	**63.4**	**62.7**	**62.5**	**62.3**	**62.3**	**62.7**	**63.9**	**62.7**	**74.2**	**74.2**	**72.7**	**65.7**	**59.8**
$Fe^{3+}/\Sigma Fe$ used	0.904	0.91	0.903	0.904	0.909	0.898	0.912	0.926	0.618	0.574	0.58	0.605	0.605	0.549	0.567	0.562	0.554	0.581	0.584	0.615	0.916	0.913	0.814	0.713	0.478
Group	OH,F,Cl	oxo	oxo	OH,F,Cl	OH,F,Cl	oxo	oxo	OH,F,Cl	oxo	OH,F,Cl	OH,F,Cl	OH,F,Cl	OH,F,Cl	OH,F,Cl	OH,F,Cl	OH,F,Cl	OH,F,Cl	OH,F,Cl	OH,F,Cl	OH,F,Cl	OH,F,Cl	OH,F,Cl	OH,F,Cl	OH,F,Cl	oxo	oxo
Subgroup of (OH,F,Cl)	Ca	B = Ca	B = Ca	Ca	Ca	B = Ca	B = Ca	Ca	B = Ca	Ca	Ca	Ca	Ca	Ca	Ca	Ca	Ca	Ca	Ca	Ca	Ca	Ca	Ca	Ca	B = Ca	B = Ca
Species	magnesio-hastingsite	ferri-kaersutite	ferri-kaersutite	magnesio-hastingsite	magnesio-hastingsite	ferri-kaersutite	ferri-kaersutite	magnesio-hastingsite	ferri-kaersutite	Ti-rich magnesio-hastingsite	Ti-rich magnesio-hastingsite	Ti-rich magnesio-hastingsite	Ti-rich magnesio-hastingsite	Ti-rich magnesio-hastingsite	Ti-rich magnesio-hastingsite	Ti-rich magnesio-hastingsite	Ti-rich magnesio-hastingsite	Ti-rich magnesio-hastingsite	Ti-rich magnesio-hastingsite	Ti-rich magnesio-hastingsite	magnesio-hastingsite	magnesio-hastingsite	magnesio-hastingsite	ferri-kaersutite	ferri-kaersutite
Formula Assignments																									
(T) Si	5.794	5.789	5.792	5.778	5.771	5.791	5.782	5.736	5.941	5.89	5.872	5.869	5.894	5.902	5.887	5.897	5.896	5.886	5.898	5.859	5.827	5.856	5.889	5.909	6.04
(T) Al	2.206	2.211	2.208	2.222	2.229	2.209	2.218	2.264	2.059	2.11	2.128	2.131	2.106	2.098	2.113	2.103	2.104	2.114	2.102	2.141	2.173	2.144	2.111	2.091	1.96
(T) Ti	0	0	0	0	0	0	0	0	0	0	0	0	0	0	0	0	0	0	0	0	0	0	0	0	0
(C) Ti	0.494	0.502	0.501	0.491	0.497	0.503	0.519	0.494	0.614	0.358	0.367	0.363	0.372	0.37	0.366	0.362	0.357	0.362	0.375	0.371	0.494	0.488	0.483	0.665	0.529
(C) Al	0.413	0.405	0.423	0.403	0.406	0.414	0.386	0.442	0.237	0.427	0.427	0.402	0.411	0.435	0.431	0.418	0.441	0.424	0.426	0.386	0.42	0.396	0.412	0.213	0.302
(C) Cr	0.011	0.009	0.01	0.009	0.008	0.008	0.009	0.014	0.001	0	0.001	0	0	0	0	0	0	0	0	0	0.015	0.014	0.002	0.001	0
(C) Fe^{3+}	1.03	1.033	1.031	1.076	1.046	1.035	1.047	1.019	0.952	0.944	0.929	0.961	0.949	0.871	0.906	0.906	0.888	0.926	0.897	0.984	0.961	0.968	0.917	1.005	0.802
(C) Ni	0	0.001	0.001	0	0.002	0	0.005	0.004	0	0	0	0.004	0.002	0.001	0	0	0	0.001	0.004	0	0.002	0.002	0.007	0	0
(C) Mn^{2+}	0	0	0	0	0	0	0	0	0	0	0	0	0	0	0	0	0	0	0	0	0	0	0	0.011	0
(C) Fe^{2+}	0.077	0.06	0.068	0.04	0.078	0.068	0.067	0.056	0.583	0.636	0.614	0.563	0.554	0.658	0.634	0.646	0.661	0.601	0.58	0.564	0.082	0.078	0.176	0.404	0.868
(C) Mg	2.974	2.991	2.967	2.981	2.964	2.972	2.967	2.971	2.614	2.635	2.663	2.707	2.713	2.666	2.663	2.668	2.653	2.685	2.719	2.696	3.026	3.053	3.003	2.701	2.499
(B) Mn^{2+}	0.012	0.01	0.017	0.013	0.012	0.01	0.012	0.016	0.025	0.02	0.021	0.017	0.016	0.017	0.019	0.014	0.022	0.021	0.02	0.02	0.012	0.011	0.014	0.007	0.031
(B) Fe^{2+}	0.033	0.043	0.043	0.075	0.027	0.05	0.034	0.026	0.007	0.065	0.059	0.063	0.064	0.059	0.059	0.06	0.054	0.067	0.059	0.052	0.006	0.014	0.033	0	0.008
(B) Ca	1.872	1.87	1.854	1.827	1.881	1.853	1.878	1.892	1.925	1.806	1.817	1.819	1.818	1.827	1.822	1.833	1.826	1.802	1.82	1.834	1.918	1.904	1.887	1.977	1.909
(B) Na	0.083	0.077	0.087	0.086	0.08	0.087	0.076	0.067	0.043	0.108	0.102	0.102	0.102	0.097	0.1	0.094	0.098	0.111	0.101	0.093	0.064	0.071	0.065	0.015	0.053
(A) Ca	0	0	0	0	0	0	0	0	0	0	0	0	0	0	0	0	0	0	0	0	0	0	0	0	0
(A) Na	0.617	0.629	0.614	0.611	0.634	0.63	0.64	0.634	0.711	0.625	0.649	0.643	0.629	0.664	0.651	0.639	0.645	0.639	0.648	0.638	0.627	0.621	0.653	0.689	0.698
(A) K	0.218	0.214	0.218	0.21	0.215	0.21	0.213	0.223	0.203	0.223	0.226	0.228	0.22	0.226	0.225	0.235	0.229	0.236	0.232	0.227	0.215	0.216	0.192	0.199	0.212
O (non-W)	22	22	22	22	22	22	22	22	22	22	22	22	22	22	22	22	22	22	22	22	22	22	22	22	22
(W) OH	0.853	0.865	0.914	0.84	0.871	0.86	0.768	0.853	0.483	1.219	1.134	1.151	1.133	1.123	1.156	1.161	1.24	1.177	1.151	1.152	0.89	0.858	0.897	0.433	0.666
(W) F	0.157	0.123	0.083	0.168	0.135	0.125	0.176	0.153	0.279	0.052	0.132	0.123	0.103	0.13	0.112	0.111	0.039	0.098	0.086	0.106	0.122	0.156	0.137	0.225	0.275
(W) Cl	0	0.007	0	0.01	0	0.008	0.016	0.005	0.009	0.012	0	0	0.019	0.008	0	0.003	0.006	0	0.013	0	0	0.009	0	0.012	0
(W) O	0.99	1.005	1.003	0.982	0.994	1.007	1.039	0.989	1.229	0.717	0.734	0.726	0.745	0.74	0.732	0.725	0.714	0.725	0.75	0.742	0.988	0.978	0.967	1.33	1.059
Sum (T,C,B,A)	15.834	15.844	15.834	15.822	15.85	15.84	15.853	15.858	15.915	15.847	15.875	15.872	15.85	15.891	15.876	15.875	15.874	15.875	15.881	15.865	15.842	15.836	15.844	15.887	15.911

Table 2: (continued)

Sample	MA1 - Bostonite				FC80 - Camptonite			MA1 – Bostonite										
Amphibole type	*Type 3*				*Type 4*			*Type 5*										
Name	Am2_c	Am2_tr1	Am2_tr2	Am2_r	Am3_c	Am3_tr1	Am3_r	Am5_c	Am5_tr1	Am5_tr2	Am5_tr3	Am5_tr4	Am5_tr5	Am5_tr6	Am5_tr7	Am5_tr8	Am5_tr9	Am5_r
Oxyde (wt%)																		
SiO_2	39.088	38.649	39.990	39.134	37.475	37.671	38.310	37.416	37.227	38.800	37.863	36.037	36.968	36.020	40.965	41.475	40.666	40.164
TiO_2	2.405	2.533	3.694	3.908	3.312	3.837	4.336	2.757	2.765	2.787	2.771	2.798	2.782	2.775	3.727	3.681	3.561	3.706
Al_2O_3	13.833	14.093	14.308	13.688	15.537	15.957	15.546	15.375	16.316	16.200	16.158	14.846	15.421	14.974	13.539	13.258	13.611	13.514
Cr_2O_3	0.004	0.000	0.029	0.024	0.000	0.021	0.000	0.009	0.011	0.001	0.000	0.000	0.010	0.003	0.093	0.055	0.059	0.008
FeO_{TOT}	15.794	15.274	10.384	12.324	15.449	12.154	10.548	22.091	22.060	21.710	22.044	22.038	21.979	21.989	9.648	10.186	9.729	10.834
MnO	0.399	0.351	0.134	0.174	0.193	0.139	0.115	0.420	0.426	0.415	0.423	0.442	0.400	0.425	0.168	0.156	0.125	0.153
MgO	10.018	10.383	13.287	11.999	9.137	11.240	12.446	5.341	5.217	5.696	5.397	5.033	5.324	4.949	14.000	13.977	13.894	13.101
CaO	11.721	11.951	11.602	11.791	11.771	12.079	11.779	10.377	10.230	10.279	10.283	10.387	10.395	10.341	11.427	11.238	11.426	11.877
Na_2O	2.660	2.466	2.610	2.735	2.730	2.417	2.513	2.682	3.145	2.994	2.950	2.548	2.732	2.720	2.703	2.647	2.687	2.762
K_2O	1.132	1.073	1.297	0.994	1.182	1.130	1.024	1.396	1.320	1.351	1.364	1.372	1.357	1.316	1.189	1.127	1.153	1.071
NiO	0.000	0.016	0.000	0.026				0.007	0.000	0.017	0.018	0.012	0.000	0.000	0.046	0.038	0.009	0.014
F	0.243	0.304	0.203	0.254	0.111	0.138	0.180	0.199	0.028	0.093	0.064	0.085	0.112	0.112	0.267	0.270	0.178	0.384
Cl	0.034	0.077	0.000	0.010	0.037	0.010	0.014	0.103	0.077	0.084	0.059	0.078	0.099	0.104	0.016	0.029	0.011	0.026
Tot.	97.330	97.167	97.538	97.061	96.933	96.793	96.799	98.172	98.821	100.426	99.391	95.674	97.578	95.727	97.787	98.136	97.107	97.614
Mg#	**53.1**	**54.8**	**69.5**	**63.4**	**51.3**	**62.2**	**67.8**	**30.1**	**29.6**	**31.9**	**30.4**	**28.9**	**30.2**	**28.6**	**72.1**	**71.0**	**71.8**	**68.3**
$Fe^{3+}/\Sigma Fe$ used	0.366	0.449	0.589	0.584	0.41	0.626	0.783	0.314	0.346	0.303	0.325	0.331	0.328	0.328	0.592	0.677	0.58	0.548
Group	OH,F,Cl	OH,F,Cl	OH,F,Cl	OH,F,Cl	OH,F,Cl	OH,F,Cl	OH,F,Cl	OH,F,Cl	OH,F,Cl	OH,F,Cl	OH,F,Cl	OH,F,Cl	OH,F,Cl	OH,F,Cl	OH,F,Cl	OH,F,Cl	OH,F,Cl	OH,F,Cl
Subgroup of (OH,F,Cl)	Ca	Ca	Ca	Ca	Ca	Ca	Ca	Ca	Ca	Ca	Ca	Ca	Ca	Ca	Ca	Ca	Ca	Ca
Species	magnesio-hastingsite	magnesio-hastingsite	Ti-rich magnesio-hastingsite	Ti-rich magnesio-hastingsite	Ti-rich magnesio-hastingsite	Ti-rich magnesio-hastingsite	magnesio-hastingsite	Ti-rich ferro-ferri-sadanagaite	Ti-rich ferro-ferri-sadanagaite	Ti-rich ferro-ferri-sadanagaite	Ti-rich ferro-ferri-sadanagaite	Ti-rich ferro-ferri-sadanagaite	Ti-rich ferro-ferri-sadanagaite	Ti-rich ferro-ferri-sadanagaite	Ti-rich magnesio-hastingsite	Ti-rich magnesio-hastingsite	Ti-rich magnesio-hastingsite	Ti-rich magnesio-hastingsite
Formula Assignments																		
(T) Si	5.946	5.871	5.933	5.894	5.736	5.675	5.722	5.799	5.707	5.838	5.768	5.746	5.76	5.741	6.043	6.078	6.033	5.986
(T) Al	2.054	2.129	2.067	2.106	2.264	2.325	2.278	2.201	2.293	2.162	2.232	2.254	2.24	2.259	1.957	1.922	1.967	2.014
(T) Ti	0	0	0	0	0	0	0	0	0	0	0	0	0	0	0	0	0	0
(C) Ti	0.275	0.289	0.412	0.443	0.381	0.435	0.487	0.321	0.319	0.315	0.318	0.336	0.326	0.333	0.414	0.406	0.397	0.416
(C) Al	0.426	0.393	0.434	0.323	0.539	0.508	0.458	0.607	0.655	0.71	0.67	0.535	0.591	0.554	0.397	0.368	0.412	0.36
(C) Cr	0.001	0	0.003	0.003	0	0.003	0	0.001	0.001	0	0	0	0.001	0	0.011	0.006	0.007	0.001
(C) Fe^{3+}	0.736	0.87	0.759	0.906	0.81	0.958	1.032	0.899	0.979	0.826	0.913	0.972	0.94	0.962	0.705	0.845	0.7	0.74
(C) Ni	0	0.002	0	0.003	0	0	0	0.001	0	0.002	0.002	0.001	0	0	0.005	0.004	0.001	0.002
(C) Mn^{2+}	0.018	0.024	0	0	0.018	0	0	0	0.004	0	0	0	0	0.006	0	0	0	0
(C) Fe^{2+}	1.273	1.07	0.453	0.628	1.168	0.573	0.252	1.936	1.849	1.868	1.872	1.96	1.905	1.969	0.389	0.317	0.41	0.571
(C) Mg	2.272	2.351	2.938	2.694	2.085	2.524	2.771	1.234	1.192	1.278	1.226	1.196	1.237	1.176	3.079	3.053	3.073	2.911
(B) Mn^{2+}	0.034	0.021	0.017	0.022	0.007	0.018	0.015	0.055	0.052	0.053	0.055	0.06	0.053	0.052	0.021	0.019	0.016	0.019
(B) Fe^{2+}	0	0	0.077	0.018	0	0	0.034	0.028	0	0.037	0.024	0.007	0.019	0	0.097	0.086	0.097	0.04
(B) Ca	1.91	1.945	1.844	1.903	1.93	1.95	1.885	1.723	1.68	1.657	1.678	1.774	1.735	1.766	1.806	1.765	1.816	1.897
(B) Na	0.056	0.034	0.062	0.057	0.062	0.032	0.067	0.194	0.268	0.253	0.243	0.159	0.193	0.182	0.076	0.13	0.071	0.044
(A) Ca	0	0	0	0	0	0	0	0	0	0	0	0	0	0	0	0	0	0
(A) Na	0.729	0.692	0.688	0.741	0.748	0.673	0.661	0.612	0.667	0.62	0.628	0.628	0.632	0.658	0.697	0.622	0.702	0.754
(A) K	0.22	0.208	0.246	0.191	0.231	0.217	0.195	0.276	0.258	0.259	0.265	0.279	0.27	0.268	0.224	0.211	0.218	0.204
O (non-W)	22	22	22	22	22	22	22	22	22	22	22	22	22	22	22	22	22	22
(W) OH	1.323	1.255	1.08	0.99	1.173	1.061	0.936	1.232	1.328	1.302	1.318	1.264	1.266	1.25	1.043	1.056	1.119	0.981
(W) F	0.117	0.146	0.095	0.121	0.054	0.066	0.085	0.098	0.014	0.044	0.031	0.043	0.055	0.056	0.124	0.125	0.083	0.181
(W) Cl	0.009	0.02	0	0.002	0.01	0.003	0.004	0.027	0.02	0.021	0.015	0.021	0.026	0.028	0.004	0.007	0.003	0.007
(W) O	0.551	0.579	0.825	0.886	0.764	0.87	0.975	0.644	0.639	0.632	0.636	0.672	0.653	0.666	0.828	0.812	0.795	0.832
Sum (T,C,B,A)	15.95	15.899	15.933	15.932	15.979	15.891	15.857	15.887	15.924	15.878	15.894	15.907	15.902	15.926	15.921	15.832	15.92	15.959

Table 3: LA-ICP-MS trace element composition of representative amphibole and clinopyroxene crystals from Predazzo camptonite

Sample	FC80	FC80	FC80	FC80	FC80	FC80	FC80	FC80
Mineral	Amph	Amph	Amph	Amph3	Amph2_core	Amph2_rim	Cpx	Cpx
Type	*Type 1_core*	*Type 1_rim*	*Type 1_groundmass*	*Type 2_rim*	*Type 4_core*	*Type 4_rim*	Large phenoXX	Small phenoXX
Trace element (ppm)								
Sc	53.670	89.030	54.330	65.190	32.225	77.530	124.850	148.210
V	398.665	519.700	379.830	343.440	333.475	519.990	409.270	453.925
Cr	9.830	131.000	22.485	195.080	21.245	62.270	542.315	941.050
Co	58.415	55.180	57.550	55.115	52.450	54.550	30.240	31.635
Ni	55.205	95.635	55.720	80.480	23.930	94.380	65.720	71.360
Zn	n.d.	n.d.	n.d.	n.d.	n.d.	n.d.	n.d.	n.d.
Pb	0.441	0.550	0.372	0.569	0.744	0.474	0.234	0.196
Cs	0.050	0.260	n.d.	0.179	n.d.	0.169	n.d.	n.d.
Rb	5.340	6.195	6.055	6.705	6.990	6.510	0.049	n.d.
Ba	291.855	365.970	349.270	303.505	429.855	356.940	0.521	0.328
Th	0.095	0.078	0.101	0.040	0.151	0.131	0.080	0.106
U	0.043	0.022	0.018	0.050	0.029	<0.0118	0.011	0.016
Nb	16.310	22.335	20.005	17.685	27.125	16.080	0.511	0.854
Ta	0.681	1.054	0.973	0.826	0.981	0.862	0.095	0.096
La	7.960	7.080	10.195	7.095	12.860	7.590	5.390	4.985
Ce	25.540	23.345	33.460	23.420	38.760	22.910	18.490	18.585
Pr	4.355	4.130	5.590	4.170	6.320	4.130	3.510	3.410
Sr	767.490	763.915	786.870	728.255	796.760	735.690	100.915	103.345
Nd	24.160	22.885	30.780	23.530	33.730	22.780	20.475	20.580
Zr	83.480	120.945	112.995	96.095	134.655	97.380	98.605	113.245
Hf	2.760	4.085	3.500	3.475	4.425	3.710	3.915	5.030
Sm	6.815	5.905	8.160	6.520	8.315	6.540	6.865	6.465
Eu	2.290	2.295	2.530	2.550	2.925	2.033	2.205	2.310
Gd	6.470	6.760	7.150	6.450	7.750	6.290	6.200	6.065
Tb	1.047	1.069	1.274	1.130	1.214	1.042	1.155	1.095
Dy	6.090	5.895	6.755	6.130	7.600	5.690	6.820	6.835
Y	30.115	30.060	34.325	32.300	38.270	29.120	31.030	33.470
Ho	1.185	1.163	1.319	1.341	1.408	1.180	1.325	1.414
Er	2.955	3.105	3.200	3.220	3.910	3.040	3.030	3.185
Tm	0.375	0.433	0.454	0.403	0.531	0.390	0.501	0.529
Yb	2.525	2.430	3.105	2.730	3.370	2.520	2.720	3.170
Lu	0.373	0.298	0.440	0.358	0.507	0.405	0.391	0.455

Table 4: Major element composition and a.p.f.u. calculation of representative clinopyroxene crystals from Predazzo lamprophyres

Sample	FC80 - Camptonite												MA5 - Camptonite						FF14 - Camptonite				
Name	Cpx1 c	Cpx1 r	Cpx3 c	Cpx4 c	Cpx6 c	Cpx6 tr1	Cpx8 c	Cpx11 c	Cpx11 r	Cpx14 c	Cpx14 r	Cpx19 c	Cpx1 c	Cpx1 tr1	Cpx1 r	Cpx2 c	Cpx3 c	Cpx4 c	Cpx1 c	Cpx2 c	Cpx5 c	Cpx8 c	Cpx12 c
Oxide (wt%)																							
SiO_2	49.604	42.278	48.742	47.089	44.324	45.773	43.078	45.583	48.050	45.548	45.762	46.792	47.658	47.176	43.272	43.518	47.591	42.472	44.043	44.549	42.305	47.141	48.427
TiO_2	1.108	4.031	1.206	2.126	2.065	2.136	3.164	2.266	2.012	2.151	1.974	1.744	1.461	1.491	3.773	3.844	2.089	4.049	3.343	2.614	3.633	1.947	1.536
Al_2O_3	5.005	9.933	5.847	5.462	10.878	9.710	10.085	9.836	5.581	9.582	9.247	9.208	8.612	9.028	10.068	9.320	5.270	9.178	9.003	8.648	10.510	5.790	4.823
FeO_{TOT}	5.751	8.483	6.028	8.099	8.532	6.142	7.942	6.680	7.971	6.469	6.756	6.383	5.394	5.476	7.874	8.073	8.106	9.655	6.928	6.474	7.052	8.213	6.620
MnO	0.138	0.139	0.130	0.180	0.176	0.118	0.143	0.125	0.200	0.126	0.126	0.116	0.110	0.119	0.110	0.133	0.146	0.139	0.112	0.130	0.096	0.168	0.170
MgO	14.534	10.291	14.344	12.714	10.378	12.376	11.069	12.295	12.714	12.290	12.161	12.765	13.600	13.384	11.329	11.037	13.487	10.405	11.393	12.179	11.164	12.814	14.086
CaO	22.176	22.555	21.673	22.676	21.990	22.073	22.669	22.133	22.611	22.259	22.334	21.958	22.045	21.903	22.618	22.829	21.650	22.464	22.758	22.967	22.873	22.475	22.767
Na_2O	0.502	0.594	0.505	0.410	0.754	0.641	0.471	0.621	0.448	0.624	0.597	0.650	0.555	0.558	0.414	0.533	0.322	0.524	0.408	0.406	0.416	0.332	0.283
K_2O	0.000	0.017	0.000	0.022	0.004	0.005	0.005	0.008	0.008	0.000	0.002	0.014	0.000	0.015	0.004	0.005	0.000	0.006	0.059	0.012	0.023	0.014	0.007
Cr_2O_3	0.133	0.000	0.155	0.010	0.041	0.142	0.025	0.194	0.000	0.258	0.047	0.205	0.462	0.510	0.249	0.202	0.121	0.002	0.442	0.830	0.463	0.025	0.159
NiO	0.000	0.019	0.020	0.013	0.009	0.022		0.012	0.007	0.000	0.010	0.015	0.036	0.034	0.017	0.000	0.006	0.000	0.020	0.000	0.000	0.000	0.000
Tot.	98.933	98.336	98.643	98.799	99.150	99.138	98.782	99.754	99.601	99.306	99.015	99.849	99.932	99.695	99.727	99.494	98.788	98.893	98.510	98.804	98.557	98.983	98.933
Mg#	**81.8**	**68.4**	**80.9**	**73.7**	**68.4**	**78.2**	**71.3**	**76.6**	**74.0**	**77.2**	**76.2**	**78.1**	**81.8**	**81.3**	**71.9**	**70.9**	**74.8**	**65.8**	**74.6**	**77.0**	**73.8**	**73.5**	**79.1**
A.p.f.u.																							
(T) Si^{4+}	1.841	1.612	1.815	1.775	1.664	1.703	1.628	1.688	1.796	1.694	1.708	1.727	1.751	1.738	1.621	1.636	1.791	1.616	1.667	1.674	1.600	1.774	1.810
(T) Al^{3+}	0.159	0.388	0.185	0.225	0.336	0.297	0.372	0.312	0.204	0.306	0.292	0.273	0.249	0.262	0.379	0.364	0.209	0.384	0.333	0.326	0.400	0.226	0.190
(T) Fe^{3+}	0.000	0.000	0.000	0.000	0.000	0.000	0.000	0.000	0.000	0.000	0.000	0.000	0.000	0.000	0.000	0.000	0.000	0.000	0.000	0.000	0.000	0.000	0.000
(M1) Al^{3+}	0.060	0.058	0.072	0.017	0.146	0.128	0.077	0.118	0.041	0.114	0.115	0.127	0.124	0.130	0.065	0.050	0.025	0.028	0.069	0.057	0.069	0.031	0.022
(M1) Fe^{3+}	0.069	0.144	0.078	0.119	0.127	0.092	0.149	0.107	0.083	0.109	0.108	0.091	0.071	0.075	0.124	0.130	0.086	0.164	0.093	0.127	0.142	0.110	0.097
(M1) Ti^{4+}	0.031	0.116	0.034	0.060	0.058	0.060	0.090	0.063	0.057	0.060	0.055	0.048	0.040	0.041	0.106	0.109	0.059	0.116	0.095	0.074	0.103	0.055	0.043
(M1) Cr^{3+}	0.004	0.000	0.005	0.000	0.001	0.004	0.001	0.006	0.000	0.008	0.001	0.006	0.013	0.015	0.007	0.006	0.004	0.000	0.013	0.025	0.014	0.001	0.005
(M1) Ni^{2+}	0.000	0.001	0.001	0.000	0.000	0.001	0.000	0.000	0.000	0.000	0.000	0.000	0.001	0.001	0.001	0.000	0.000	0.000	0.001	0.000	0.000	0.000	0.000
(M1) Mg^{2+}	0.804	0.585	0.796	0.714	0.581	0.686	0.624	0.679	0.708	0.681	0.677	0.702	0.745	0.735	0.633	0.619	0.757	0.590	0.643	0.682	0.630	0.719	0.785
(M1) Fe^{2+}	0.032	0.097	0.015	0.089	0.086	0.029	0.060	0.027	0.111	0.028	0.043	0.025	0.006	0.003	0.064	0.087	0.070	0.103	0.086	0.035	0.042	0.085	0.047
(M2) Fe^{2+}	0.078	0.030	0.095	0.048	0.055	0.070	0.043	0.073	0.056	0.064	0.060	0.081	0.089	0.091	0.059	0.037	0.099	0.041	0.041	0.041	0.038	0.064	0.062
(M2) Mn^{2+}	0.004	0.004	0.004	0.006	0.006	0.004	0.005	0.004	0.006	0.004	0.004	0.004	0.003	0.004	0.003	0.004	0.005	0.004	0.004	0.004	0.003	0.005	0.005
(M2) Ca^{2+}	0.882	0.921	0.865	0.916	0.885	0.880	0.918	0.878	0.905	0.887	0.893	0.868	0.868	0.865	0.908	0.920	0.873	0.916	0.923	0.925	0.927	0.906	0.912
(M2) Na^{+}	0.036	0.044	0.036	0.030	0.055	0.046	0.035	0.045	0.032	0.045	0.043	0.046	0.040	0.040	0.030	0.039	0.023	0.039	0.030	0.030	0.031	0.024	0.021
(M2) K^{+}	0.000	0.001	0.000	0.001	0.000	0.000	0.000	0.000	0.000	0.000	0.000	0.001	0.000	0.001	0.000	0.000	0.000	0.000	0.003	0.001	0.001	0.001	0.000
Wo	47.18	51.72	46.67	48.42	50.87	49.96	51.07	49.68	48.44	50.01	50.04	49.02	48.70	48.79	50.70	51.19	46.20	50.38	51.60	50.96	52.00	47.97	47.76
En	43.03	32.84	42.98	37.78	33.41	38.98	34.70	38.40	37.90	38.42	37.92	39.65	41.81	41.48	35.33	34.44	40.05	32.47	35.94	37.60	35.32	38.06	41.12
Fs	9.78	15.44	10.35	13.80	15.73	11.06	14.22	11.92	13.67	11.57	12.04	11.33	9.49	9.73	13.97	14.37	13.75	17.15	12.46	11.44	12.69	13.97	11.12
Tot.	100.00	100.00	100.00	100.00	100.00	100.00	100.00	100.00	100.00	100.00	100.00	100.00	100.00	100.00	100.00	100.00	100.00	100.00	100.00	100.00	100.00	100.00	100.00

Table 5: Major element composition and a.p.f.u. calculation of representative plagioclase (Plag) and K-feldspar (K-Feld) crystals from Predazzo lamprophyres

Sample	FC80 - Camptonite										FF14 - Camptonite						MA5 - Camptonite		MA1 - Bostonite				
Mineral	Plag	Plag	Plag	Plag	Plag	Plag	Plag	Plag	Plag	Plag	Plag	Plag	Plag	Plag	Plag	Plag	Plag	Plag	Plag	Plag	K-Feld	K-Feld	K-Feld
Name	Plag1_c	Plag1_tr1	Plag1_tr2	Plag1_tr3	Plag1_r	Plag4_c	Plag5_c	Plag5_r	PLag7_c	Plag7_r	Plag3_c	Plag4_c	Plag8_c	Plag10_c	Plag11_c	Plag14_c	Plag3_c	Plag5_c	Plag1_c	Plag3_c	Kf1_c	Kf2_c	Kf4_c
Oxide (wt%)																							
SiO_2	56.994	55.766	56.303	56.115	49.614	51.747	55.204	49.116	52.291	50.105	53.309	51.735	49.748	55.984	49.369	50.193	49.209	49.275	61.624	56.077	64.624	65.065	65.340
TiO_2	0.013	0.000	0.002	0.012	0.107	0.087	0.013	0.086	0.015	0.102	0.148	0.127	0.091	0.126	0.067	0.121	0.081	0.071	0.024	0.041	0.012	0.000	0.014
Al_2O_3	26.996	27.050	27.099	27.365	30.781	30.266	28.417	31.571	30.506	31.151	29.209	29.855	30.713	27.734	31.030	30.352	31.688	32.093	23.858	26.491	19.408	19.523	19.125
FeO_{TOT}	0.147	0.450	0.151	0.143	0.587	0.639	0.203	0.596	0.043	0.520	0.595	0.614	0.631	0.560	0.770	0.676	0.619	0.554	0.309	0.418	0.271	0.195	0.207
MnO	0.000	0.006	0.000	0.000	0.000	0.020	0.004	0.003	0.002	0.008	0.013	0.000	0.007	0.006	0.014	0.000	0.009	0.000	0.009	0.009	0.010	0.000	0.005
MgO	0.002	0.379	0.000	0.000	0.082	0.071	0.006	0.101	0.000	0.079	0.050	0.067	0.112	0.029	0.131	0.125	0.111	0.104	0.008	0.032	0.012	0.000	0.010
CaO	8.566	9.274	8.988	9.313	13.734	12.879	10.469	14.586	12.605	13.943	11.550	12.615	13.904	9.586	14.186	13.688	15.000	15.240	4.748	8.586	0.294	0.350	0.244
BaO	0.000	0.013	0.000	0.027	0.066	0.036	0.007	0.037	0.000	0.009	0.049	0.071	0.000	0.143	0.000	0.029	0.000	0.000	0.000	0.000	0.000	0.000	0.000
Na_2O	6.687	5.987	6.230	6.216	3.380	3.857	5.559	3.047	4.439	3.471	4.736	4.084	3.131	5.529	3.186	3.453	3.025	2.841	7.941	6.184	4.700	5.019	5.021
K_2O	0.240	0.189	0.220	0.174	0.265	0.289	0.247	0.211	0.190	0.246	0.453	0.378	0.496	0.643	0.240	0.301	0.135	0.146	1.177	0.579	9.925	9.465	9.555
Tot.	99.610	99.113	98.986	99.347	98.609	99.890	100.130	99.353	100.064	99.632	100.110	99.537	98.825	100.341	98.980	98.938	99.875	100.323	99.696	98.417	99.255	99.618	99.561
A.p.f.u.																							
Si	2.558	2.526	2.551	2.533	2.292	2.356	2.482	2.256	2.363	2.289	2.410	2.361	2.296	2.518	2.275	2.312	2.249	2.244	2.751	2.557	2.942	2.946	2.963
Ti	0.000	0.000	0.000	0.000	0.004	0.003	0.000	0.003	0.001	0.004	0.005	0.004	0.003	0.004	0.002	0.004	0.003	0.002	0.001	0.001	0.000	0.000	0.000
Al	1.428	1.444	1.447	1.456	1.676	1.624	1.506	1.709	1.625	1.677	1.557	1.606	1.671	1.470	1.685	1.648	1.707	1.722	1.255	1.424	1.041	1.042	1.022
Cr	0.000	0.000	0.000	0.000	0.000	0.000	0.000	0.000	0.000	0.000	0.000	0.000	0.000	0.000	0.000	0.000	0.000	0.000	0.000	0.000	0.000	0.000	0.000
Fe^{3+}	0.000	0.000	0.000	0.000	0.000	0.000	0.000	0.000	0.000	0.000	0.000	0.000	0.000	0.000	0.000	0.000	0.000	0.000	0.000	0.000	0.000	0.000	0.000
Fe^{2+}	0.006	0.017	0.006	0.005	0.023	0.024	0.008	0.023	0.002	0.020	0.022	0.023	0.024	0.021	0.030	0.026	0.024	0.021	0.012	0.016	0.010	0.007	0.008
Mn	0.000	0.000	0.000	0.000	0.000	0.001	0.000	0.000	0.000	0.000	0.000	0.000	0.000	0.000	0.001	0.000	0.000	0.000	0.000	0.000	0.000	0.000	0.000
Mg	0.000	0.026	0.000	0.000	0.006	0.005	0.000	0.007	0.000	0.005	0.003	0.005	0.008	0.002	0.009	0.009	0.008	0.007	0.001	0.002	0.001	0.000	0.001
Ca	0.412	0.450	0.436	0.450	0.680	0.628	0.504	0.718	0.610	0.683	0.560	0.617	0.688	0.462	0.700	0.675	0.734	0.744	0.227	0.419	0.014	0.017	0.012
Ba	0.000	0.000	0.000	0.000	0.001	0.001	0.000	0.001	0.000	0.000	0.001	0.001	0.000	0.003	0.000	0.001	0.000	0.000	0.000	0.000	0.000	0.000	0.000
Na	0.582	0.526	0.547	0.544	0.303	0.341	0.485	0.271	0.389	0.307	0.415	0.361	0.280	0.482	0.285	0.308	0.268	0.251	0.687	0.547	0.415	0.441	0.441
K	0.014	0.011	0.013	0.010	0.016	0.017	0.014	0.012	0.011	0.014	0.026	0.022	0.029	0.037	0.014	0.018	0.008	0.008	0.067	0.034	0.576	0.547	0.553
Tot. cat.	5.000	5.000	5.000	5.000	5.000	5.000	5.000	5.000	5.000	5.000	5.000	5.000	5.000	5.000	5.000	5.000	5.000	5.000	5.000	5.000	5.000	5.000	5.000
Tot. oxy.	7.975	7.980	7.994	7.985	7.975	7.993	7.986	7.972	7.976	7.970	7.973	7.976	7.980	7.998	7.970	7.977	7.967	7.978	8.002	7.980	7.967	7.974	7.977
An	40.88	45.61	43.79	44.84	68.10	63.75	50.28	71.67	60.41	67.96	55.91	61.67	68.97	47.09	70.10	67.45	72.69	74.14	23.14	41.95	1.43	1.69	1.18
Ab	57.75	53.28	54.93	54.16	30.33	34.55	48.31	27.09	38.50	30.61	41.48	36.13	28.10	49.15	28.49	30.79	26.53	25.01	70.03	54.68	41.25	43.87	43.88
Or	1.36	1.11	1.28	1.00	1.56	1.70	1.41	1.23	1.08	1.43	2.61	2.20	2.93	3.76	1.41	1.77	0.78	0.84	6.83	3.37	57.32	54.44	54.94
Tot.	100.00	100.00	100.00	100.00	100.00	100.00	100.00	100.00	100.00	100.00	100.00	100.00	100.00	100.00	100.00	100.00	100.00	100.00	100.00	100.00	100.00	100.00	100.00

Table 6: Major element composition and a.p.f.u. calculation of representative Fe-Ti oxides from Predazzo lamprophyres

Sample	FC80 - Camptonite				MA1 - Bostonite
Name	Ox1	Ox2	Ox5	Ox7	Ox3
Oxides (wt%)					
SiO_2	0.524	0.097	0.788	0.514	2.106
TiO_2	17.615	12.139	18.982	18.339	12.260
Al_2O_3	7.851	2.330	5.533	7.381	4.283
FeO	61.332	77.084	63.173	62.735	69.367
MnO	0.783	0.976	0.907	0.756	1.451
MgO	2.331	0.219	0.950	2.418	0.196
CaO	0.166	0.119	0.562	0.198	0.219
Cr_2O_3	0.146	0.000	0.044	0.036	0.043
V_2O_3	0.455	0.086	0.363	0.469	0.097
NiO	0.000	0.000	0.000	0.000	0.030
ZnO	0.166	0.238	0.322	0.110	0.237
Tot.	91.364	93.269	91.615	92.956	90.288
A.p.f.u.					
Si	0.020	0.004	0.031	0.019	0.083
Ti	0.503	0.352	0.553	0.515	0.363
Al	0.351	0.106	0.253	0.325	0.199
Fe^{3+}	0.000	0.000	0.000	0.000	0.000
Fe^{2+}	1.947	2.487	2.046	1.961	2.283
Mn	0.025	0.032	0.030	0.024	0.048
Mg	0.132	0.013	0.055	0.135	0.011
Ca	0.007	0.005	0.023	0.008	0.009
Cr	0.004	0.000	0.001	0.001	0.001
V	0.011	0.002	0.009	0.012	0.003
Tot. Cat.	3.000	3.000	3.000	3.000	3.000
FeO (mol%)	**63.04**	**58.10**	**63.78**	**62.76**	**62.79**
Fe_2O_3 (mol%)	**13.63**	**26.24**	**12.33**	**13.60**	**20.67**
TiO_2 (mol%)	**23.32**	**15.66**	**23.90**	**23.65**	**16.55**

Table 7: Major element composition of representative carbonates in Predazzo lamprophyres

Sample	FC80 - Camptonite														
Name	C1	C3	C4	C5	C6	C7	C9	C10	C11	C13	C14	C15	C16	C18	C19
Oxides (wt%)															
SiO_2	0.023	0.017	0.011	0.006	0.012	0.007	0.016	0.025	0.000	0.043	0.000	0.021	0.000	0.000	0.030
FeO	35.147	34.065	32.973	5.434	10.377	5.523	6.483	10.561	38.746	38.623	38.958	14.368	7.794	5.001	6.548
MnO	0.406	0.447	0.483	0.544	0.249	0.467	0.391	0.328	0.647	0.550	0.581	0.423	0.477	0.421	0.450
MgO	18.482	18.521	17.697	18.416	16.137	18.578	18.025	13.629	14.356	15.035	15.342	12.706	16.453	18.538	17.990
CaO	2.209	3.343	5.232	28.475	27.579	29.062	28.604	29.870	3.645	3.137	2.250	27.823	28.638	28.816	27.907
SrO	0.000	0.000	0.000	0.212	0.080	0.166	0.033	0.054	0.000	0.000	0.000	0.066	0.161	0.304	0.098
Tot.	56.266	56.393	56.397	53.087	54.435	53.803	53.552	54.465	57.394	57.388	57.131	55.405	53.522	53.080	53.023
$CaCO_3$ (%)	**3.966**	**5.962**	**9.343**	**48.352**	**47.239**	**48.690**	**48.411**	**52.050**	**6.703**	**5.737**	**4.131**	**48.722**	**49.310**	**48.831**	**47.715**
$MgCO_3$ (%)	**46.167**	**45.958**	**43.971**	**43.510**	**38.457**	**43.306**	**42.446**	**33.043**	**36.728**	**38.254**	**39.194**	**30.957**	**39.416**	**43.708**	**42.798**
$FeCO_3$ (%)	**49.253**	**47.421**	**45.961**	**7.202**	**13.873**	**7.222**	**8.565**	**14.364**	**55.610**	**55.129**	**55.833**	**19.639**	**10.474**	**6.615**	**8.739**
$SrCO_3$ (%)	**0.000**	**0.000**	**0.024**	**0.197**	**0.075**	**0.152**	**0.031**	**0.051**	**0.018**	**0.012**	**0.000**	**0.063**	**0.152**	**0.281**	**0.091**
$MnCO_3$ (%)	**0.577**	**0.630**	**0.682**	**0.730**	**0.337**	**0.619**	**0.523**	**0.451**	**0.941**	**0.796**	**0.843**	**0.585**	**0.649**	**0.564**	**0.608**

Table 8: *P*, *T*, fO_2 and H_2O parameters obtained by mineral-melt and single mineral calculations on Predazzo lamprophyres. For each applied method, the corresponding reference and error on the single parameters are reported. *T* and *P* of clinopyroxene crystallization were obtained by means of the mineral-melt equations of Putirka (2008). Oxygen fugacity was calculated by means of the Ishibashi (2013) oxy-barometer. The water content of the melt during amphibole crystallization was calculated using the Ridolfi *et al.* (2010) single-mineral hygrometer. *T* and *P* of amphibole crystallization were obtained by means of the Putirka (2016) mineral-melt thermometer and H_2O-dependent barometer. This latter equation was applied by considering as input the H_2O content of the coexisting melt resulted from the hygrometer of Ridolfi *et al.* (2010). Cpx = clinopyroxene; Amph = amphibole

Sample	Type (Amph)	Method	Reference	T (°C)	Error (°C)	P (kbar)	Error (kbar)	H_2O (wt%)	Error (wt%)	$\log fO_2$
MA5 - Camptonite	-	Cpx-melt	Putirka (2008), Eq. 32a/32d	1060-1124	±58	2.3-6.4	±3.1	-	-	-
FC80 - Camptonite	*Type 1_core*	Amph-only; Amph-melt	Ridolfi et al. (2010); Putirka (2016), Eq. 5/7b	1023-1069	±30	9.2-11.6	±1.7	7.2-8.5	±0.8-1.2	-
FC80 - Camptonite	*Type 1_rim*	Amph-only; Amph-melt	Ridolfi et al. (2010); Putirka (2016), Eq. 5/7b	1038-1067	±30	7.4-9.0	±1.7	6.8-7.5	±0.8-1.2	-
FC80 - Camptonite	*Type 1_intermediate*	Amph-only; Amph-melt	Ridolfi et al. (2010); Putirka (2016), Eq. 5/7b	1071	±30	10.5	±1.7	7.7	±0.8-1.2	-
FC80 - Camptonite	*Type 1_groundmass*	Amph-only; Amph-melt	Ridolfi et al. (2010); Putirka (2016), Eq. 5/7b	1025-1074	±30	8.5-11.1	±1.7	6.7-8.1	±0.8-1.2	-
MA1 - Bostonite	*Type 1_core*	Amph-only; Amph-melt	Ridolfi et al. (2010); Putirka (2016), Eq. 5/7b	948-1042	±30	6.2-9.8	±1.7	6.5-7.7	±0.8-1.2	-
MA1 - Bostonite	*Type 1_rim*	Amph-only; Amph-melt	Ridolfi et al. (2010); Putirka (2016), Eq. 5/7b	1031-1032	±30	6.0-6.4	±1.7	6.2-6.6	±0.8-1.2	-
MA1 - Bostonite	*Type 1_groundmass*	Amph-only; Amph-melt	Ridolfi et al. (2010); Putirka (2016), Eq. 5/7b	1001-1029	±30	4.7-8.0	±1.7	6.5-7.6	±0.8-1.2	-
FC80 - Camptonite	*Type 2_core*	Amph-only; Amph-melt	Ridolfi et al. (2010); Putirka (2016), Eq. 5/7b	997-1009	±30	8.9-9.2	±1.7	6.8-7.1	±0.8-1.2	-
FC80 - Camptonite	*Type 2_rim*	Amph-only; Amph-melt	Ridolfi et al. (2010); Putirka (2016), Eq. 5/7b	1005-1053	±30	7.3-7.7	±1.7	6.8-7.0	±0.8-1.2	-
FC80 - Camptonite	*Type 2_intermediate*	Amph-only; Amph-melt	Ridolfi et al. (2010); Putirka (2016), Eq. 5/7b	1051-1063	±30	9.2-9.7	±1.7	7.2-7.4	±0.8-1.2	-
FC80 - Camptonite	*Type 3_rim*	Amph-only; Amph-melt	Ridolfi et al. (2010); Putirka (2016), Eq. 5/7b	1057-1063	±30	8.7-9.8	±1.7	7.2-7.3	±0.8-1.2	-
MA1 - Bostonite	*Type 3_rim*	Amph-only; Amph-melt	Ridolfi et al. (2010); Putirka (2016), Eq. 5/7b	961-1030	±30	6.3-7.5	±1.7	6.4-7.8	±0.8-1.2	-
FC80 - Camptonite	*Type4_core*	Amph-only; Amph-melt	Ridolfi et al. (2010); Putirka (2016), Eq. 5/7b	1008	±30	12.2	±1.7	8.9	±0.8-1.2	-
FC80 - Camptonite	*Type4_rim*	Amph-only; Amph-melt	Ridolfi et al. (2010); Putirka (2016), Eq. 5/7b	1042-1060	±30	11.2-12.3	±1.7	8.3	±0.8-1.2	-
MA1 - Bostonite	*Type 5_core*	Amph-only; Amph-melt	Ridolfi et al. (2010); Putirka (2016), Eq. 5/7b	927-983	±30	9.6-11.3	±1.7	8.8-9.8	±0.8-1.2	-
MA1 - Bostonite	*Type 5_rim*	Amph-only; Amph-melt	Ridolfi et al. (2010); Putirka (2016), Eq. 5/7b	977-1048	±30	4.9-6.9	±1.7	5.8-6.9	±0.8-1.2	-
FC80 - Camptonite	-	Ti-magnetite-melt	Ishibashi (2013)	1100 (input)	-	5.0 (input)	-	-	-	-8.4/-10.0
FC80 - Camptonite	-	Ti-magnetite-melt	Ishibashi (2013)	1050 (input)	-	5.0 (input)	-	-	-	-9.4/-11.0

Table 9: Modal composition, melting proportions and REE composition of the mantle sources used in the partial melting models. I = Sp-lherzolite with DMM composition (Workman & Hart 2005); II = Sp-lherzolite; III = Grt-lherzolite; IV = Sp-Grt-Amph-lherzolite; V = Grt-Amph-lherzolite; VI = Grt-Phlog-lherzolite. Starting REE composition of II, III, IV, V and VI sources is fertile PM of Sun & McDonough (1989). REE partition coefficients used in the models are also reported. Ol, Opx, Cpx, Sp, Grt and Amph partition coefficients are from McKenzie & O'Nions (1991) and Schmidt *et al.* (1999), except for Tm in Cpx (Zack & Brumm, 1998). Phlog partition coefficients: La, Ce, Nd and Sm from Schmidt *et al.* (1999); Eu, Gd, Dy, Er, Yb and Lu from Fujimaki *et al.* (1984); Pr, Tb, Ho and Tm were extrapolated from the partition coefficients of the adjacent elements according to Barry *et al.* (2003)

Source modal composition	**I**	**II**	**III**	**IV**	**V**	**VI**
Ol	0.57	0.55	0.55	0.55	0.55	0.56
Opx	0.28	0.25	0.25	0.19	0.2	0.19
Cpx	0.13	0.15	0.15	0.15	0.15	0.15
Sp	0.02	0.05	-	0.02	-	-
Grt	-	-	0.05	0.04	0.04	0.02
Amph	-	-	-	0.05	0.06	0.02
Phlog	-	-	-	-	-	0.06

Source melting proportions	**I**	**II**	**III**	**IV**	**V**	**VI**
Ol	0.01	0.01	0.01	0.05	0.03	0.03
Opx	0.09	0.09	0.07	0.05	0.05	0.05
Cpx	0.6	0.6	0.6	0.1	0.22	0.1
Sp	0.3	0.3	-	0.1	0	-
Grt	-	-	0.32	0.2	0.2	0.15
Amph	-	-	-	0.5	0.5	0.37
Phlog	-	-	-	-	-	0.3

Source REE composition	**I**	**II**	**III**	**IV**	**V**	**VI**
La	0.192	0.687	0.687	0.687	0.687	0.687
Ce	0.55	1.775	1.775	1.775	1.775	1.775
Pr	0.107	0.276	0.276	0.276	0.276	0.276
Nd	0.581	1.354	1.354	1.354	1.354	1.354
Sm	0.239	0.444	0.444	0.444	0.444	0.444
Eu	0.0096	0.168	0.168	0.168	0.168	0.168
Gd	0.358	0.596	0.596	0.596	0.596	0.596
Tb	0.07	0.108	0.108	0.108	0.108	0.108
Dy	0.505	0.737	0.737	0.737	0.737	0.737
Ho	0.115	0.164	0.164	0.164	0.164	0.164
Er	0.348	0.48	0.48	0.48	0.48	0.48
Tm	-	0.074	0.074	0.074	0.074	0.074
Yb	0.365	0.493	0.493	0.493	0.493	0.493
Lu	0.058	0.074	0.074	0.074	0.074	0.074

Partition coefficients	**Ol**	**Opx**	**Cpx**	**Sp**	**Grt**	**Amph**	**Phlog**
La	0.0004	0.002	0.054	0.01	0.01	0.17	0.00002
Ce	0.0005	0.003	0.098	0.01	0.021	0.26	0.0002
Pr	0.0008	0.0048	0.15	0.01	0.054	0.35	0.0002
Nd	0.001	0.0068	0.21	0.01	0.087	0.44	0.0002
Sm	0.0013	0.01	0.26	0.01	0.217	0.76	0.0002
Eu	0.0016	0.013	0.31	0.01	0.32	0.88	0.0218
Gd	0.0015	0.016	0.3	0.01	0.498	0.86	0.0205
Tb	0.0015	0.019	0.31	0.01	0.75	0.83	0.025
Dy	0.0017	0.022	0.33	0.01	1.06	0.78	0.0281
Ho	0.0016	0.026	0.31	0.01	1.53	0.73	0.028
Er	0.0015	0.03	0.29	0.01	2	0.68	0.0303
Tm	0.0015	0.04	0.449	0.01	3	0.64	0.035
Yb	0.0015	0.049	0.28	0.01	4.03	0.59	0.0484
Lu	0.0015	0.06	0.28	0.01	5.5	0.51	0.0471